Viscoelastic free vibration analysis of in-plane functionally graded orthotropic plates integrated with piezoelectric sensors: Time-dependent 3D analytical solutions

Article *in* Mechanical Systems and Signal Processing · February 2023

DOI: 10.1016/j.ymssp.2022.109636

CITATIONS
0

READS
517

4 authors, including:

Agyapal Singh Brar
New York University
13 PUBLICATIONS **55** CITATIONS
SEE PROFILE

Susmita Naskar
University of Southampton
48 PUBLICATIONS **612** CITATIONS
SEE PROFILE

Tanmoy Mukhopadhyay
Indian Institute of Technology Kanpur
189 PUBLICATIONS **3,182** CITATIONS
SEE PROFILE

Viscoelastic free vibration analysis of in-plane functionally graded orthotropic plates integrated with piezoelectric sensors: Time-dependent 3D analytical solutions

A. Singh[1], S. Naskar[2], P. Kumari[3], T. Mukhopadhyay[1*]
[1]Department of Aerospace Engineering, Indian Institute of Technology Kanpur, Kanpur, India
[2]Faculty of Engineering and Physical Sciences, University of Southampton, Southampton, UK
[3]Department of Mechanical Engineering, Indian Institute of Technology Guwahati, Guwahati, India

ABSTRACT

This paper proposes an accurate three-dimensional framework for elastic and viscoelastic free vibration investigation of in-plane functionally graded (IPFG) orthotropic rectangular plates integrated with piezoelectric sensory layers. The developed analytical framework is capable of considering layer-wise unidirectional linear functional gradation in both stiffness and density of the orthotropic composite layers. 3D piezoelasticity-based governing equations of motion are formulated in mixed form by employing Hamilton's principle, and further solved analytically for Levy-type support conditions using the power-series-based extended Kantorovich method (EKM) jointly with Fourier series. The displacements, stresses, and electrical variables (electric field and electric potential) are solved as the primary variables that ensure the point-wise interlayer continuity and electro-mechanical support conditions. The viscoelastic property of the orthotropic interlayer is defined by employing Biot model, which is similar to the standard linear viscoelastic model. The correctness and efficacy of the present mathematical model are established by comparing the present numerical results with published literature and 3D finite element results, obtained by utilizing user material subroutine in the commercial FE software ABAQUS. An extensive numerical study is performed for various configurations and thickness ratios to investigate the influences of in-plane gradation, viscoelasticity and their coupled effects on the free-vibration response of hybrid laminated plates. It is found that in-plane gradation of stiffness and density remarkably alters the flexural frequencies and corresponding mode shapes of the hybrid intelligent rectangular plates. The flexural frequencies and stresses in the plate can be modified by selecting suitable grading indexes. Another interesting observation is that the in-plane gradation shows a considerably less effect on the electrical response of piezoelectric layers, which can play a vital role in the design of sensors and actuators for dynamic applications. Further, the numerical study demonstrates a potential time-dependent structural behaviour based on the present viscoelastic modelling. The consideration of viscoelasticity could be crucial for analysing the mechanical behaviour of a wide range of polymer composites more realistically and for prospective temporal programming in smart structural systems by exploiting the viscoelastic effect. Although the present analytical solution has been proposed for the free-vibration investigation of smart in-plane functionally graded (IPFG) viscoelastic plates, it can also be utilized directly to analyze the symmetric and asymmetric laminated piezoelectric smart plates with constant properties.

Keywords: Extended Kantorovich method for dynamic analysis; Time-domain viscoelastic analysis; Smart functionally graded materials; Three-dimensional solution for piezo-embedded plates

*Corresponding author, Email: tanmoy@iitk.ac.in (T. Mukhopadhyay)

1 Introduction

In the past decade, functionally graded materials have been widely explored for several engineering applications in the aerospace, civil, mechanical, and biomedical fields due to their superior mechanical and thermal properties [1, 2]. Such materials give freedom to the designers for tailoring the mechanical properties of structures like stiffness, density, and thermal resistance along particular directions according to the operational requirements. This is achieved by introducing gradation in the material properties along that particular direction. However, it makes the computational analysis of such structures more complicated because their governing equations involve some variable coefficients, which are the functions of coordinate along which the gradation is considered (unlike conventional isotropic and composite plates). Hence, the structural problem of functionally graded structure can not be solved by using the traditional methods proposed for the conventional structural problems [3]. Hence, more efficient and dedicated solution approaches are required for the accurate determination of structural behaviour of functionally graded structures under dynamic and static conditions, which is a prime focus of the present work.

A significant number of mathematical models have been developed for bending, fracture and natural frequency investigation of functionally graded beams, rectangular plates, and shell structures. An extensive review of the work related to functionally graded structures, presented by Byrd [4], Wu et al. [5] and Swaminathan et al. [6], suggests that in most of the studies through-thickness gradation of properties is considered following deterministic and stochastic frameworks [7–14]. However, over the last few years, the focus is getting diverted toward the in-plane and multidirectional functionally graded structures because it gives more freedom to control the material properties of thin structures for meeting application-specific demands, such as specific stiffness, strength, impact and thermal resistance, high fatigue strength, corrosion resistance, and acoustic properties [5]. In this context, Leissa and Martin [15] probed the buckling and natural frequency response of thin rectangular composite plates having in-plane graded properties and proved that desired buckling load and fundamental frequencies can be obtained effectively by controlling the gradation parameters of material along an in-plane direction.

Most of the analytical solutions for in-plane graded or multidirectional functionally graded plates published in the literature are based on two-dimensional (2D) theories of plates. For example, Tomar et al. [16] developed classical plate theory based 2D analytical solution for natural frequency investigation of isotropic functionally graded panels (length of the plate along is considered infinite along y-direction) employing Frobenius series. In this work, elastic modulus and density of the flat panel are taken exponentially graded along the axial (x) direction. Fares and Zenkour [17] have employed higher-order plate theory (HPT), first-order plate theory (FPT), and classical plate theory (CPT) to develop 2D analytical solutions for natural frequency and buckling investigation of multidirectional functionally graded orthotropic rectangular plates. They found that the index of gradation significantly affects the buckling and free vibration response of plate. Fourier series approach along with particular integration method has been utilized by Liu et al. [18] to solve the variable coefficient ordinary differential equation and they obtained classical plate theory (CPT) based solution for natural frequency analysis of in-plane functionally graded rectangular plates under Levy-type support condition. In their paper, they concluded that the desired natural frequencies can be attained by adjusting grading indexes. Yu et al. [19] have used the Whittaker technique for solving the fourth-order variable coefficients governing equation to obtain an analytical solution for flexural analysis of the thin in-plane graded isotropic plates of rectangular shape subjected to Levy-type end conditions. Recently, Amirpour et al. [20] provided HSDT-based analytical solutions for flexural investigation of in-plane functionally graded isotropic rectangular plates. In the literature, mostly 2D analytical solutions have been presented so far that belong to specific type of mechanical end conditions, like simply-supported or Levy-type support conditions. The governing equations involved in analysis are higher-order ODEs that have variable coefficients and to solve them in analytically for arbitrary boundary conditions is computationally difficult. Thus, some researchers employed numerical approaches to obtain reliable approximate two-dimensional solutions for in-plane multidirectional grada-

tion in rectangular plates. Numerical solutions for non-classical boundary conditions are developed using the higher-order shear deformation theory [21–23] and the classical plate theories (CPT) [24–29]. Recently, Xue et al. [30] reported an isogeometric numerical solution for natural frequency investigation of IPFG plates by utilizing a refined plate theory and also extended this solution to obtain a FSDT-based numerical solution for modal investigation of circular, square, and rectangular porous FGM plates having porosity gradation along the in-plane and thickness directions. Utilizing Rayleigh-Ritz and Bolotin's method, Loja and Barbosa [31] proposed a 2D numerical solution based on classical plate theory for natural frequency and dynamic instability investigation of in-plane functionally graded thin plates.

Although it is found that the higher-order theory-based 2D solutions are adequate and reliable in obtaining the global response of thinner orthotropic plates, the accuracy of 2D solutions significantly reduces as the plate becomes thicker [32] and 2D theory-based results are not reliable for higher modes [32]. In 3D elasticity solutions, no pre-assumptions are adopted in the distribution of deformations and stresses. Both stresses and strains are solved as primary variables. Hence, the 3D solution of plates achieves high accuracy and is always preferred for bench-marking purposes, including accurate prediction of stresses near edges (the variation of stresses in the vicinity of edges is highly non-linear). In this direction, Lü et al. [33] reported a 3D semi-analytical solution for multidirectional graded Levy-type plate by using differential quadrature method based state-space approach (SSDQM). The stiffness of the rectangular plate was assumed exponentially graded along the axial (x) and thickness (z) directions. This analysis shows that the behaviour of rectangular plates is affected more by axial stiffness variation than through-thickness stiffness variation. Singh and Kumari developed a power series-based extended Kantorovich elasticity analytical approach for flexural analysis of in-plane functionally graded composite beams [34–37], panels [38, 39], and rectangular plates [40]. Using a similar approach, Ravindran and Bhaskar [41] developed a 3D analytical approach for flexural analysis of IPFG simply-supported plates subjected to sinusoidal loading. They extended this approach further [42] for flexural analysis of simply-supported isotropic sandwich plates integrated with in-plane graded composite face sheets. Zhang et al. [43] have employed the scaled boundary finite element method (SBFEM) to obtain a 3D semi-analytical solution for the flexural investigation of in-plane functionally graded (IPFG) isotropic rectangular plates. Singh and Kumari [44] recently presented a 3D analytical model for natural frequency modal analysis of orthotropic IPFG rectangular plates.

Some researchers have also explored pure numerical approaches to analyze the IPFG plates under static and dynamic conditions. The graded finite element-based numerical technique has been developed by Asemi et al. [45] for flexural investigation of bidirectional functionally graded plates. Xiang et al. [46] utilized this recently developed scaled boundary finite element method to obtain a 3D solution for buckling and natural frequency of the IPFG isotropic rectangular plates subjected to Navier and all-around clamped supports. The Chebyshev spectral approach has been utilized by Huang et al. [47] to obtain a numerical solution for static flexural and natural frequency analysis of orthotropic IPFG rectangular plates subjected to general support conditions.

Piezoelectric materials are getting increasingly employed in active response control and sensing applications as actuators and sensors due to their inherent property of producing a voltage in response to deformation and vice-versa [48, 49]. When composite and FGM structures are integrated with piezoelectric sensors and actuators, their behaviours become very complex due to electro-mechanical coupling [50]. Due to weak coupling between elastic and electric parameters, the electrical response of active smart layers is very sensitive to internal or external factors such as internal imperfection or defects, external loading, etc. Moreover, when smart materials are used with FGM structure, the gradation of properties makes its response even more complex. Hence, efficient and reliable solutions are required to analyze the smart functionally graded structures accurately. A thorough review of the literature on functionally graded smart plates reveals that the through-thickness gradation of properties is commonly considered [51–55]. Only a few papers have been reported for in-plane functionally graded (IFGP) smart structures. Zhang

et al. [56] utilized the precise integration method (PIM) in conjunction with the scaled boundary finite element method (SBFEM) to develop a semi-analytical model for static flexural investigation of magneto-electro-elastic IPFG plates. Later they extended this model to develop a semi-analytical framework for bending analysis of the in-plane and multidirectional graded piezoelectric plates [57] and also to natural frequency analysis of magneto-electro-elastic IPFG rectangular plates [58]. In all these solutions, only elastic displacements along the x ,y and z-coordinates, magnetic potential and electric voltage are solved as the primary independent variables. To the best knowledge of the authors, no 3D analytical study has been presented to date for natural frequency investigation of in-plane functionally graded (IPFG) rectangular plates integrated with piezoelectric smart layers. Based on the extensive literature review, it is observed that benchmark 3D piezo-elasticity based analytical solutions are essential for in-plane functionally graded (IPFG) smart plates, which can serve as an accurate reference for future developments. Thus, this research work is carried out to fill this gap by providing a benchmark 3D mathematical model for IPFG plates.

Nowadays viscoelastic materials are widely used in vibration attenuation. Moreover, many of the polymers used in composites actually show a visco-elastic behaviour in their operational temperature regime. Besides accurate analysis of such structural systems, time-dependent viscoelastic behaviour can further be exploited for programming mechanical responses in smart structural systems. However, only a few works are reported for viscoelastic analysis with the coexistence of gradation and piezoelasticity. Zhang and Zheng [59] explored application of the Biot approach in analyzing the dynamic behavior of viscoelastic composite structures. Hu and Wang [60] studied the effect of viscoelasticity on free vibration behavior and transverse stresses with the help of Reddy's layerwise theory and showed that transverse stresses in the viscoelastic layer are the main factor that leads to delamination in lower modes. Mao et al. [61] studied the creep buckling and post-buckling behavior of layered viscoelastic piezoelectric plates graded along thickness direction. Zenkour [62] studied the bending behavior of elastic/ viscoelastic exponentially graded composite (EGC) rectangular sandwich plates using Illyushin's approximation methods. Wang et al. [63] used Kelvin-Voigt model for viscoelastic stability investigation of composite rectangular plates integrated with a smart piezoelectric layer and under a follower force. Alibeigloo [64] developed a 3D state-space model to study the effect of viscoelastic inter-layers on flexural and vibration response of simply-supported layered composite plates. Wu et al. [65] proposed a 3D elasticity-based analytical method for flexural investigation of simply supported layered plates having viscoelastic interlayers. Recently, Wang et al. [66] presented a 3D analytical model to investigate the time-dependent flexural response of exponential functionally graded laminated rectangular plates bonded by viscoelastic adhesive inter-layers. Apart from that, the application of viscoelastic layers in vibration damping is significantly explored in many recent studies [67–71]. Sun et al. [72] developed an inverse approach for calculating the frequency-dependent mechanical properties of viscoelastic medium using measured frequency response functions (FRFs). Grosso et al. [73] developed an experimental identification technique for calculating equivalent viscoelastic parameters of the model for layered thin-walled structures from the vibration data.

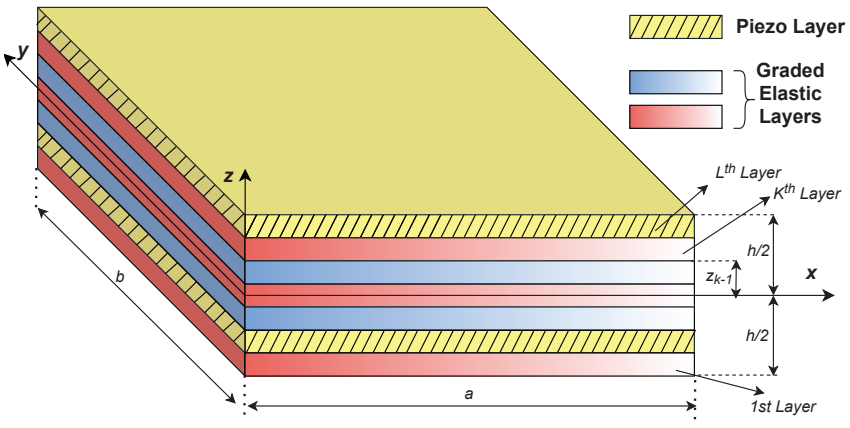

Fig. 1: Geometry of smart in-plane functionally graded (IPFG) plates.

Based on the discussions presented in the preceding paragraphs, it becomes evident that development of an accurate 3D analytical solution approach for graded piezoelectric composites including the effect of viscoelasticity would have a wide range of impacts for analyzing and designing smart structural systems. In this article, we aim to propose an accurate 3D analytical framework for viscoelastic natural frequency investigation of in-plane functionally graded (IPFG) orthotropic rectangular plates integrated with piezoelectric layers [Advantages of the proposed mathematical model compared to others are listed in Remark 1, Appendix G (refer to the Supplementary material)]. Although the present analytical model is developed for the analysis of smart IPFG viscoelastic plates, it is also directly applicable for the investigation of laminated piezoelectric rectangular elastic and viscoelastic plates without any gradation. The present paper is organized chronologically in six sections as follows; the mathematical formulation of the 3D governing equations using the piezo-elasticity-based Hamilton's principle is explained in Sec. 2. In Sec. 3, the viscoelastic mathematical model is developed for obtaining effective viscoelastic properties of the viscoelastic layer in time domain. In Sec. 4, the extended Kantorovoch method together with the power series and Fourier series method is used to attain a solution in the approximated analytical form. Sec. 5 is dedicated to validation and numerical investigation. In section Sec. 5.1, numerical results are presented for elastic case and Sec. 5.2 is dedicated to viscoelastic analysis. Finally, the conclusions and interesting findings of the present study are summarized in the Sec. 6.

2 3D piezo-elasticity based formulation for modal analysis of hybrid FGM plates

A laminated in-plane functionally graded (IPFG) hybrid rectangular plate ($x \in (0, a)$, $z = -h/2,\ h/2$, $y \in (0, b)$) integrated with piezoelectric layers, as demonstrated in Fig. 1, is taken into consideration for the present numerical study. In such type of plates, the in-plane gradation of material properties in the elastic layers is helpful to control flexural frequency response of plate and at the same time piezoelectric layers act as sensor to sense the behaviour of plate under different gradation cases. The considered rectangular functionally graded plate consists of total L number of orthotropic IPFG layers and $\xi_1\ (= x/a)$, $\zeta^{(k)} = (z - z_{k-1})/t^{(k)}$ and $\xi_2\ (= y/b)$ are non-dimensionalized layer parameter defined for x, z (thickness) and y-direction, respectively. Here the non-dimensional parameters ξ_1 and ξ_2 are defined as global parameters which are valid for all layers. But $\zeta^{(k)}$ is local thickness parameter of layer defined for each kth layer and $t^{(k)}$ denotes the thickness of that kth layer, and z_k represents thickness coordinate parameter for the upper layer surface of that kth layer. These superscripts of layers may be excluded in the further mathematical expressions unless absolutely needed for better clarity.

The strain-displacement and the electrical field-potential relations for the 3D rectangular hybrid plate can be written as,

$$\begin{bmatrix}\varepsilon_x\\ \varepsilon_y\\ \varepsilon_z\end{bmatrix} = \begin{bmatrix}u_{,x}\\ v_{,y}\\ w_{,z}\end{bmatrix};\qquad \begin{bmatrix}\gamma_{yz}\\ \gamma_{zx}\\ \gamma_{xy}\end{bmatrix} = \begin{bmatrix}v_{,z} + w_{,y}\\ w_{,x} + u_{,z}\\ u_{,y} + v_{,x}\end{bmatrix};\qquad \begin{bmatrix}E_x\\ E_y\\ E_z\end{bmatrix} = \begin{bmatrix}\phi_{,x}\\ \phi_{,y}\\ \phi_{,z}\end{bmatrix} \tag{1}$$

In these expressions ε_i represents normal strains and γ_{ij} represents shear strains of the plate, wherein w, v and u denote the displacement along z, y and x directions, respectively. Similarly, electric fields along x, y and z directions are designated by E_x, E_y and E_z, respectively. $\bar{\phi}$ denotes electric potential in the piezo-electric layer.

The 3D piezo-elasticity based linear constitutive equations for an orthotropic smart layer can be expressed as

$$\begin{aligned}
\varepsilon_x &= s_{11}\sigma_x + s_{12}\sigma_y + s_{13}\sigma_z + d_{31}E_z\\
\varepsilon_y &= s_{12}\sigma_x + s_{22}\sigma_y + s_{23}\sigma_z + d_{32}E_z\\
\varepsilon_z &= s_{13}\sigma_x + s_{23}\sigma_y + s_{33}\sigma_z + d_{33}E_z\\
\gamma_{yz} &= s_{44}\tau_{yz} + d_{24}E_y\\
\gamma_{zx} &= s_{55}\tau_{zx} + d_{15}E_x
\end{aligned} \tag{2}$$

$$\gamma_{xy} = s_{66}\tau_{xy}$$

$$\begin{aligned} D_x &= d_{15}\tau_{zx} + \epsilon_{11}E_x \\ D_y &= d_{24}\tau_{yz} + \epsilon_{22}E_y \\ D_z &= d_{31}\sigma_x + d_{32}\sigma_y + d_{33}\sigma_z + \epsilon_{33}E_z \end{aligned} \tag{3}$$

In above expressions, D_i, σ_i and τ_{ij} are the electric displacement, normal stress and shear stress components, respectively. The piezoelectric strain constants d_{ij}, dielectric permittivities ϵ_{ij} (at constant stress field) and elastic compliances s_{ij} are given in Appendix A of the supplementary material.

The expression of E_x, E_y and E_z in terms of D_x, D_y and D_z can be obtained from Eq. (3). After putting these expressions of E_x, E_y and E_z into Eq. (2), we obtain

$$\begin{aligned} &\varepsilon_x = \bar{s}_{11}\sigma_x + \bar{s}_{12}\sigma_y + \bar{s}_{13}\sigma_z + \bar{d}_{31}D_z, && \varepsilon_y = \bar{s}_{12}\sigma_x + \bar{s}_{22}\sigma_y + \bar{s}_{23}\sigma_z + \bar{d}_{32}D_z \\ &\varepsilon_z = \bar{s}_{13}\sigma_x + \bar{s}_{23}\sigma_y + \bar{s}_{33}\sigma_z + \bar{d}_{33}D_z, && E_z = -\bar{d}_{31}\sigma_x - \bar{d}_{32}\sigma_y - \bar{d}_{33}\sigma_z + \bar{\epsilon}_{33}D_z \\ &\gamma_{yz} = \bar{s}_{44}\tau_{yz} + \bar{d}_{24}D_y, \quad \gamma_{zx} = \bar{s}_{55}\tau_{zx} + \bar{d}_{15}D_x, && E_x = \bar{\epsilon}_{11}D_x - \bar{d}_{15}\tau_{zx} \quad E_y = \bar{\epsilon}_{22}D_y - \bar{d}_{24}\tau_{yz} \end{aligned} \tag{4}$$

where

$$\begin{aligned} &\bar{\epsilon}_{33} = 1/\epsilon_{33}, \qquad \bar{s}_{ij} = s_{ij} - d_{3i}\bar{d}_{3j}, \quad \bar{d}_{3i} = d_{3i}/\epsilon_{33}, \qquad \text{for} \quad (i,j) = 1,2,3 \\ &\bar{s}_{44} = s_{44} - d_{24}\bar{d}_{24}, \qquad \bar{s}_{55} = s_{55} - d_{15}\bar{d}_{15}, \qquad \bar{s}_{66} = s_{66} \\ &\bar{\epsilon}_{11} = 1/\epsilon_{11}, \qquad \bar{\epsilon}_{22} = 1/\epsilon_{22}, \qquad \bar{d}_{24} = d_{24}/\epsilon_{22}, \qquad \bar{d}_{15} = d_{15}/\epsilon_{11}. \end{aligned}$$

These constitutive equations are valid for piezoelectric elastic layers having constant material properties.

For in-plane functionally graded layers, the elastic compliances and density of particular layer are considered to vary continuously and linearly along the (x) coordinate of the plate as [44, 74]

$$\begin{aligned} &\rho^m(\xi_1) = \rho(1 + \delta_p\,\xi_1) = \rho + \hat{\rho} \\ &\bar{s}^m_{1j}(\xi_1) = \bar{s}_{1j}(1 + \delta_1\xi_1) = \bar{s}_{1j} + \hat{s}_{1j} \quad \text{for} \quad j = 1,2,3; \\ &\bar{s}^m_{55}(\xi_1) = \bar{s}_{55}(1 + \delta_2\xi_1) = \bar{s}_{55} + \hat{s}_{55}; \quad \bar{s}^m_{66} = \bar{s}_{66}(1 + \delta_2\xi_1) = \bar{s}_{66} + \hat{s}_{66} \end{aligned} \tag{5}$$

Here δ_p denotes gradation index for density, δ_1 and δ_2 denote gradation indexes correspond to Young's and shear modulus, respectively. These gradation parameters (δ_p, δ_1 and δ_2) can have any positive and negative numerical value. This type of gradation is considered to provide flexibility to present mathematical model in considering different kind of variation in material properties. Therefore, the present mathematical model can be used for graded cases in which variation of material properties is introduced intentionally to achieve specific structural behaviour. Additionally, this formulation can also be used for degradation cases in which elastic properties of some specific layers may deteriorate due to dispersion of moisture or some chemicals such as hydrogen or due to periodic exposure to heat etc. Therefore, for in-plane functionally graded layers, Eq. (4) are modified and can be expressed as,

$$\begin{aligned} \varepsilon_x &= (\bar{s}_{11} + \hat{s}_{11})\sigma_x + (\bar{s}_{12} + \hat{s}_{12})\sigma_y + (\bar{s}_{13} + \hat{s}_{13})\sigma_z + \bar{d}_{31}D_z \\ \varepsilon_y &= (\bar{s}_{12} + \hat{s}_{12})\sigma_x + \bar{s}_{22}\sigma_y + \bar{s}_{23}\sigma_z + \bar{d}_{32}D_z \\ \varepsilon_z &= (\bar{s}_{13} + \hat{s}_{13})\sigma_x + \bar{s}_{23}\sigma_y + \bar{s}_{33}\sigma_z + \bar{d}_{33}D_z \\ E_z &= -\bar{d}_{31}\sigma_x - \bar{d}_{32}\sigma_y - \bar{d}_{33}\sigma_z + \bar{\epsilon}_{33}D_z \\ \gamma_{yz} &= (\bar{s}_{44} + \hat{s}_{44})\tau_{yz} + \bar{d}_{24}D_y, \qquad \gamma_{zx} = (\bar{s}_{55} + \hat{s}_{55})\tau_{zx} + \bar{d}_{15}D_x \\ E_x &= \bar{\epsilon}_{11}D_x - \bar{d}_{15}\tau_{zx} \qquad E_y = \bar{\epsilon}_{22}D_y - \bar{d}_{24}\tau_{yz} \end{aligned} \tag{6}$$

A 3D piezo-elasticity based extended Hamilton's principle in a mixed form, without any type of charge source and body force, can be expressed as,

$$\int_t \int_V [(\sigma_{ij,j} - \rho\ddot{u}_i)\delta u_i + (\varepsilon_{ij} - 0.5(u_{i,j} + u_{j,i}))\delta\sigma_{ij} + D_{i,i}\delta\phi - (E_i + \phi_{,i})\delta D_i]\mathrm{d}V\,\mathrm{d}t = 0, \tag{7}$$

where V is the volume ($a \times b \times h$) of the three-dimensional plate under consideration and i = 1, 2, 3 represent the x, y, z coordinate, respectively. Hence, $u_1 = u$, $u_2 = v$, $u_3 = w$, $\varepsilon_1 = \varepsilon_x$, $\varepsilon_2 = \varepsilon_y$, $\varepsilon_3 = \varepsilon_z$, $\varepsilon_{12} = \gamma_{xy}$, $\varepsilon_{23} = \gamma_{yz}$, $\varepsilon_{31} = \gamma_{zx}$, $\sigma_1 = \sigma_x$, $\sigma_2 = \sigma_y$, $\sigma_3 = \sigma_z$, $\sigma_{12} = \tau_{xy}$, $\sigma_{23} = \tau_{yz}$, $\sigma_{31} = \tau_{zx}$, $E_1 =$

E_x, $E_2 = E_y$, $E_3 = E_z$, $D_1 = D_x$, $D_2 = D_y$ and $D_3 = D_z$. Substituting the expressions of the electric components and strains from Eqs. (6) and (1) into Eq. (7) yields

$$\int_t\int_a\int_b\int_h [\delta u\{\tau_{xz,z} + \sigma_{x,x} + \tau_{xy,y} - (\rho+\hat{\rho})\ddot{u}\} + \delta v\{\tau_{yz,z} + \tau_{xy,x} + \sigma_{y,y} - (\rho+\hat{\rho})\ddot{v}\} + \delta w\{\sigma_{z,z} + \tau_{zx,x} + \tau_{yz,y} - (\rho+\hat{\rho})\ddot{w}\} + \delta\phi(D_{x,x} + D_{y,y} + D_{z,z}) + \delta\sigma_x\{(\bar{s}_{11}+\hat{s}_{11})\sigma_x + (\bar{s}_{12}+\hat{s}_{12})\sigma_y + (\bar{s}_{13}+\hat{s}_{13})\sigma_z + \bar{d}_{31}D_z - u_{,x}\} + \delta\sigma_y\{(\bar{s}_{12}+\hat{s}_{12})\sigma_x + \bar{s}_{22}\sigma_y + \bar{s}_{23}\sigma_z + \bar{d}_{32}D_z - v_{,y}\} - \delta\sigma_z\{w_{,z} - (\bar{s}_{13}+\hat{s}_{13})\sigma_x - \bar{s}_{23}\sigma_y - \bar{s}_{33}\sigma_z - \bar{d}_{33}D_z\} - \delta\tau_{yz}(v_{,z} + w_{,y} - \bar{s}_{44}\tau_{yz} - \bar{d}_{24}D_y) - \delta\tau_{zx}\{u_{,z} + w_{,x} - (\bar{s}_{55}+\hat{s}_{55})\tau_{zx} - \bar{d}_{15}D_x\} + \delta\tau_{xy}\{(\bar{s}_{66}+\hat{s}_{66})\tau_{xy} - v_{,x} - u_{,y}\} - \delta D_x(\phi_{,x} + \bar{\epsilon}_{11}D_x - \bar{d}_{15}\tau_{zx}) - \delta D_y(\phi_{,y} + \bar{\epsilon}_{22}D_y - \bar{d}_{24}\tau_{yz}) - \delta D_z(\phi_{,z} - \bar{d}_{31}\sigma_x - \bar{d}_{32}\sigma_y - \bar{d}_{33}\sigma_z + \bar{\epsilon}_{33}D_z)]\,\mathrm{d}z\,\mathrm{d}y\,\mathrm{d}x\,\mathrm{d}t = 0, \quad \forall\ \delta u_i,\ \delta\phi,\ \delta\sigma_i,\ \delta\tau_{ij},\ \delta D_i \tag{8}$$

The exterior surfaces of the plate (bottom-most and top-most surface) are shear traction free. Therefore, the boundary conditions of exterior surface at $z = \pm h/2$ can be expressed as,

$$\text{at} \quad z = \pm h/2: \quad \tau_{yz} = 0, \quad \tau_{zx} = 0, \qquad \sigma_z = 0 \tag{9}$$

If top or bottom surface is subjected to close-circuit (CC) condition then ϕ is prescribed. For open circuit condition D_z is prescribed. Therefore, for close-circuit surface $\phi(x, y)$=0 and for open-circuit surface $D_z(x, y)$= 0. For multilayered FGM plates, perfect bonding is assumed between different functionally graded layers. Therefore, following continuity condition is satisfied at each internal surface between kth and $(k + 1)$th layers

$$[(u,\, v,\, w,\, \phi,\, D_z,\, \sigma_z,\, \tau_{yz},\, \tau_{zx})|_{\zeta=1}]^{(k)} = [(u,\, v,\, w,\, \phi,\, D_z,\, \sigma_z,\, \tau_{yz},\, \tau_{zx})|_{\zeta=0}]^{(k+1)} \quad \text{for} \quad k = 1, ...L-1 \tag{10}$$

In the present mathematical model, interfaces of smart piezoelectric layers with IPFG elastic substrate are considered as grounded ($\phi = 0$) for better sensing. Note that when the interfaces between the piezoelectric layers and the elastic substrate are made grounded, the maximum potential difference will appear on top of the piezoelectric layer on the application of force. This is easier to evaluate accurately and effectively, which makes sensing better by easing the potential evaluation. Therefore, D_z becomes discontinuous at these interfaces. Subsequently, the continuity condition given in Eq. (10) is changed to $[\phi|_{\zeta=1}]^{(n_q)}$=0 *i.e.* $q = 1, \ldots, L_a$, where L_a expresses the piezo-elastic layer interface where actuation electric voltage/potential is prescribed.

The present investigation is for Levy-type boundary conditions, hence the two opposite ends of the IPFG laminate smart plate along y-direction (at $y = 0$ and $y = b$) are always considered under simply-supported and close-circuit conditions. Thus, $\sigma_y = w = u = 0$ at $y = 0$ and b for all x, z of that plane. The other two opposite edges of hybrid FGM plate can have any type of mechanical and electrical support conditions. The mechanical support conditions at the edges $\xi_1 = 0$ and 1 can be clamped ($w = u = v = 0$), free ($\sigma_x = \tau_{xz} = \tau_{xy} = 0$) or simply-supported ($\sigma_x = w = v = 0$) at each point of corresponding $y - z$ plane. The ends of piezo-electric layers can have closed circuit (CC) condition (ϕ=0) or open circuit (OC) condition (D_x=0).

3 Formulation for viscoelastic analysis

First classical elasticity analysis is performed in which instantaneous stresses within a material are considered only function of instantaneous strains, as presented in the preceding section. Now to implement viscoelasticity of material in the analysis, instantaneous stresses are assumed as a function of strains history by employing linear viscoelastic model. In a simplified linear viscoelastic mathematical model, the stress $\sigma(t)$ at any point within the structure is a function of time and can be written in the form of convolution integral on the kernel function [75] as

$$\sigma_t(t) = g_t(t) \circledast \varepsilon(t) \tag{11}$$

In above equation, $t \in \mathbb{R}^+$ is the dimensionless time parameter, $\sigma(t)$ and $\varepsilon(t)$ are representing time-dependent stress and strain, respectively. Here, it is assumed that the strain is zero for negative times. Hence, the initial strain is $\varepsilon_t = 0$ for $t < 0$ and g_t is the kernel or memory function. Causality requirements enforce g_t to be a causal function *i.e.*, it vanishes for $t < 0$; $g_t(t) = 0, \forall t < 0$. This approach of deriving time-dependent stress equations in the context of linear viscoelasticity is known as the hereditary approach,

which gives greater freedom in constructing viscoelastic models as compared to the differential approach that only relies on the concepts of certain springs and dashpots combinations. Hence, time-dependent stress-strain relationship of Eq. (11) can directly be used for dynamic investigation of a solid viscoelastic body. Such as, in case of its implementation to uniform bar, Eq. (11) must be multiplied by its cross-section area which give the displacement and force rate (or velocity). In Eq. (11), $g_t(t)$ is also known as 'relaxation function', 'after-effect function' or 'hereditary function' in the context of different fields. Generally for the simplicity, the kernel function ($g_t(t)$) is usually described in the frequency domain which is also known as Laplace domain form. Hence, Laplace transformation of Eq. (11) converts it into frequency domain which can be expressed as

$$\bar{\sigma_s}(s_L) = s_L \bar{G}_s(s_L) \bar{\varepsilon_s}(s_L) \tag{12}$$

Here $s_L \in \mathbb{C}$ represents complex Laplace domain parameter. The parameters $\bar{\sigma_s}(s_L)$, $\bar{G}_s(s_L)$ and $\bar{\varepsilon_s}(s_L)$ are representing the corresponding Laplace transformation of $\sigma_t(t)$, $g_t(t)$ and $\varepsilon_t(t)$. The kernel function $g_t(t)$ can be constructed by two generally used methods one is approximation based mathematical approach and the other is general mathematical approach.

3.1 Construction of the kernel function using approximation based mathematical approach

In the approximation based mathematical approach, different combinations of springs and dashpots are used to obtain kernel function for viscoelastic constitutive relationship. Though a variety of springs and dashpots based models can be constructed by considering different arrangements, but for viscoelastic analysis of solid body generally four models [76, 77] are used which are known as Maxwell viscoelastic model, Voigt viscoelastic model, Standard linear viscoelastic model and Generalised Maxwell viscoelastic model, as shown in Fig. 2. Here, Dirac delta function $\delta(t)$ and unit step function $\mathbb{U}(t)$ are defined as below

$$\mathbb{U}(t) = 1 \quad \text{if} \quad t \geq 0, \qquad \text{and} \qquad 0 \quad \text{if} \quad t < 0. \tag{13}$$

$$\delta(t) \circledast f_t(t) = f_t(t) \tag{14}$$

Here, $\delta(t)$ represents the Dirac delta function and $f_t(t)$ continuous generalized function. Dirac's delta $\delta(t)$ distribution represents the unit impulse function which is a generalized function or distribution over the real numbers [78, 79]. Based on these assumptions, the viscoelastic kernel function ($g_t(t)$) for the four models can be expressed [75–77] as

- *Maxwell viscoelastic model:*

$$g_t(t) = \mu e^{-(\mu/\eta)t} \mathbb{U}(t) \tag{15}$$

- *Voigt viscoelastic model:*

$$g_t(t) = \eta \delta(t) + \mu \mathbb{U}(t) \tag{16}$$

- *Standard linear model:*

$$g_t(t) = E_R \left[1 - (1 - \frac{\tau_\sigma}{\tau_{\bar{\varepsilon}_s}}) e^{-t/\tau_{\bar{\varepsilon}_s}} \right] \mathbb{U}(t) \tag{17}$$

- *Generalised Maxwell viscoelastic model:*

$$g_t(t) = \left[\sum_{j=1}^{n} \mu_j e^{-(\mu_j/\eta_j)t} \right] \mathbb{U}(t) \tag{18}$$

This models is also called as the Prony series viscoelastic model.

These functions are obtained by assuming the equilibrium of different forces coming from stretching of the dashpots and springs as given in Fig. 2. In these functions, t is time, $\sigma(t)$ is stress, $\varepsilon(t)$ is strain of system, η is viscosity parameter of material represented by a purely viscous damper in the dashpots-springs system, μ is elastic stiffness parameter of material represented by a purely elastic spring in the dashpots-springs system, τ denotes relaxation time constant and E_R represents relaxation modulus.

3.2 Mathematical depiction of the kernel function in the frequency domain

The kernel function $g_t(t)$ in Eq. (12) can also be represented in the frequency (ω_s) state. It is a complex function which can be denoted as,

$$\bar{G}_s(\omega_s) = \bar{G}_s(\iota\omega_s) = G_s(\omega_s) \tag{19}$$

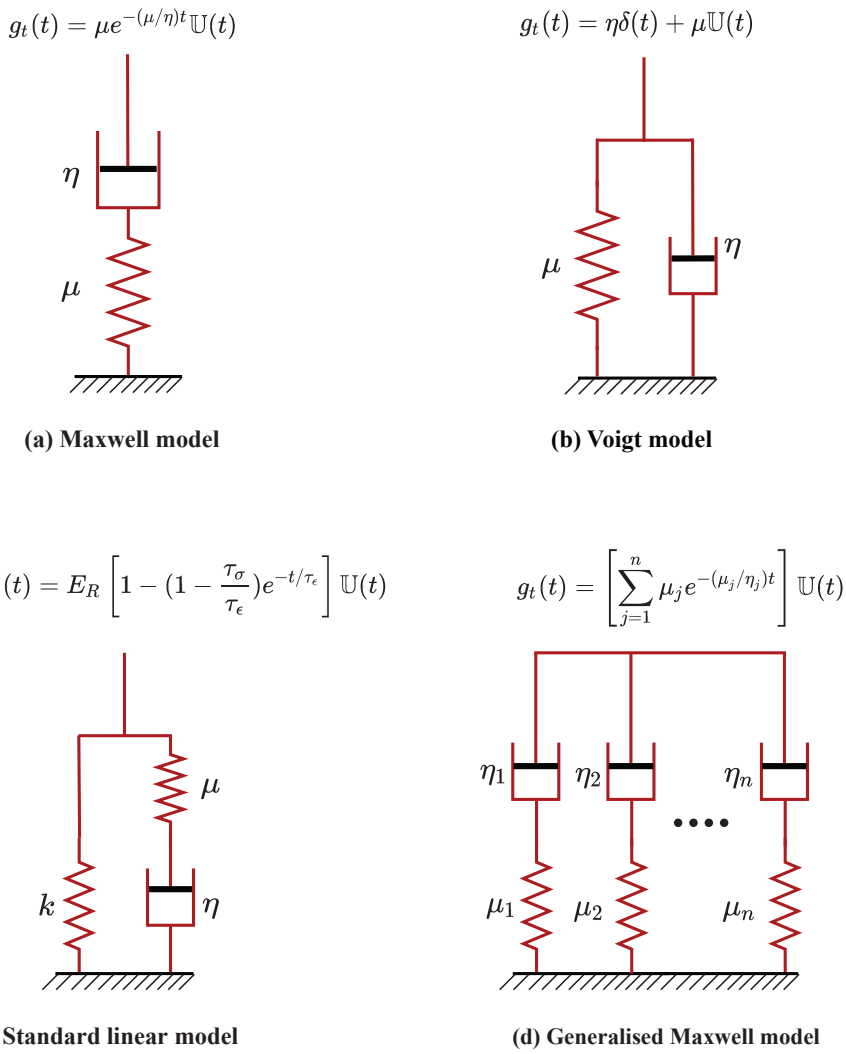

(a) Maxwell model **(b) Voigt model**

(c) Standard linear model **(d) Generalised Maxwell model**

Fig. 2: Representation of viscoelastic materials models using springs and dashpots arrangement.

Here $\omega_s \in \mathbb{R}^+$ represents the frequency of Laplace domain signal. The complex function $G_s(\omega_s)$ can be split into real and imaginary part and can be also represented in term of amplitude and phase angle as,

$$G_s(\omega_s) = G'_s(\omega_s) + \iota G''_s(\omega_s) = |G_s(\omega_s)|e^{\iota\phi_s(\omega_s)} \tag{20}$$

Real part $G'_s(\omega_s)$ is known as storage moduli and imaginary part $G''_s(\omega_s)$ is known as loss moduli. The kernel function has one main restriction, which comes from the relationship between cause and effect that the reaction of the structure depends upon its loading history.The output of a function at any time depends on past and present values of input which is known as causality condition and causal system. A causal system (also known as a physical or non-anticipative system) is a system where the output depends on past and current inputs but not future inputs—i.e., the output $y(t_0)$ depends only on the input $x(t)$ for values of $t \leq t_0$ [79]. Therefore, according to the causality condition, the structure's reaction should depend upon its loading history. Further, the Kramers-Kronig relation [79] defines the mathematical correlation between the imaginary and real parts of the complex elasticity modulus (complex modulus)[71, 79]. Kramers-Kronig interrelations show that the imaginary and real parts of complex elasticity modulus must be linked by a Hilbert transform duo and it could be written mathematically as

$$G'_s(\omega_s) = G_{s\infty} + \frac{2}{\pi}\int_0^\infty \frac{uG''_s(u_s)}{\omega_s^2 - u_s^2}\,\mathrm{d}u_s \tag{21}$$

$$G''_s(\omega_s) = \frac{2\omega_s}{\pi}\int_0^\infty \frac{G'_s(u_s)}{u_s^2 - \omega_s^2}\,\mathrm{d}u_s \tag{22}$$

where $G_{s\infty} = G_s(\omega_s \to \infty) \in \mathbb{R}$ represents unrelaxed modulus. The integral in the Eqs. (21) and (22) is evaluated in Cauchy's principal value sense near the singularity [79–81]. The behavior of visco-elastic

material in the present case is considered to correspond to various spring dashpot combinations. Therefore, the reference signal has come from the corresponding spring-dashpot oscillator, where the real and imaginary parts bear the meaning according to the conventional signal processing literature [71, 79]. The equivalent relationships which is linking the modulus $|G_s'(\omega_s)|$ and the phase $\phi_s(\omega_s)$ of $G_s(\omega_s)$ can be expressed as [Remark 4 and 5, Appendix G (refer to the Supplementary material)],

$$\ln|G_s'(\omega_s)| = \ln|G_{s\infty}| + \frac{2}{\pi}\int_0^\infty \frac{u_s\phi_s(u_s)}{\omega_s^2-u_s^2}\,\mathrm{d}u_s \tag{23}$$

$$\phi_s(\omega_s) \quad = \frac{2\omega_s}{\pi}\int_0^\infty \frac{\ln|G_s(u_s)|}{u_s^2-\omega_s^2}\,\mathrm{d}u_s \tag{24}$$

It is worth mentioning that the approximation based principle described above to drive complex elasticity modulus automatically satisfy these conditions. However, other functions are also there which can also satisfy these conditions. The determination of $G_s(\omega_s)$, which satisfy these conditions, through experimental measurements is also possible [79, 82]. The most commonly used functions in literature are listed in Table 1.

Table 1: Representation of complex elasticity modulus for different viscoelastic material models in the Laplace or frequency domain.

Viscoelastic model	Complex elasticity modules
Biot model [83]	$G_s(\omega_s) = G_{s0} + \sum_{k=1}^{n} \frac{a_k \iota\omega_s}{\iota\omega_s + b_k}$
Fractional derivative [84]	$G_s(\omega_s) = \frac{G_{s0}+G_{s\infty}(\iota\omega_s\tau)^\beta}{1+(\iota\omega_s\tau)^\beta}$
ADF [85]	$G_s(\omega_s) = G_{s0}\left[1 + \sum_{k=1}^{n} \Delta_k \frac{\omega_s^2+\iota\omega_s\Omega_{sk}}{\omega_s^2+\Omega_{sk}^2}\right]$
GHM [86]	$G_s(\omega_s) = G_{s0}\left[1 + \sum_k \alpha_k \frac{-\omega_s^2+2\iota\xi_k\omega_{sk}\omega_s}{-\omega_s^2+2\iota\xi_k\omega_{sk}\omega_s+\omega_{sk}^2}\right]$
Step-function [87]	$G_s(\omega_s) = G_{s0}\left[1 + \eta\frac{1-e^{-\omega_s t_0}}{\omega_s t_0}\right]$
Half cosine model [87]	$G_s(\omega_s) = G_{s0}\left[1 + \eta\frac{1+2(\omega_s t_0/\pi)^2-e^{-\omega_s t_0}}{1+2(\omega_s t_0/\pi)^2}\right]$
Gaussian model [88]	$G_s(\omega_s) = G_{s0}\left[1 + \eta\, e^{\omega_s^2/4\mu}\left\{1-\mathrm{erf}\left(\frac{\iota\omega_s}{2\sqrt{\mu}}\right)\right\}\right]$

3.3 Effective material properties of viscoelastic layers in the laminated plate

In this paper, it is considered that each Young's moduli E_i $(E_1, E_2,\ E_3)$ and each shear moduli G_{ij} (G_{12}, G_{13}, G_{23}) of viscoelastic layer is modelled using viscoelastic properties. The Biot model (mentioned in Table 1) with only one term has been used for computational simplicity. Hence, complex elastic and shear modulus in frequency domain [75] can be expressed as

$$E_i(\omega_s) = (E_s)_i\left(1 + \bar{\varepsilon}_s\frac{\iota\omega_s}{\mu+\iota\omega_s}\right) \tag{25}$$

$$G_{ij}(\omega_s) = (G_s)_{ij}\left(1 + \bar{\varepsilon}_s\frac{\iota\omega_s}{\mu+\iota\omega_s}\right) \tag{26}$$

where E_i represents the elastic modulus of the orthotropic layers considering viscoelasticity and $(E_s)_i$ represents the elastic modulus in absence of viscoelasticity. Similarly, G_{ij} represents the shear modulus of the orthotropic layers when viscoelasticity is considered and $(G_s)_{ij}$ represents the shear modulus in absence of viscoelasticity. In these expressions, μ is the relaxation parameter and $\bar{\varepsilon}_s$ represents a constant defining the 'strength' of viscosity. The amplitude of complex elastic moduli and shear moduli [75] is given by

$$|E_i(\omega_s)| = E_{si}\sqrt{\frac{\mu^2+\omega_s^2\left(1+\bar{\varepsilon}_s\right)^2}{\mu^2+\omega_s^2}} \tag{27}$$

$$|G_{ij}(\omega_s)| = G_{sij}\sqrt{\frac{\mu^2+\omega_s^2\left(1+\bar{\varepsilon}_s\right)^2}{\mu^2+\omega_s^2}} \tag{28}$$

The phase (ϕ_s) [75] of these complex elastic moduli and shear moduli are given by

$$\phi_s\left(E_i(\omega_s)\right) = \phi_s\left(G_{ij}(\omega_s)\right) = \tan^{-1}\left(\frac{\mu\bar{\varepsilon}_s\omega_s}{\mu^2+\omega_s^2(1+\bar{\varepsilon}_s)}\right) \tag{29}$$

The complex elastic and shear moduli have the various limiting properties which are providing critical insights for various special cases. These limiting properties are listed in Appendix B (refer to the Supple-

mentary material).

3.3.1 Numerical transformation of frequency domain into the time domain

The objective of the present paper is to present the time-dependent viscoelastic behavior. Therefore, once the Frequency (Laplace) domain solutions are obtained using the viscoelastic correspondence principle, as described in the preceding subsection, they are inverted back into the time domain. The Inversion of frequency domain data into the time-domain is performed by employing the computationally efficient inverse Fourier transform (IFFT) [89, 90]. The physical interpretation of time signal into the Fourier transform can be expressed as

$$E_i(t) = \frac{1}{2\pi}\int_{-\infty}^{\infty} E_i(\omega_s)e^{\iota\omega_s t}\mathrm{d}\omega = \int_{-\infty}^{\infty} E_i(2\pi f_s)e^{2\pi\iota f_s t}\mathrm{d}f_s \tag{30}$$

$$G_{ij}(t) = \frac{1}{2\pi}\int_{-\infty}^{\infty} G_{ij}(\omega_s)e^{\iota\omega_s t}\mathrm{d}\omega = \int_{-\infty}^{\infty} G_{ij}(2\pi f_s)e^{2\pi\iota f_s t}\mathrm{d}f_s \tag{31}$$

Here, $E_i(t)$ and $G_{ij}(t)$ represent relaxation elastic and shear moduli for composite orthotropic layers. The physical interpretation of an equation indicates the act of establishing the relation between the physical quantities in the equation by expecting how the system will behave at extreme or normal conditions. It can involve some approximations of the equation. The main characteristics of materials with viscoelasticity are used to describe the stress relaxation of materials with time (t). The efficient determination of $E_i(t)$ and $G_{ij}(t)$ must accurately simulate the viscoelastic deformation and stress relaxation in the material. Since in the inversion, discrete numerical data of frequency domain is used rather than a continuous expression for computation convenience, the continuous inverse Fourier transform can be expressed by its discrete counterpart as,

$$E_i(t) = \sum_{n=-\infty}^{\infty} C_n^E e^{\iota 2\pi n t} \quad \text{and} \quad G_{ij}(t) = \sum_{n=-\infty}^{\infty} C_n^G e^{\iota 2\pi n t} \tag{32}$$

where coefficients C_n^E and C_n^G are given by,

$$C_n^E = |E_i(\omega_{s_n})|\ e^{\iota\phi(E(\omega_{s_n}))} \tag{33}$$

$$C_n^G = |G_{ij}(\omega_{s_n})|\ e^{\iota\phi(G(\omega_{s_n}))} \tag{34}$$

It shows that whether the signal is periodic or not, its time waveform can be represented in the form of amplitude $|E(\omega_{s_n})|$ and phase $\phi\left(E(\omega_{s_n})\right)$. For more information on the relationships between the continuous and discrete Fourier transform, one can refer to [91]. While inverting the frequency domain data into the time domain, all values (higher to lowest) of the parameter ω_s are considered. So the time domain signal shows oscillation at each time step and to smoothen this time signal Savitzky-Golay smoothing algorithm is used here.

4 EKM-Fourier series based analytical solution approach

In the present mathematical model both mechanical and electrical variables are considered as primary variables. Thus, the mechanical displacements variables (u, v, w), electrical variables (ϕ, D_x, D_y and D_z) and the stresses variables (σ_x, σ_y, σ_z, τ_{xy}, τ_{yz}, τ_{zx}) are functions of ξ_1, ξ_2, and ζ, and solved as primary variables using combination of extended Kantorovich method and Fourier series approach, as further explained in this section.

To obtain the solution for y-direction, Fourier series approach is utilized and solution is assumed in form of Fourier series in such a manner that it satisfies simply-supported end conditions ($\sigma_y = w = u = 0$ at edges $\xi_2 = 0, 1$) of y direction [Remark 3: Appendix G (supplementary material)],

$$[u,\ w,\ \sigma_x,\ \sigma_y,\ \sigma_z,\ \tau_{zx},\ \phi,\ D_x,\ D_z] = \sum_{m=1}^{M_y} [(u,\ w,\ \sigma_x,\ \sigma_y,\ \sigma_z,\ \tau_{zx},\ \phi,\ D_x,\ D_z)_m \cos\omega t] \sin m\pi\xi_2$$

$$[v,\ \tau_{yz},\ \tau_{xy},\ D_y] = \sum_{m=1}^{M_y} [(v,\ \tau_{yz},\ \tau_{xy},\ D_y)_m \cos\omega t] \cos m\pi\xi_2 \tag{35}$$

where M_y represents the number of term in Fourier series and $(\ )_m$ denotes the mth term of Fourier series, and it is the function of ξ_1 and ζ. The truncated Fourier series is used where truncation of series (no. of

terms in Fourier series) is corresponding to the flexural vibration mode of y-directions. A rectangular plate can have infinite flexural vibration modes along any direction. Hence, for general case $M_y \to \infty$. However, as in engineering application, the interest is over finite number of fundamental modes, the series has usually finite number of terms depending on the vibration modes of interest. Further, we substitute these Fourier series assumption, given in Eq. (35), into the extended Hamilton's principle expressed in Eq. (8). It transforms Eq. (8) into the following form, due to the orthogonality of cosine and sine functions,

$$\int_t\int_a\int_h [\delta u_m\{\tau_{xz_m,z} + \sigma_{x_m,x} - \bar{m}\tau_{xy_m} - (\rho+\hat{\rho})\omega^2 u_m\} + \delta v_m(\tau_{yz_m,z} + \tau_{xy_m,x} + \bar{m}\sigma_{y_m} - (\rho+\hat{\rho})\omega^2 v_m)$$
$$+\delta w_m\{\sigma_{z_m,z} + \tau_{zx_m,x} - \bar{m}\tau_{yz_m} - (\rho+\hat{\rho})\omega^2 w_m\} + \delta\phi_m(D_{x_m,x} - \bar{m}D_{y_m} + D_{z_m,z}) + \delta\sigma_{x_m}((\bar{s}_{11}+\hat{s}_{11})\sigma_{x_m}$$
$$+(\bar{s}_{12}+\hat{s}_{12})\sigma_{y_m} + (\bar{s}_{13}+\hat{s}_{13})\sigma_{z_m} + \bar{d}_{31}D_{z_m} - u_{m,x}) + \delta\sigma_{y_m}((\bar{s}_{12}+\hat{s}_{12})\sigma_{x_m} + \bar{s}_{22}\sigma_{y_m} + \bar{s}_{23}\sigma_{z_m} + \bar{d}_{32}D_{z_m}$$
$$+\bar{m}v_m) - \delta\sigma_{z_m}(w_{m,z} - (\bar{s}_{13}+\hat{s}_{13})\sigma_{x_m} - \bar{s}_{23}\sigma_{y_m} - \bar{s}_{33}\sigma_{z_m} - \bar{d}_{33}D_{z_m}) - \delta\tau_{yz_m}(v_{m,z} + \bar{m}w_m - \bar{s}_{44}\tau_{yz_m}$$
$$-\bar{d}_{24}D_{y_m}) - \delta\tau_{zx_m}(u_{m,z} + w_{m,x} - (\bar{s}_{55}+\hat{s}_{55})\tau_{zx_m} - \bar{d}_{15}D_{x_m}) + \delta\tau_{xy_m}((s_{66}+\hat{s}_{66})\tau_{xy_m} - v_{m,x} - \bar{m}u_m)$$
$$-\delta D_{x_m}(\phi_{m,x} + \bar{\epsilon}_{11}D_{x_m} - \bar{d}_{15}\tau_{zx_m}) - \delta D_{y_m}(\bar{m}\phi_m + \bar{\epsilon}_{22}D_{y_m} - \bar{d}_{24}\tau_{yz_m}) - \delta D_{z_m}(\phi_{m,z} - \bar{d}_{31}\sigma_{x_m} - \bar{d}_{32}\sigma_{y_m}$$
$$-\bar{d}_{33}\sigma_{z_m} + \bar{\epsilon}_{33}D_{z_m})]\mathrm{d}z\mathrm{d}x\mathrm{d}t = 0, \quad \forall \quad \delta u_{i_m}, \delta\phi_m, \delta\sigma_{i_m}, \delta\tau_{ij_m}, \delta D_{i_m} \qquad \text{where} \quad \bar{m} = m\pi/b \tag{36}$$

The above expression appears for every Fourier term. Now dependency of each variable is reduced and all primary field variables, $\mathbf{X} = [\, u_m \quad v_m \quad w_m \quad \sigma_{x_m} \quad \sigma_{y_m} \quad \sigma_{z_m} \quad \tau_{xy_m} \quad \tau_{yz_m} \quad \tau_{zx_m} \quad \phi_m \quad D_{x_m} \quad D_{y_m} \quad D_{z_m} \,]^{\mathrm{T}}$ are function of ξ_1 (x-coordinate) and ζ (thickness coordinate) only. The solution along these two-directions (for x and z- direction) is obtained further by employing recently developed the multi-term extended Kantorovich method [34, 38, 40, 44, 74, 92]. The solution of X_l, lth variable $\mathbf{X}$, is assumed as the summation of n terms series containing products of two separable unknown functions $g_l^i(\zeta)$ and $f_l^i(\xi_1)$. Thus, the solution of each X_l variable can be expressed for the kth layer as,

$$X_{l_m}(\xi_1,\zeta) = \sum_{i=1}^{n} f_{l_m}^i(\xi_1) g_{l_m}^i(\zeta) \qquad \text{for} \quad l = 1, 2, \ldots 13 \tag{37}$$

Here, $f_l^i(\xi_1)$ acts as global variable and is valid for all layers, while $g_l^i(\zeta)$ acts as local variable which is valid separately for every local k^{th} layer. In the next sections, subscript 'm' is dropped from the mathematical expressions of $f_{l_m}^i$ and $g_{l_m}^i$ for convenience. Now, the solutions for unknown functions $g_l^i(\zeta)$ and $f_l^i(\xi_1)$ are obtained in two iterative steps.

4.1 First iterative step - solving functions $g_l^i(\zeta)$

In this iteration step, thickness function $g_l^i(\zeta)$ is solved. To start the first iteration step, $f_l^i(\xi_1)$ is assumed in sine and cosine form. In present EKM approach, the assumed initial functions need not satisfy any natural and essential boundary condition and it can be chosen arbitrarily. But for better convergence and to reduce the number of iteration for accurate solution, the $f_l^i(\xi_1)$ function is assumed corresponding to simply-supported boundary conditions of edges $\xi_1 = 0$ and 1. Hence, the initial functions $f_l^i(\xi_1)$ to the start the first step of iteration 1 can be assumed as $f_1^i(\xi_1) = f_7^i(\xi_1) = f_9^i(\xi_1) = f_{11}^i(\xi_1) = \cos i\pi\xi_1$; $f_2^i(\xi_1) = f_3^i(\xi_1) = f_4^i(\xi_1) = f_5^i(\xi_1) = f_6^i(\xi_1) = f_8^i(\xi_1) = f_{12}^i(\xi_1) = f_{13}^i(\xi_1) = \sin i\pi\xi_1$. Here, $f_1(\xi_1)$, $f_2(\xi_1)$, $f_3(\xi_1)$, $f_4(\xi_1)$, $f_5(\xi_1)$, $f_6(\xi_1)$, $f_7(\xi_1)$, $f_8(\xi_1)$, $f_9(\xi_1)$, $f_{10}(\xi_1)$, $f_{11}(\xi_1)$, $f_{12}(\xi_1)$ and $f_{13}(\xi_1)$ denote in-plane function for u, v, w, σ_x, σ_y, σ_z, τ_{xy}, τ_{yz}, τ_{zx}, ϕ, D_x, D_y and D_z, respectively. Now functions $g_l^i(\zeta)$ have to be solved in this iteration step, for which variation δX_l can be expressed as,

$$\delta X_l(\xi_1,\zeta) = \sum_{i=1}^{n} f_l^i(\xi_1)\delta g_l^i, \qquad\qquad l = 1, 2, \ldots 13 \tag{38}$$

The functions $g_l^i(\zeta)$ can be divided into two parts $\bar{\mathbf{G}}$ and $\hat{\mathbf{G}}$. Here $\bar{\mathbf{G}}$ column vector is of dimension $8n$ and has the specfic independent variables that comes in the interface condition, and mechanical/electrical boundary conditions at exterior surfaces (top and bottom) of hybrid FGM plate. The other $\hat{\mathbf{G}}$ column vector is of size $5n$ and has the other left over dependent variables,

$$\bar{\mathbf{G}} = [\, g_1^1 \ldots g_1^n \quad g_2^1 \ldots g_2^n \quad g_3^1 \ldots g_3^n \quad g_6^1 \ldots g_6^n \quad g_8^1 \ldots g_8^n \quad g_9^1 \ldots g_9^n \quad g_{10}^1 \ldots g_{10}^n \quad g_{13}^1 \ldots g_{13}^n \,]^{\mathrm{T}}$$
$$\hat{\mathbf{G}} = [\, g_4^1 \ldots g_4^n \quad g_5^1 \ldots g_5^n \quad g_7^1 \ldots g_7^n \quad g_{11}^n \ldots g_{11}^n \quad g_{12}^n \ldots g_{12}^n \,]^{\mathrm{T}} \tag{39}$$

Now assumed solution Eq. (37), and its variational part Eq. (38) are substituted into Eq. (36). However, variations in δg_l^i functions are arbitrary, hence the coefficients of δg_l^i should be equal to zero individually

according to fundamental lemma of variational principles. It leads to the following set of $8n$ first-order coupled ODEs and $5n$ coupled linear-algebraic equations for every layer,

$$\mathbf{M}\bar{\mathbf{G}}_{,\zeta} = \bar{\mathbf{A}}^{\mathbf{m}}(\omega)\bar{\mathbf{G}} + \hat{\mathbf{A}}^{\mathbf{m}}\hat{\mathbf{G}} \tag{40}$$

$$\mathbf{K}^{\mathbf{m}}\hat{\mathbf{G}} = \tilde{\mathbf{A}}^{\mathbf{m}}\bar{\mathbf{G}} \tag{41}$$

Here, $\mathbf{M}_{8n\times 8n}$, $\bar{\mathbf{A}}_{8n\times 8n}$, $\hat{\mathbf{A}}_{8n\times 5n}$, $\mathbf{K}_{5n\times 5n}$, and $\tilde{\mathbf{A}}_{5n\times 8n}$ are coefficient matrices, wherein $\bar{\mathbf{A}}^{\mathbf{m}} = \bar{\mathbf{A}} + \bar{\mathbf{A}}^{\mathbf{v}}$; $\hat{\mathbf{A}}^{\mathbf{m}} = \hat{\mathbf{A}} + \hat{\mathbf{A}}^{\mathbf{v}}$; $\mathbf{K}^{\mathbf{m}} = \mathbf{K} + \mathbf{K}^{\mathbf{v}}$; $\tilde{\mathbf{A}}^{\mathbf{m}} = \tilde{\mathbf{A}} + \tilde{\mathbf{A}}^{\mathbf{v}}$. The non-zero elements of coefficient matrices of Eqs. (40) and (41) ($\mathbf{M}$, $\bar{\mathbf{A}}$, $\bar{\mathbf{A}}^{\mathbf{v}}$, $\hat{\mathbf{A}}$, $\hat{\mathbf{A}}^{\mathbf{v}}$, $\mathbf{K}^{\mathbf{m}}$, $\tilde{\mathbf{A}}$, $\tilde{\mathbf{A}}^{\mathbf{v}}$) are listed in Appendix C (refer to the supplementary material). Since the functions f_l^i are presumed for first starting iteration, the coefficient elements of Eqs. (40) and (41) could be solved in closed-form by performing integration along x-direction. Hence, coefficients of Eq. (40) and Eq. (41) are now known. The substitution of $\hat{\mathbf{G}}$ from Eq. (41) into Eq. (40), transforms equation (40) to the following form,

$$\bar{\mathbf{G}}_{,\zeta} = \mathbf{A}(\omega)\bar{\mathbf{G}}, \qquad \text{Here,} \qquad \mathbf{A} = \mathbf{M}^{-1}[\bar{\mathbf{A}}^{\mathbf{m}} + \hat{\mathbf{A}}^{\mathbf{m}}\mathbf{K}^{\mathbf{m}^{-1}}\tilde{\mathbf{A}}^{\mathbf{m}}] \tag{42}$$

Above Eq. (42) is a set of $8n$ first-order coupled ODEs with constant coefficients and this system of ODEs can be solved analytically by following solution approach suggested by Kumari and Behera [93] which is further explained in Appendix D (refer to the supplementary material).

4.2 Second iterative step - solving functions $f_l^i(\xi_1)$

In the first iterative step, $g_l^i(\zeta)$ functions are obtained in closed-form. Now, in the second iteration these obtained $g_l^i(\zeta)$ functions are used to obtain f_l^i functions, which are assumed as unknown in this iteration. Therefore, variation is assumed in g_l^i functions and hence $\delta\mathbf{X_l}$ can be expressed as,

$$\delta X_l(\xi_1,\zeta) = \sum_{i=1}^{n} g_l^i(\zeta)\delta f_l^i \qquad \text{for} \quad l = 1,2,\ldots,13 \tag{43}$$

Similar to first iteration, the in-plane functions $f_l^i(\xi_1)$ can also be split-up into two column vectors $\hat{\mathbf{F}}$ and $\bar{\mathbf{F}}$. Here, $\bar{\mathbf{F}}$ contains the specific independent variables that appear in the mechanical and electrical boundary conditions along x-directions at ξ_1=0 and 1. The $\hat{\mathbf{F}}$ column vector contains the remaining dependent variables. Hence,

$$\begin{aligned}\bar{\mathbf{F}} &= [\, f_1^1 \ldots f_1^n \quad f_2^1 \ldots f_2^n \quad f_3^1 \ldots f_3^n \quad f_4^1 \ldots f_4^n \quad f_7^1 \ldots f_7^n \quad f_9^1 \ldots f_9^n \quad f_{10}^1 \ldots f_{10}^n \quad f_{11}^1 \ldots f_{11}^n \,]^{\mathrm{T}} \\ \hat{\mathbf{F}} &= [\, f_5^1 \ldots f_5^n \quad f_6^1 \ldots f_6^n \quad f_8^1 \ldots f_8^n \quad f_{12}^1 \ldots f_{12}^n \quad f_{13}^1 \ldots f_{13}^n \,]^{\mathrm{T}}\end{aligned} \tag{44}$$

Substituting Eq. (43) and Eq. (37) in Eq. (36), and equating the coefficient of δf_l^i to zero individually, lead to a set of differential-algebraic equations as,

$$\mathbf{N}\bar{\mathbf{F}}_{,\xi_1} = \{\bar{\mathbf{B}}(\omega) + \xi_1\bar{\mathbf{B}}^{\mathbf{v}}(\omega)\}\bar{\mathbf{F}} + (\hat{\mathbf{B}} + \xi_1\hat{\mathbf{B}}^{\mathbf{v}})\hat{\mathbf{F}} \tag{45}$$

$$\mathbf{L}\hat{\mathbf{F}} = (\tilde{\mathbf{B}} + \xi_1\tilde{\mathbf{B}}^{\mathbf{v}})\bar{\mathbf{F}} \tag{46}$$

where $\mathbf{N}_{8n\times 8n}$, $\bar{\mathbf{B}}_{8n\times 8n}$, $\bar{\mathbf{B}}^{\mathbf{v}}_{8n\times 8n}$, $\hat{\mathbf{B}}_{8n\times 5n}$, $\hat{\mathbf{B}}^{\mathbf{v}}_{8n\times 5n}$, $\mathbf{L}_{5n\times 5n}$, $\tilde{\mathbf{B}}_{5n\times 8n}$ and $\tilde{\mathbf{B}}^{\mathbf{v}}_{5n\times 8n}$ are coefficient matrices and all non-zero elements of these matrices are listed in Appendix E (refer to the supplementary material). However, $g_l^i(\zeta)$ are already known in closed-form from previous iteration, hence all elements of the coefficient matrices can also be solved exactly in closed form by executing integration over ζ direction on the known g_l^i functions. Then, substitution of algebraic equation (46) into Eq. (45) leads to,

$$\bar{\mathbf{F}}_{,\xi_1} = \{\mathbf{B_0}(\omega) + \xi_1\mathbf{B_1}(\omega) + \xi_1^2\mathbf{B_2}\}\bar{\mathbf{F}} \tag{47}$$

Here $\mathbf{B_0} = \mathbf{N^{-1}}(\bar{\mathbf{B}} + \hat{\mathbf{B}}\mathbf{L^{-1}}\tilde{\mathbf{B}})$, $\mathbf{B_2} = \mathbf{N^{-1}}(\hat{\mathbf{B}}^{\mathbf{v}}\mathbf{L^{-1}}\tilde{\mathbf{B}}^{\mathbf{v}})$, $\mathbf{B_1} = \mathbf{N^{-1}}(\bar{\mathbf{B}}^{\mathbf{v}} + \hat{\mathbf{B}}\mathbf{L^{-1}}\tilde{\mathbf{B}}^{\mathbf{v}} + \hat{\mathbf{B}}^{\mathbf{v}}\mathbf{L^{-1}}\tilde{\mathbf{B}})$. The above Eq. (47) represents coupled system of first-order differential equations ($8n$) having variable coefficients which are function of ξ_1. This couple system ODEs cannot be solved exactly using traditional approaches. Therefore, solution of Eq. (47) has been obtained by utilizing a modified power series approach recently developed by Singh and Kumari et al. [44, 74], which is explained in Appendix F (Supplementary material). After obtaining $\bar{\mathbf{F}}$ functions in closed-form, further they have been used to obtain the $\hat{\mathbf{F}}$ functions using Eq. (46). In this way second iterative step is completed which gives solution along in-plane (x) direction. These two iteration steps, first for thickness functions g_l^i which is explained in (Sec. 4.1), and second for f_l^i functions which is explained in (Sec. 4.2), complete one iteration. After one iteration these g_l^i and f_l^i are known and then, it has been used for obtaining final solution based on equation Eq. (35) and Eq. (37). These two iterative steps can be continued to get the final converged solution depending on the required level of accuracy.

5 Numerical Results and discussion

This section presents numerical results concerning validation of the proposed analytical framework first, followed by in-depth elastic and viscoelastic analyses.

5.1 Elastic analysis

5.1.1 Hybrid piezoelectric rectangular plates of constant stiffness and density

The developed mathematical model is validated first by comparing the present results with previously published results in the literature to establish and demonstrate the accuracy of the proposed analytical solution approach. In the following subsections, the effect of in-plane graded elastic properties on natural frequencies and mode shapes of intelligent FGM plates is investigated extensively. New benchmark results are presented for various gradation cases by considering different configurations and thickness ratios ($S = a/h$) under different electrical and mechanical boundary conditions. The material properties [94] used in this study are tabulated in Table 2.

Table 2: Material constants [83]

Material	Y_1	Y_2	Y_3	G_{23}	G_{13}	G_{12}	ν_{12}	ν_{13}	ν_{23}	ρ
Mat. 1	6.9	6.9	6.9	1.38	1.38	1.38	0.25	0.25	0.25	1578
Mat. 2	224.25	6.9	6.9	1.38	56.58	56.58	0.25	0.25	0.25	1578
Mat. 3	172.5	6.9	6.9	1.38	3.45	3.45	0.25	0.25	0.25	1578
Mat. 4 (Gr/Ep)	181.0	10.3	10.3	2.87	7.17	7.17	0.28	0.28	0.33	1578
Mat. 5 (Face)	131.1	6.9	6.9	2.3322	3.588	3.588	0.32	0.32	0.49	1000
Mat. 6 (Core)	0.0002208	0.0002208	2.76	0.4554	0.5451	0.01656	0.99	3×10^{-5}	3×10^{-5}	70
PZT-5A	61.0	61.0	53.2	21.1	21.1	22.6	0.35	0.38	0.38	7600
Material	d_{31}	d_{32}	d_{33}	d_{24}	d_{15}	η_{11}	η_{22}	η_{33}		
PZT-5A	-171	-171	374	584	584	15.3	15.3	15.0		

Units: density (ρ) in Kg/m^3; Young's moduli Y_i in GPa and shear moduli G_{ij} in GPa; electric permittivities η_{ij} in nF/m; piezoelectric strain coefficients d_{ij} in pm/V; where $d_0 = d_{33}$ pm/V

Various configurations of smart plates, as shown in Fig. 3, are taken into consideration for the current numerical study. The obtained results for natural frequencies are expressed in non-dimensionalized form using $\omega^* = \omega a S\sqrt{\rho_0/Y_0}$. Where Y_0=6.9 GPa for hybrid smart plate (b) and (c), and Y_0=10.3 GPa for all other hybrid smart plates and in-plane functionally graded (IPFG) plates. Similarly, ρ_0= 1000 Kg/m^3 for hybrid smart plate (c), and ρ_0= 1578 Kg/m^3 for all other hybrid smart plates and inplane IPFG plates. Similarly, non-dimensionalized values of modal displacements, electrical state variables and stresses are plotted in graphical figures, and the following expression is used for the non-dimensionalization of results.

$$(\bar{w},\, \bar{v},\, \bar{u}) = (w, v, u)/\max(w, v, u); \qquad (\bar{\sigma}_i,\, \bar{\tau}_{ij}) = (\sigma_i,\, \tau_{ij})\, h\, S/(\, Y_0 \max(w, u))$$

$$\bar{\phi} = \phi\, d_0/\max(w, u) \qquad \bar{D}_i = D_i\, h\, S/(d_0\; Y_0 \max(w, u))$$

$\bar{w}$, $\bar{v}$, $\bar{u}$ denotes the non-dimensionalized displacement in z, y, and x directions. Normalized normal stresses and shear stresses are denoted by $\bar{\sigma}_i$ and $\bar{\tau}_{ij}$, respectively. Similarly, $\bar{\phi}$ expresses non-dimensionalized electric potential, and normalized electric displacements are expressed by $\bar{D}_i$. Here $S(= a/h)$ expresses the span-to-thickness ratio of FGM plate and $\max(w, v, u)$ denotes the largest value of displacement w, v and u along the thickness of FGM plate for that flexural mode. The length of all FGM and composite plates are taken equal to unity ($a = 1$) for all cases and thickness of rectangular plate is assumed according to span to thickness ratio ($S = a/h$) of the plates. For $S = 5, 10, 20$ the values of h are 0.2, 0.1, 0.05, respectively. Similarly, $s(= h/a)$ expresses the thickness-to-span ratio. The rectangular plates are named corresponding to their mechanical support conditions at the ends. For example, CFSS designation of plate indicates that plate is clamped (C) at $\xi_1 = 0$ and free (F) at $\xi_1 = 1$, and simply-supported at $\xi_2 = 0$ and $\xi_2 = 1$.

Here the present EKM-Fourier series technique of solution is validated by comparing the results with previously reported numerical results for constant property cases without any type of gradation. First, the present results are validated for an orthotropic single-layered piezoelectric rectangular plate subjected to a

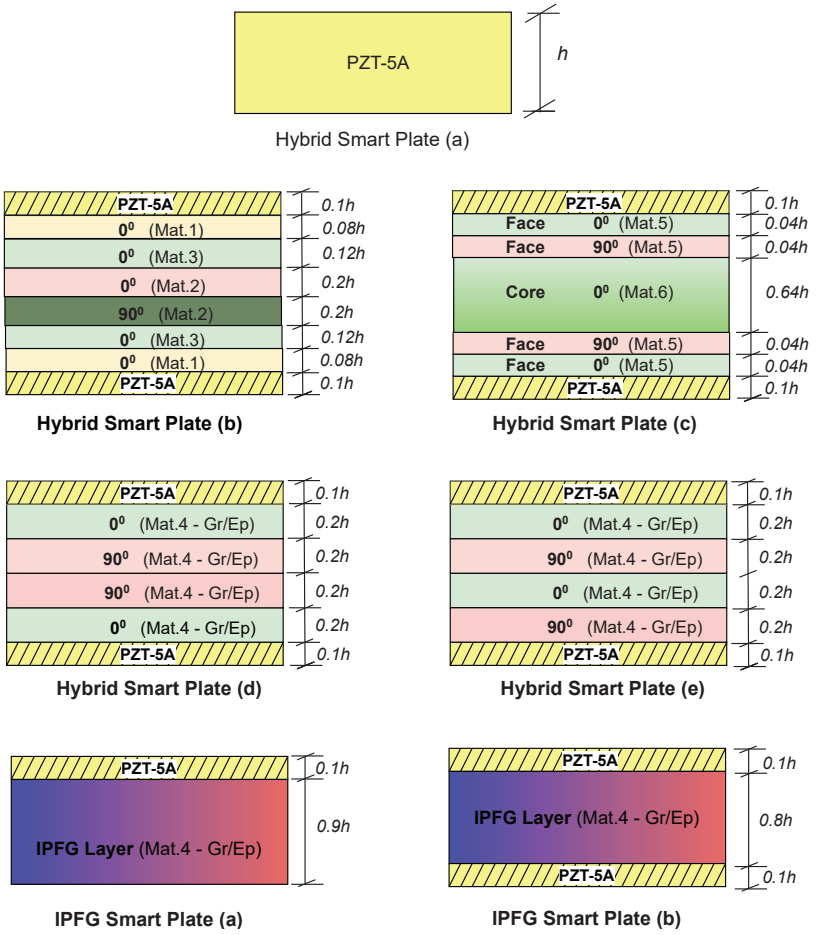

Fig. 3: Configurations of smart IPFG rectangular plates considered for the present numerical study.

simply-supported boundary condition and it has poling [Remark 2: Appendix G (supplementary material)] along the z-direction. Results are compared with the 3D exact result of Heyliger and Saravanos [95], which was obtained by employing the Fourier series approach through which the solution of the ordinary differential equations can be obtained in the exact closed form (therefore, referred as the exact solution approach in literature), and 3D elasticity-based analytical results of Susanata and Kumari [93]. In Table 3, the results are compared for two-type of electrical arrangements, (i) Single-layered PZT-5A plate subjected to closed-circuit (CC) condition at top and bottom surface ($\phi(x, y, \pm h/2)$=0), (ii) Single-layered PZT-5A plate subjected to Open-circuit (OC) condition at top and bottom surface ($D_z(x, y, \pm h/2)$=0). Results are compared for thick plates having thickness ratio S=4 and S=1 (Cubical-plate). It is noted that the current power series-based EKM solution is accurate in predicting natural frequencies of single-layered smart piezoelectric plate, and all results are in good agreement.

After establishing the accuracy of the present mathematical model for single-layered piezoelectric smart plate (a), the results are obtained for laminated piezoelectric plates (b), (c), (d), and (e) of different configurations, as shown in Fig. 3. All the laminated hybrid plates are integrated with two PZT-5A plies at the bottom and top to their elastic substrate. The thickness of both top and bottom piezoelectric layers is $0.1h$ and it has poling along with the thickness (z-direction). The surfaces of piezoelectric layers with the elastic substrate are considered grounded (ϕ=0). The elastic substrate of plate (b) has six laminae with orientation θ_k as $[0^0/0^0/90^0/0^0/0^0/0^0]$ with thickness $0.08h/0.12h/0.2h/\ 0.2h/0.12h/0.08h$ of material 1/3/2/2/3/1, as shown in Fig. 3. The elastic substrate of the plate (c) is a five-layer sandwich substrate with two faces $[0^0/90^0]$ of Material 5 and a soft-core $[0^0]$ of Material 6. Overall orientation of substrate is $[0^0/90^0/0^0/90^0/0^0]$ of thicknesses 0.04h/0.04h/0.64h/0.04h/0.04h and material 5/5/6/5/5, as shown in Fig. 3. The elastic substrate of the plate (d) and (e) has a 4-ply composite laminate of

Table 3: Comparison of first six lowest flexural frequencies for all-around simply supported (SSSS) single-layered square smart piezoelectric plates under closed circuit (CC) condition ($\phi(x, y, \pm h/2)$=0 and open circuit (OC) condition ($D_z(x, y, \pm h/2)$=0).

	Closed circuit			Open circuit		
	Present	3D Analytical [93]	3D Exact [95]	Present	3D Analytical [93]	3D Exact [95]
	96929.9	96929.9	96929.9	98233.0	98231.7	98231.7
	194254.8	194254.8	194255.0	194254.8	194254.8	194255.0
S=4	327662.5	327662.5	327663.0	355170.5	355110.0	355110.0
	538884.4	538884.4	538885.0	538884.4	538884.4	538885.0
	609187.1	609185.3	609186.0	690984.2	690766.8	690767.0
	958929.5	958922.4	958922.0	960118.1	960103.9	960103.0
	713025.6	713062.7	713061.0	724559.2	724602.0	724602.0
	777020.5	777020.5	777021.0	777020.5	777020.5	777021.0
S=1	889887.0	889901.3	889902.0	912882.9	912911.4	912912.0
	925431.5	925431.5	925431.0	925431.5	925431.5	925431.0
	1243806.5	1243817.9	1243819.0	1270594.7	1270594.7	1270594.0
	1270594.7	1270594.7	1270594.0	1293476.5	1293505.0	1293504.0

Table 4: Comparison of natural frequencies ($\omega^* = \omega a S\sqrt{\rho_0/Y_0}$) of hybrid smart plate (b), intelligent sandwich plate (c), composite smart plate (d) and (e) with different S values and electrical condition as $\phi(x, y, -h/2)$=0 and $D_z(x, y, h/2)$=0.

		Smart Plate (b)		Smart Plate (c)		Smart Plate (d)		Smart Plate (e)	
	S	Present	3D Exact[94]	Present	3D Exact[94]	Present	3D Exact[94]	Present	3D Exact[94]
	5	7.4148	7.4148	4.5233	4.5277	7.1810	7.1810	7.1809	7.1809
ω^*_{11}	10	10.0342	10.0342	7.3390	7.3390	9.3686	9.3686	9.2795	9.2795
	20	11.4178	11.4178	9.7440	9.7440	10.4327	10.4327	10.2231	10.2231
	5	14.7140	14.7140	7.8958	7.8958	13.5944	13.5944	13.6391	13.6391
ω^*_{21}	10	22.3965	22.3965	13.8801	13.8801	21.2357	21.2357	20.4789	20.4779
	20	29.0240	29.0240	21.3567	21.3567	27.8333	27.8333	25.2664	25.2664
	5	23.6208	23.6208	11.9501	11.9501	20.9313	20.9313	21.0482	21.0482
ω^*_{31}	10	37.7411	37.7411	21.2309	21.2357	35.0186	35.0186	34.5431	34.5431
	20	53.5800	53.5800	35.6934	35.6934	51.6591	51.6591	47.5942	47.5942
	5	18.6431	18.6431	10.2915	10.2915	18.3672	18.3672	18.2319	18.2319
ω^*_{22}	10	29.6593	29.6593	18.0932	18.0103	28.7240	28.7240	28.7234	28.7234
	20	40.1367	40.1367	29.3559	29.3559	37.4744	37.4744	37.1180	37.1180
	5	30.7853	30.7853	16.9820	16.9820	29.7901	29.7901	29.4727	29.4727
ω^*_{33}	10	51.5468	51.5468	29.2571	29.2571	50.7313	50.7313	50.5764	50.5764
	20	77.4823	77.4823	50.7073	50.7073	73.8647	73.8647	73.6951	73.6951

graphite-epoxy Mat.4, and each ply is of equal thickness $0.2h$. Plate (d) has symmetric substrate with lay-up $[0^0/90^0/90^0/0^0]$ and the of plate (e) has antisymmetric substrate with lay-up $[90^0/0^0/90^0/0^0]$, as shown in Fig. 3. The all above mentioned stacking sequences are from the base layer to top layer for all plates, as shown in Fig. 3. The dimensionless flexural frequencies are tabulated in Table 4 for plates (b), (c), (d) and (e) with the upper surface grounded ($\phi(x, y, h/2)$=0) and the bottommost surface subjected to open-circuit conditions ($D_z(x, y, \pm - h/2)$=0. The flexural frequencies are listed for different span to thickness ratio, S=5,10, 20, and for different mode, (m, n) = (1, 1), (2, 1), (2, 2), (3, 1), (3, 3). The present numerical results for hybrid smart plates (b), (c), (d) and (e) are compared with the 3D exact results presented by Kapuria and Achary [94], which is also based on the Fourier series approach, known as an exact solution. It is noted that the current power-series EKM model is very much accurate in predicting flexural frequencies for symmetric and antisymmetric laminated/sandwich piezoelectric smart plates. All numerical results are in excellent agreement with the 3D exact results of [94]. The current

model is highly efficient and accurate, and moreover, accuracy is not affected much by thickness to span ratio S and inhomogeneity in configurations.

After demonstrating the validation for simply-supported smart piezoelectric plates, the validation is carried out for piezo-laminated smart rectangular plates subjected to arbitrary support conditions. The numerical results obtained from the present power series-based EKM model are compared with the result presented by Susanta and Kumari [93] which are obtained using 3D exact EKM. Table S1 (in the supplementary material) shows the comparison of the first ten lowest natural bending frequencies for thick (S=5) and moderately thick (S=10) hybrid smart plates (d) under different mechanical support conditions such as SSSS, CSSS, CCSS, CFSS, and FFSS. Excellent agreement is observed for all the cases. It demonstrates that the present power-series approach is efficient, yet accurate in solving coupled system of ODEs for dynamic cases. It is worth noting that one term ($n = 1$) based EKM solution is enough to predict the natural frequencies of the piezoelectric plate accurately. It is also worth mentioning that the present power series-based EKM solution is equally accurate for predicting the natural frequencies of the thick and thin hybrid piezoelectric plates subjected to open or closed-circuit conditions. The effects of electrical circuit conditions are very less on flexural frequencies of the plate due to weak electro-mechanical coupling, but these tiny effects play a vital role in precise control and sensory applications. It is observed that the present mathematical model is very accurate and precise in predicting these small effects, as illustrated in table 3, 4 and S1 (Supplementary material).

5.1.2 Hybrid piezoelectric rectangular plates with variable stiffness and density

After demonstrating the accuracy and efficacy of the current 3D mathematical model for constant stiffness piezoelectric plates, the numerical study is extended to the analysis of functionally graded smart piezo-plates in this section. Two types of smart FGM plates are taken into consideration for the numerical study, (i) IPFG Plate (a): In-plane functionally graded rectangular substrate integrated with a single piezoelectric layer at the top; and (ii) IPFG Plate (b): In-plane functionally graded rectangular substrate integrated with the piezoelectric layer at bottom and top, as shown in Fig. 3. The thickness of PZT-5A layers is $0.1h$ for both type of IPFG plates. To study the effect of in-plane stiffness variation on dynamic behaviour of smart plates, three types of stiffness and density gradation cases are considered for the elastic layers, Case (1): $\delta_1 = \delta_2 = \delta_p = 0.5$; Case (2): $\delta_1 = \delta_2 = \delta_p = 1.0$; and Case (3): $\delta_1 = 2.0$, $\delta_2 = 1.0$, $\delta_p = 1.5$ along with homogenous plate (constant properties) case (Constant: $\delta_1 = \delta_2 = \delta_p = 0.0$). The numerical results for homogenous (constant) property case are also presented along with graded density and stiffness cases to access the influence of in-plane variation of stiffness and density on the flexural frequencies and electro-mechanical behavior of IPFG plates. Only converged results are tabulated here, which are obtained by taking $n = 1$, iter.1 for SSSS smart plate and $n = 1$, iter.2 for all other types of support conditions. The convergence study of the present EKM approach is presented in Table S2 (supplementary material). In subsequent sections, three-dimensional finite element (3D FE) results, obtained using commercial finite element analysis (FEA) software ABAQUS, are also listed along with present EKM results for validation purposes because no other analytical and semi-analytical solution exists in literature for free-vibration of variable-stiffness piezoelectric plates. For 3D FE analysis, user material subroutine (UMAT) is developed to implement the in-plane gradation of stiffness and density in the finite element model and then converged FE results are obtained by using a discretization of 50 (length) $\times$50 (width) $\times$18 (thickness). For comparison and bench-marking purposes, the numerical results are tabulated for various type of electrical and mechanical supports under different thickness ratios.

5.1.2.1 IPFG Plate (a): In-plane functionally graded rectangular elastic substrate integrated with piezoelectric layer at top. An in-plane functionally graded plate (a) integrated with a smart piezoelectric (PZT-5A) layer of thickness $0.1h$ at the top, as shown in Fig. 3, is taken into consideration for numerical study in this section. The stiffness and density of the elastic composite layer are assumed to vary linearly along the axial (x) direction where the elastic and electrical properties of the piezoelectric layer are assumed constant. The side edges and top/bottom surface of the active piezoelectric

Table 5: Influence of in-plane gradation of density and stiffness on natural flexural frequencies ($\omega^* = \omega a S\sqrt{\rho_0/E_0}$) of moderately thick ($S = 10$) IPFG smart piezoelectric plate (a) subjected to CCSS boundary conditions.

	Constant		Case (1)		Case (2)		Case (3)	
ω^*_{nm}	Present	3D FE	Present	3D FE	Present	3D FE	Present	3D FE
ω^*_{11}	15.390	15.489	12.978	13.099	10.422	11.403	10.095	10.350
ω^*_{21}	32.424	32.719	27.264	27.542	23.591	23.878	21.609	21.893
ω^*_{31}	52.017	52.585	43.763	44.260	37.874	38.348	34.936	35.382
ω^*_{41}	72.422	73.239	61.041	61.726	52.846	53.473	49.052	49.639
ω^*_{51}	93.019	94.057	78.703	79.483	68.166	68.903	63.588	64.264
ω^*_{12}	20.029	20.023	17.665	17.506	15.970	15.662	14.164	14.509
ω^*_{22}	35.752	36.000	30.489	30.724	26.716	26.962	24.711	24.960
ω^*_{32}	54.645	55.158	46.296	46.747	39.490	40.746	37.382	37.790
ω^*_{42}	74.610	75.381	63.149	63.795	54.871	55.465	51.079	51.638
ω^*_{52}	95.377	95.847	80.406	81.241	69.845	70.600	65.259	65.964
ω^*_{13}	29.065	29.224	26.133	26.275	23.841	23.977	22.276	22.407
ω^*_{23}	42.431	42.632	37.002	37.192	33.040	33.245	30.848	31.059
ω^*_{33}	59.759	60.187	51.322	51.697	45.232	45.596	42.201	42.549
ω^*_{43}	78.119	79.416	67.225	67.796	58.623	59.397	55.013	55.509
ω^*_{53}	98.246	99.174	83.813	84.573	73.198	73.890	68.556	69.203

Table 6: Effect of in-plane gradation (density and stiffness) on natural flexural frequencies ($\omega^* = \omega a S\sqrt{\rho_0/E_0}$) of moderately thick ($S = 10$) IPFG piezoelectric plate (a) for CFSS boundary condition.

	Constant		Case (1)		Case (2)		Case (3)	
ω^*_{nm}	Present	3D FE	Present	3D FE	Present	3D FE	Present	3D FE
ω^*_{11}	5.199	5.226	4.489	4.507	3.984	3.996	3.628	3.636
ω^*_{21}	17.306	17.377	14.866	14.923	13.066	13.123	11.704	11.771
ω^*_{31}	36.543	36.966	31.267	31.051	27.376	27.375	24.764	24.805
ω^*_{41}	57.271	57.494	48.841	48.985	42.615	42.763	39.103	39.256
ω^*_{51}	78.411	79.372	66.622	67.341	58.109	58.554	53.830	54.201
ω^*_{12}	12.914	13.029	11.399	11.515	10.301	10.403	9.511	9.597
ω^*_{22}	22.869	22.936	20.014	20.070	17.911	17.963	16.487	16.547
ω^*_{32}	40.273	40.530	34.747	34.910	30.670	30.801	28.111	28.243
ω^*_{42}	60.118	60.462	51.512	51.754	45.147	45.352	41.665	41.872
ω^*_{52}	80.222	80.476	68.800	69.392	60.139	60.617	55.880	56.282
ω^*_{13}	24.382	24.537	21.685	21.830	19.712	19.790	18.148	18.263
ω^*_{23}	32.236	32.333	28.777	28.860	26.182	26.256	24.423	24.500
ω^*_{33}	47.100	47.317	41.240	41.383	36.893	37.008	34.248	34.362
ω^*_{43}	65.348	65.809	56.543	56.813	50.004	50.202	46.476	46.658
ω^*_{53}	84.524	85.722	72.866	73.438	64.089	64.454	59.784	60.086

layer are considered under close-circuit conditions. First five lowest dimensionless fundamental flexural frequencies ($\omega^* = \omega a S\sqrt{\rho_0/E_0}$, here E_0=10.3 GPa, ρ=1578 kg/m^3) are tabulated for m = 1, 2 and 3 considering moderately thick (S = 10) hybrid plate (a) under different mechanical support conditions. Results are listed for three gradation cases, *i.e.* Case(1), Case(2), and Case(3), along with homogeneous plate (constant properties case) to investigate the influence of in-plane variation of stiffness and density gradation on flexural frequencies. Tables 5 and 6 contain benchmark results for CCSS and CFSS support conditions, respectively. Subsequently, the results are for SSSS, CSSS, SFSS, and FFSS support conditions are tabulated in Table S3, S4, S5 and S6 (refer to the supplementary material), respectively. The fundamental flexural frequencies for the in-plane graded hybrid plate are presented for the first time in this paper. As the gradation index for elastic properties and density increases, the natural frequencies decrease remarkably under all the support conditions. The quantitative effect of in-plane variation of density and stiffness on flexural frequencies of hybrid rectangular plate primarily depends on the mechanical support conditions of the IPFG plate. Percentage decrement in flexural frequencies due to the in-plane varition of properties are plotted in Fig. S1, Fig. S2 and Fig. S3 of the supplementary material. An interesting observation is that the extent of the effect of gradation on lower natural frequencies for m=1, 2, and 3 significantly depends upon the type of support conditions. On the other hand, the influence of gradation on higher mode natural flexural frequencies (for m=1, 2, and 3) shows independence from mechanical support conditions. The percentage change in higher mode natural flexural frequencies is nearly the same for all support conditions. This observation is physically relevant considering the fact that higher flexural vibration modes are more local in nature. For all hybrid plated, except FFSS plate, nearly 10 to 15% decrement is noted in the lowest five flexural frequencies (m=1,2, and 3) for Case (1) compared to the constant property case. For Case (2) and Case (3), the percentage decrease in flexural frequencies are 16 to 27% and 22 to 34% for Case (3), respectively. For the FFSS hybrid plate, these decrements are 7-14 % for Case (1), 12-26 % for Case (2), and 15-33 % for Case (2). All results reported in this section have been computed by taking n = 1, iteration 1 for SSSS support conditions and n = 1, iteration 2 for other support conditions.

After studying the influence of in-plane gradation of stiffness and density on the natural flexural frequencies of the hybrid smart plate, the numerical investigation is extended to access the impact of in-plane gradation on mode shapes of the hybrid plate. The flexural 3D mode shapes associated with the lowest five natural frequencies are plotted for different types of support conditions under constant properties case and gradation Case 1. The 3D mode shapes for the SSSS hybrid IPFG plate are displayed for constant property case and gradation Case 1 in Fig. S4 and S5, respectively. Similarly, the 3D mode shapes for the CSSS hybrid IPFG plate are displayed for homogenous case (constant property case) and gradation Case 1 in Fig. S6 and Fig. S7. Fig. S8 and Fig. S9 contain 3D mode shapes for the CCSS hybrid IPFG plate for constant property case and gradation case 1, respectively. Similarly, the 3D mode shapes for other boundary conditions are also plotted to investigate the influence of gradation in detail. In figure Fig. S10 and Fig. S11 results are plotted for CFSS plates. Mode shapes of SFSS and FFSS hybrid plates are given in Fig. S12, Fig. S13, Fig. S14 and Fig. S15 for constant property case and gradation Case (1). The figures S6-S15 are given in supplementary material. It is worth mentioning that all flexural mode shapes are impacted significantly by the in-plane gradation of stiffness and density. Another interesting observation is that the mode shape of the FFSS plate is affected more as compared to other support conditions.

Further, the influence of axial gradation of stiffness and density is also investigated on the longitudinal variation of flexural deflection ($\bar{w}$, $\bar{v}$, $\bar{u}$) and stresses ($\bar{\sigma}_x$, $\bar{\sigma}_y$, $\bar{\tau}_{xy}$, $\bar{\tau}_{yz}$, $\bar{\tau}_{xz}$) in the hybrid FGM plate. In Fig. 4 and 5 longitudinal variation of stresses and displacements are plotted for the first flexural vibration mode of moderately thick (S = 10) smart hybrid plate (a) subjected to SSSS and CFSS support conditions, respectively. Subsequently, the longitudinal variation of stresses and displacements are also plotted for CSSS, CCSS, and SFSS hybrid FGM plate in Fig. S16, S17, and S18 (supplementary material), respectively. In these figures, the results are plotted for all gradation cases along with the constant property case. It is found that the longitudinal variation of stresses in smart FGM plates is impacted significantly due

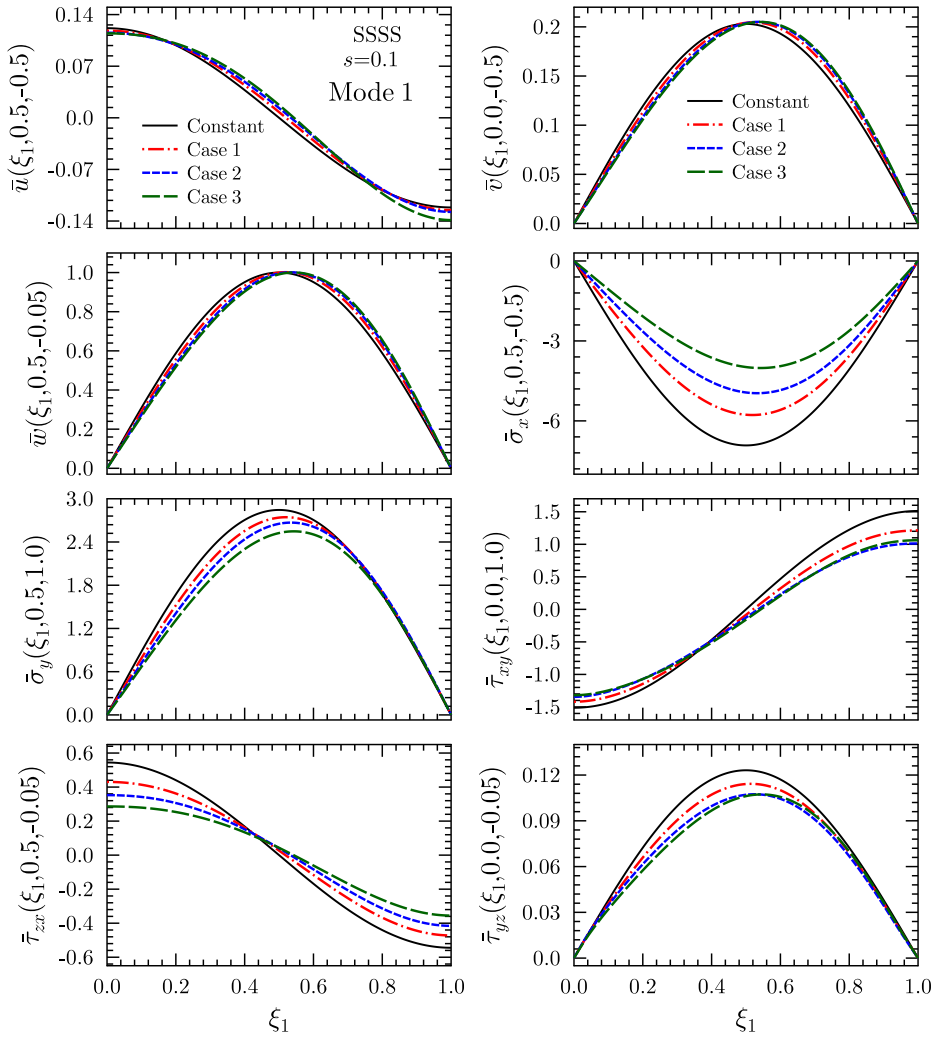

Fig. 4: Influence of in-plane variation of density and stiffness on axial variations of displacements and stresses for first flexural vibration mode (Mode-1) of the moderately thick ($S = 10$) IPFG smart plate (a) subjected to SSSS boundary condition.

to in-plane gradation, whereas displacement of the IPFG plates is least affected. The effect on stresses $\bar{\sigma}_x$, $\bar{\tau}_{xy}$, and $\bar{\tau}_{xz}$ are more as compared to other stresses. It is worth mentioning that the extent of the effect of gradation on displacement and stresses majorally depends on mechanical support conditions of the hybrid plate. An interesting observation is that the intelligent IPFG plate is more sensitive to the in-plane variation of density and elastic properties when subject to free edge boundary conditions such as CFSS and SFSS plates. The relative influence of gradation is most when the IPFG plates are subjected to the free-free boundary conditions. The effect is least when the hybrid piezoelectric plate is subjected to clamped boundary conditions. It reveals that the natural flexural vibration behavior of the plate under in-plane gradation mainly depends upon the mechanical end conditions of the plate.

Further, to access the effect of in-plane gradation of stiffness and density on sensory behavior of piezoelectric layers, the longitudinal variation of the electric variable ($\bar{D}_x$, $\bar{D}_y$, $\bar{D}_z$ and ϕ) are plotted for SSSS and CFSS hybrid smart plate in Fig. 6 and 7, respectively. Similarly results are also plotted for CSSS and SFSS hybrid smart plate in Fig. S19 and S20, respectively (supplementary material). It is found that the variation of electrical variables in the piezoelectric sensor layer is not affected much by longitudinal gradation of material properties in the elastic composite layers. A small effect of in-plane variation of density and stiffness is observed on electric field $\bar{D}_z$ and electric potential (ϕ) under SSSS and CSSS support conditions. It is worth noting that the natural flexural frequencies and their corresponding mode shapes are affected remarkably by the axial gradation of properties in the elastic layer, whereas the response of the

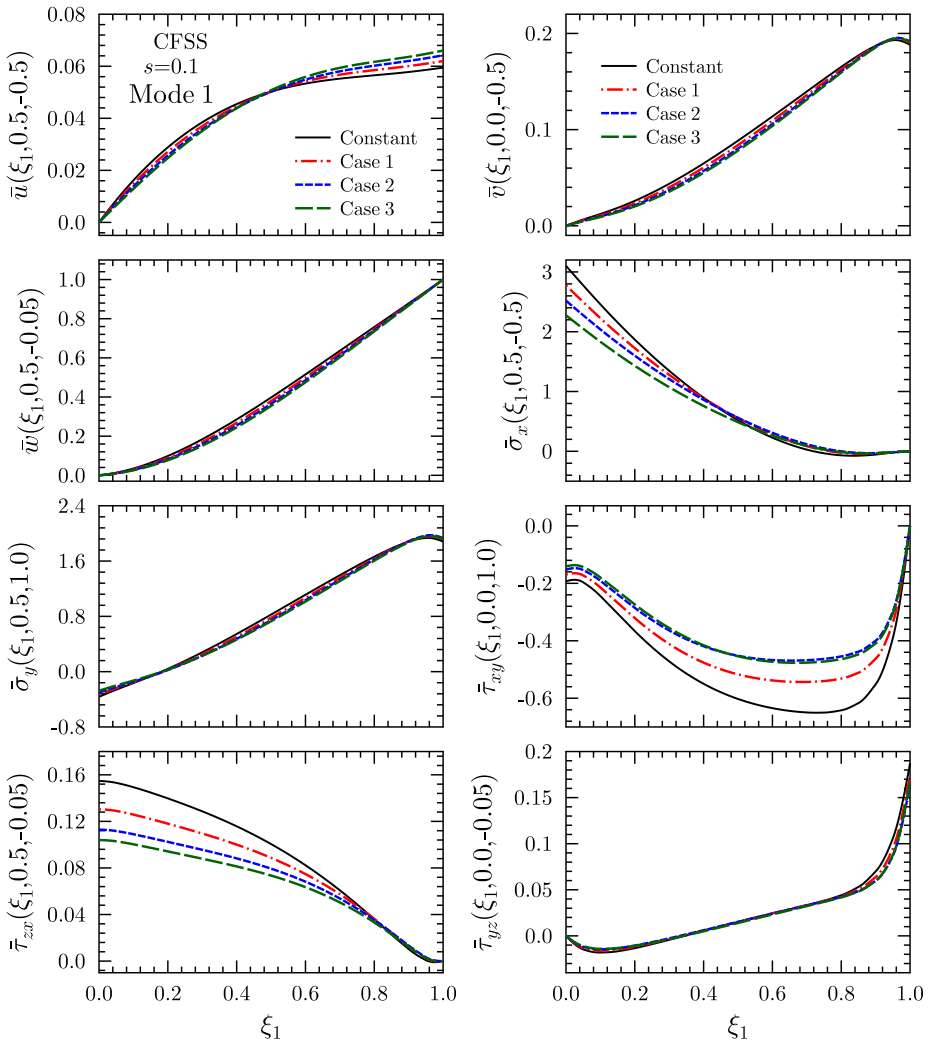

Fig. 5: Influence of in-plane variation of density and stiffness on axial variations of displacements and stresses for first flexural vibration mode (Mode-1) of the moderately thick ($S = 10$) IPFG smart plate (a) subjected to CFSS boundary condition.

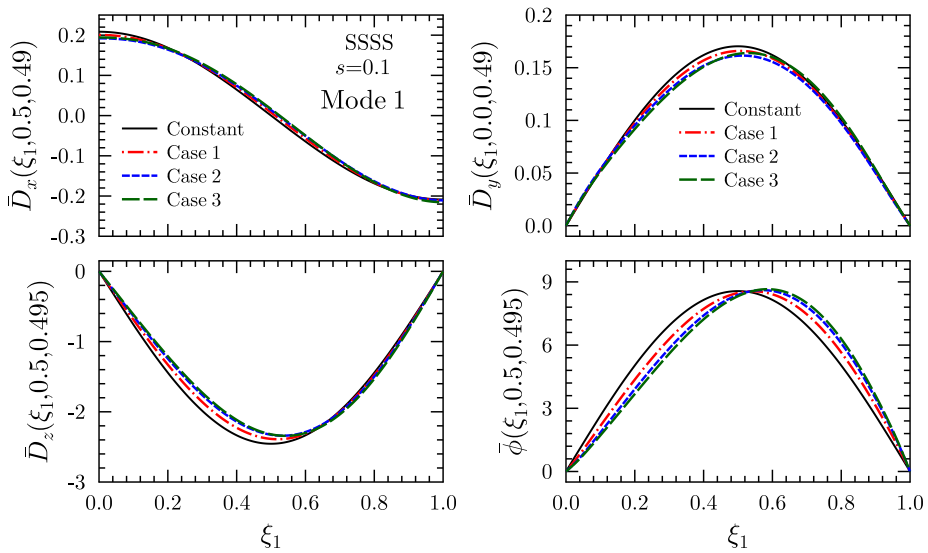

Fig. 6: Influence of in-plane variation of density and stiffness on axial variations of electric variables for first flexural vibration mode (Mode-1) of the moderately thick ($S = 10$) IPFG smart plate (a) subjected to SSSS boundary condition.

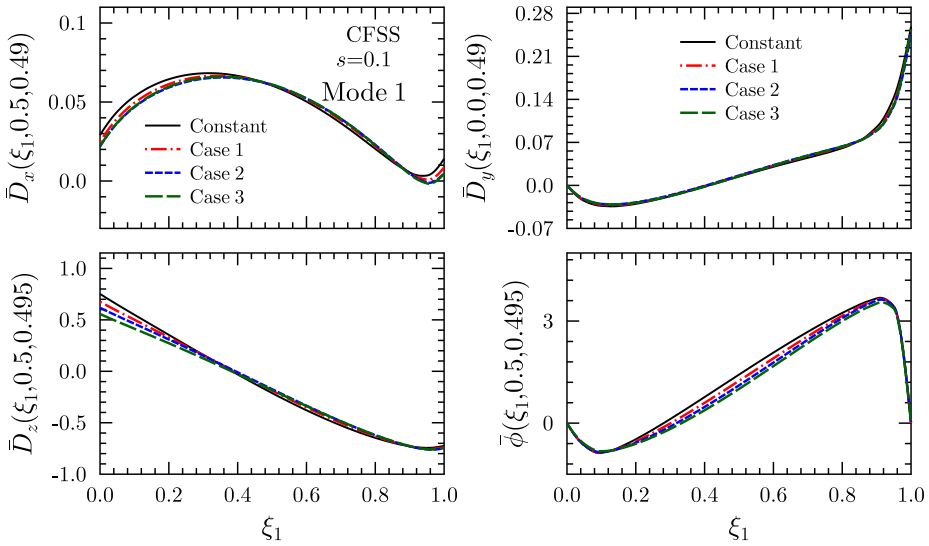

Fig. 7: Influence of in-plane variation of density and stiffness on axial variations of electric variables for first flexural vibration mode (Mode-1) of the moderately thick ($S = 10$) IPFG smart plate (a) with CFSS boundary condition.

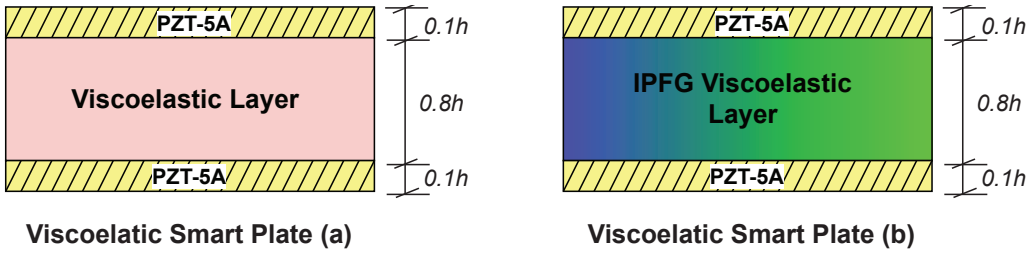

Fig. 8: Geometry of the smart in-plane functionally graded (IPFG) viscoelastic plates.

sensory layer remains almost identical or affected by a very small amount. This interesting observation of the present study can play a significant role in the design of piezoelectric sensors and actuators for vibration control applications.

5.1.2.2 IPFG Plate (b): In-plane functionally graded rectangular elastic substrate integrated with two piezoelectric layers at top and bottom. In this section, the longitudinal graded rectangular plate (b) which is integrated with the piezoelectric layers (PZT-5A) at the bottom and top, as shown in Fig. 3, is investigated. The stiffness and density of the composite elastic layer are considered to vary continuously and linearly along the x-direction, whereas the material properties of the PZT layers are assumed constant. The side edges of the smart PZT-5A layers are grounded ($\phi(y,z)$=0 at $x = 0, a$). In Table 7 lowest ten natural flexural frequencies ($\omega^* = \omega h\sqrt{\rho_0/E_0}$, where ρ=1578 kg/m^3 , E_0=10.3 GPa) are presented for moderately thick ($S = 10$) hybrid IPFG plate (b) subjected to various mechanical edge conditions such as SSSS, CSSS, CCSS, CFSS, SFSS and FFSS. Subsequently, the results for thick ($S = 5$) hybrid IPFG plate (b) are tabulated in Table S7 (refer to the supplementary material), respectively. The benchmark numerical results are tabulated for three gradation cases (Case 1, Case 2, Case 3) along with the homogeneous (constant property) case. Significant effect of in-plane variation of density and stiffness is noted on the natural flexural frequencies of IPFG plates. The natural flexural frequencies show significant decrement as the gradation index increases. The extent of the gradation influence mainly relies on mechanical edge conditions of the hybrid IPFG plate.

Further, to assess the effect of in-plane gradation of stiffness and density on sensory behavior of piezoelectric layers, the longitudinal variation of the electric variable ($\bar{D}_x$, $\bar{D}_y$, $\bar{D}_z$ and ϕ) are plotted for SSSS, CSSS and SFSS hybrid smart IPFG plate (b) in Fig. S21, S22 and S23, respectively (supplementary material). It is

Table 7: Influence of in-plane gradation of density and stiffness on lowest ten natural flexural frequencies ($\omega^* = \omega a S\sqrt{\rho_0/E_0}$) of moderately thick ($S$=10, $t_p = 0.1h$) IPFG smart plate (b) subjected to open–circuit conditions at top and closed-circuit bottom surface.

		1	2	3	4	5	6	7	8	9	10
		ω^*_{11}	ω^*_{12}	ω^*_{21}	ω^*_{13}	ω^*_{22}	ω^*_{23}	ω^*_{14}	ω^*_{31}	ω^*_{32}	ω^*_{24}
SSSS	Constant	9.673	18.145	24.673	29.816	30.493	39.573	42.621	42.815	47.909	50.502
	Case 1	8.715	16.869	21.633	27.971	27.381	36.243	40.093	37.233	41.514	46.816
	Case 2	7.951	15.791	19.322	26.353	24.968	33.602	37.797	33.030	37.283	43.834
	Case 3	7.288	14.935	17.706	25.051	23.410	31.896	35.909	30.727	35.045	41.824
		ω^*_{11}	ω^*_{12}	ω^*_{21}	ω^*_{13}	ω^*_{22}	ω^*_{23}	ω^*_{14}	ω^*_{31}	ω^*_{32}	ω^*_{24}
CSSS	Constant	11.613	19.029	26.603	30.229	31.850	40.448	42.845	44.059	48.109	51.073
	Case 1	10.392	17.564	23.430	28.250	28.593	36.983	40.214	38.526	42.550	47.266
	Case 2	9.419	16.345	20.983	26.542	26.041	34.213	37.861	34.321	38.292	44.171
	Case 3	8.649	15.423	19.358	25.201	24.441	32.456	35.952	32.054	36.055	42.108
		ω^*_{11}	ω^*_{12}	ω^*_{21}	ω^*_{13}	ω^*_{22}	ω^*_{23}	ω^*_{14}	ω^*_{31}	ω^*_{32}	ω^*_{24}
CCSS	Constant	13.747	20.063	28.338	30.229	33.152	40.448	43.094	45.232	49.083	51.655
	Case 1	12.083	18.350	24.608	28.250	29.419	36.983	40.417	39.218	43.092	47.584
	Case 2	10.809	16.958	21.840	26.542	26.599	34.213	38.019	34.777	38.626	44.347
	Case 3	9.999	16.040	20.341	25.201	25.068	32.456	36.128	32.613	36.464	42.301
		ω^*_{11}	ω^*_{12}	ω^*_{21}	ω^*_{22}	ω^*_{13}	ω^*_{31}	ω^*_{23}	ω^*_{32}	ω^*_{13}	ω^*_{33}
CFSS	Constant	5.369	14.536	15.533	22.666	26.832	31.731	33.179	36.870	40.118	45.047
	Case 1	4.873	13.340	13.948	20.792	24.677	28.186	30.840	33.213	36.904	41.151
	Case 2	4.480	12.380	12.682	19.265	22.922	25.408	28.904	30.310	34.257	38.014
	Case 3	4.194	11.631	11.665	18.149	21.514	23.499	27.461	28.456	32.122	36.050
		ω^*_{11}	ω^*_{21}	ω^*_{12}	ω^*_{22}	ω^*_{13}	ω^*_{31}	ω^*_{23}	ω^*_{32}	ω^*_{14}	ω^*_{33}
SFSS	Constant	4.684	13.549	14.353	21.532	26.762	29.949	32.558	35.615	40.083	44.207
	Case 1	4.294	12.181	13.212	19.841	24.642	26.467	30.361	32.033	36.894	40.386
	Case 2	3.982	11.098	12.287	18.463	22.904	23.779	28.542	29.223	34.253	37.341
	Case 3	3.749	10.168	11.552	17.417	21.502	21.882	27.152	27.405	32.120	35.420
		ω^*_{11}	ω^*_{21}	ω^*_{12}	ω^*_{22}	ω^*_{31}	ω^*_{32}	ω^*_{13}	ω^*_{23}	ω^*_{41}	ω^*_{33}
FFSS	Constant	3.866	6.377	13.568	16.031	18.075	25.773	26.102	28.103	35.343	36.248
	Case 1	3.657	5.991	12.795	15.180	16.182	23.643	24.464	26.820	31.090	33.683
	Case 2	3.471	5.680	12.049	14.553	14.739	21.956	22.841	25.931	27.863	31.630
	Case 3	3.310	5.480	11.389	14.111	13.541	20.763	21.468	25.187	25.850	30.253

found that the variation of electrical fields ($\bar{D}_x$, $\bar{D}_y$, $\bar{D}_z$) and potential (ϕ) in the piezoelectric sensor layer is not affected much by longitudinal gradation of material properties in the elastic composite layers. It is worth noting that the natural flexural frequencies are affected remarkably by such axial gradation, whereas the electrical response of the piezoelectric layers remains almost unaffected irrespective of configuration. This would have favorable design implications concerning sensor placements for vibration control and health monitoring applications.

To study the effect of electrical edge conditions on the behaviour of the hybrid plate with in-plane gradation, thick ($S = 5$) hybrid plate (b) is investigated in Table S7 (supplementary material) for closed-closed circuit condition ($\phi(x, y, \pm h/2)$=0), and closed-open circuit condition (($\phi(x, y, -h/2)$=0 and $D_z(x, y, h/2)$=0). The lowest six dimensionless natural flexural frequencies are listed in Table S5 for smart IPFG plate (b) under open-circuit condition at the topmost surface and closed-circuit condition at the bottommost surface. The benchmarks numerical results are listed for different types of hybrid plate boundary conditions such as SSSS, CSSS, CCSS, CFSS, SFSS, and FFSS. It is noticed that the influence of gradation on natural flexural frequencies is unchanged by the type of electric circuit conditions at the bottom and top surface of the plate. Under both types of electrical arrangements, the hybrid plate shows a similar

decrement in flexural frequencies due to the in-plane variation. However, the natural frequencies of hybrid FGM plate under open-circuit conditions are slightly higher than plate subjected to closed-closed circuit conditions. It shows that the effect of electrical circuit condition is very week for the FGM hybrid plates. It is observed that the present power series-based EKM methodology can accurately determine these small effects for smart hybrid IPFG plates, which is important for precise control applications. Moreover, It is worth mentioning that these numerical results can act as benchmark to develop accurate numerical solutions for natural frequency based applications of hybrid IPFG plates. Note that the results for mode shapes, displacements, stress and strain components for various vibration modes can be readily obtained using the proposed framework, as presented in the preceding sub-section.

5.2 Viscoelastic analysis of smart hybrid IPFG plates

After performing the extensive elastic analysis, the present EKM based mathematical model has been extended for viscoelactic analysis of in-plane functionally graded (IPFG) smart viscoelastic plates. The effect of viscoelasticity on the dynamic behaviours of rectangular IPFG plate is studied in detail. For that two types of configurations are considered as shown in Fig. 8.

In the viscoelastic analysis, the modulus amplitudes indicate the strength of the frequency (ω_s) domain signal, whereas the phase angle (ϕ_s) of the signal shows the alignment of frequency components in time. The variation of viscoelastic moduli amplitude and phase angle (ϕ_s) with respect to frequency are plotted in Fig. S24 (supplementary material). The variation is plotted by considering viscoelastic parameters as $\mu = (\omega_s)_{max}/1.4$ and ϵ=0.2 for obtaining the numerical results. The amplitude of elastic and shear moduli increases as the frequency (ω_s) increases until its limiting values as defined in Appendix B (supplementary material). The value of all three elastic and shear moduli at very low frequency (i.e., $\omega_s \to 0$) are equal to the classical elastic and shear moduli of elastic case. A similar trend of viscoelastic material properties is also observed for irregular honeycombs in frequency domain by Mukhopadhyay et al. [75] and for strand-based composite materials in the time domain by Malekmohammadi et al. [96]. The variation of phase angle (ϕ_s) corresponding to all three elastic and shear moduli in frequency (ω_s) domain is also plotted in Fig. S18 (Supplementary material). The phase angle achieves the peak value for a certain critical frequency, which can be calculated easily using Eq. (29). This variation of phase angle (ϕ_s) is explained by the Biot model which is similar to the linear standard viscoelastic model given in Fig. 2. In the Biot model, material behavior is pure elastic at very low and very high frequencies, and the viscous effect is maximum at certain critical frequencies (ω_s). The phase angles (ϕ_s) variation corresponding to Young's moduli and shear moduli are same for all cases, unlike the amplitude of elastic and shear moduli. It is worth noting that the phase angles are not dependent on the material's elastic properties and their values corresponding to different Young's moduli and shear modulus remain unchanged, unlike amplitude of elastic and shear moduli.

After obtaining the variation of amplitude and phase angle of elastic and shear moduli in frequency (ω_s) domain, it has been transformed to the time domain (t) using discrete inverse Fourier series transformation (IFFT) technique, as explained in Sec. 3.3.1. Figure S25 (supplementary material) shows the variation of elastic and shear moduli in the time domain. All three elastic and shear moduli values at $t \to 0$ are almost equal to classical elastic and shear moduli without viscoelasticity effect. As time increases, the value of elastic and shear moduli relaxes and becomes constant after a certain time. A similar trend of elastic and shear moduli in the time-domain has also been reported by Endo and Pereira [97] for an orthotropic viscoelastic material. Furthermore, they also validated their Prony series computational model with experimental data obtained by the creep Test of material. A similar trend of time-dependent Young's modulus for isotropic material has also been observed by Jalocha [98] using a generalized Maxwell model.

In the next stage, the time-dependent variation of Young's moduli and shear moduli is utilized to obtain the time-dependent natural flexural frequency response of viscoelastic smart plates (a) and (b), as shown in Fig. 8. It is considered that the bottom surface of the IPFG viscoelastic smart plate is subjected

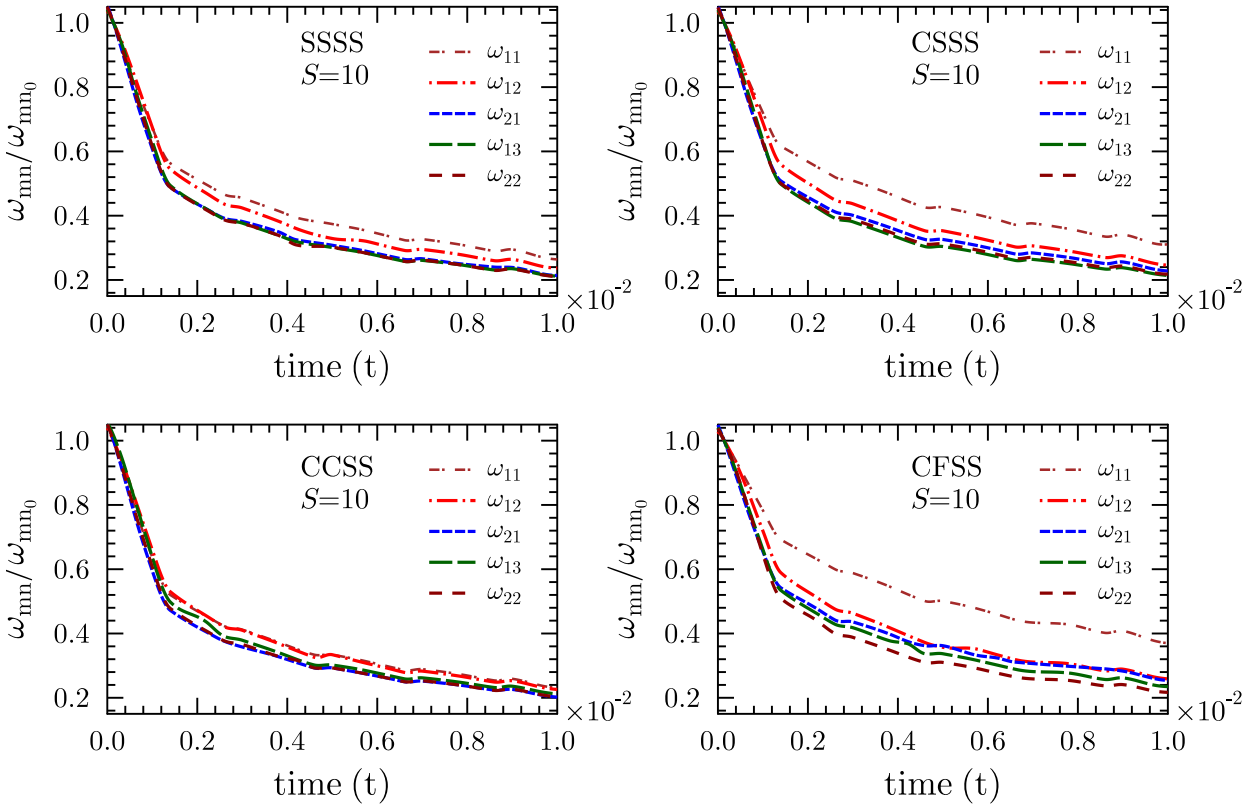

Fig. 9: Effect of viscoelasticity on the first five lowest natural frequencies of three-layered moderately thick (S=10) viscoelastic smart plate (a) without graded properties. The time-dependent variation of first five lowest natural frequencies is plotted in non-dimensionalized form for different boundary conditions such as SSSS, CSSS, CCSS, CFSS. The non-dimensionalization is performed by dividing the natural frequencies of viscoelastic plate by the corresponding natural frequency of elastic plate given in Table 7.

to closed-circuit condition *i.e.* $\phi(x, y, -h/2)$=0, and the top surface is under open circuit condition *i.e.* $D_z(x, y, h/2)$=0. First, the effect of viscoelasticity on natural frequencies is studied for smart viscous plate (a) (plate without in-plane gradation) subjected to different mechanical boundary conditions. Figure 9 shows the influence of viscoelasticity on the first five lowest natural frequencies of three-layered moderately thick (S = 10) viscoelastic smart plate (a) without graded properties.

The time-dependent variation of the first five lowest natural frequencies is plotted in non-dimensionalized form for different boundary conditions such as SSSS, CSSS, CCSS, CFSS. The non-dimensionalization is performed by dividing the flexural frequencies of the viscoelastic plate by the corresponding flexural frequency of elastic plate given in Table 7. It is observed that the viscoelastic layer acts as a damper. Due to viscoelastic behavior of the composite layer, the natural frequencies of the smart hybrid plate are decreased with increasing time. It is worth noting that the natural frequencies decrease gradually with time, unlike viscoelastic properties, which decrease fast with the increase in time. The viscoelastic effect on lower vibration modes is more influenced by mechanical boundary conditions of the plates. The effect of viscoelasticity on higher mode natural frequencies is almost similar under all support conditions.

Figure S26 (supplementary material) shows the effect of viscoelasticity on the first natural flexural frequencies of three-layered moderately thick (S = 10) inhomogeneous viscoelastic smart plate (b) having graded properties. The time-dependent variation of natural frequencies is plotted in non-dimensionalized form for different gradation cases under different edge conditions such as SSSS, CSSS, CCSS, CFSS. The non-dimensionalization is done by dividing the flexural frequencies of the viscoelastic plate by the flexural frequencies of the elastic plate without any gradation given in Table 7. It is found that the trend of viscoelatic effect on natural frequency is not affected much by inhomogeneity in composite layers, albeit the numerical values become different. For different gradation cases, the natural frequencies of the

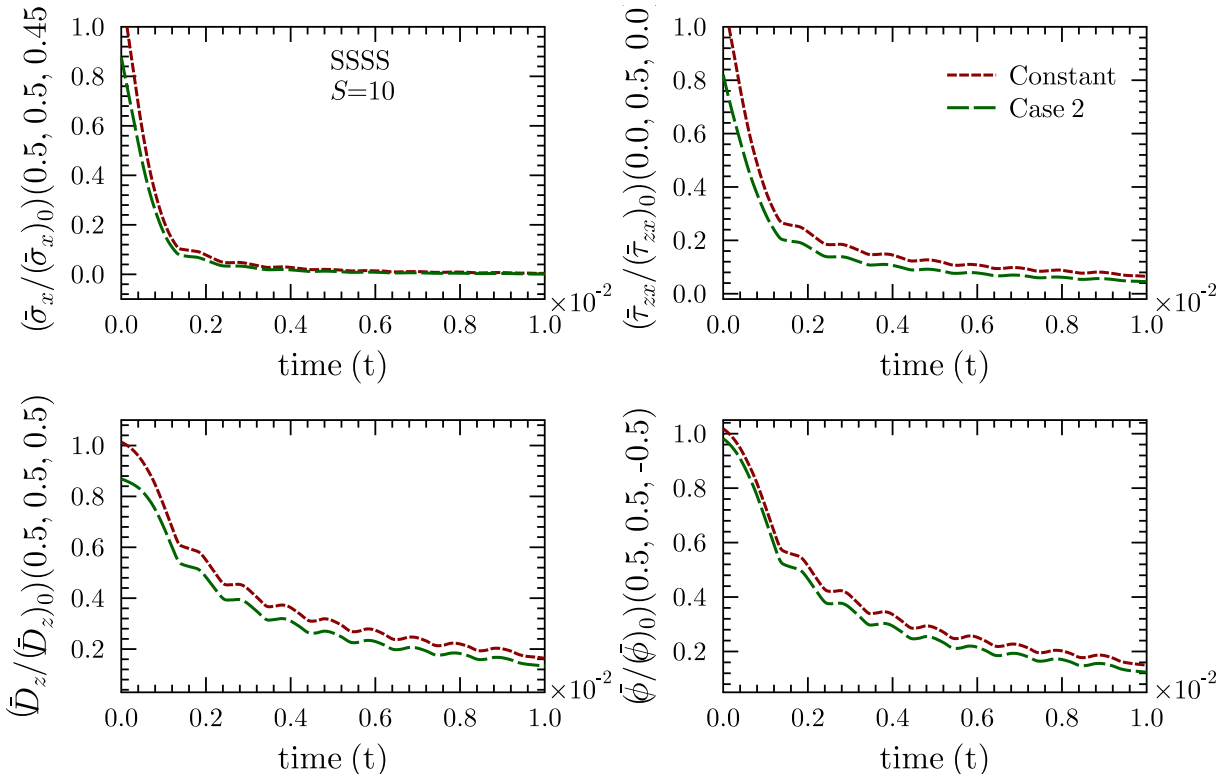

Fig. 10: Effect of viscoelasticity on the in-plane stress $\bar{\sigma}_x$, transverse stress $\bar{\sigma}_{zx}$, electric field $\bar{D}_z$ and electric potential $\bar{\phi}$ of three-layered moderately thick ($S = 10$) viscoelastic smart plate (a) with non-graded and graded properties. The time-dependent variation of in-plane stress $\bar{\sigma}_x$, transverse stress $\bar{\sigma}_{zx}$, electric field $\bar{D}_z$ and electric potential $\bar{\phi}$ is plotted in non-dimensionalized form for first vibration mode under SSSS boundary condition. The non-dimensionalized initial values of in-plane stress $(\bar{\sigma}_x)_0$ = -5.8047, transverse stress $(\bar{\sigma}_{zx})_0$ = 0.53780, electric field $(\bar{D}_z)_0$ = 3.1374 and electric potential $(\bar{\phi})_0$ = -2.3274 $\times 10^{-3}$ for non-viscous non-graded case are used for further normalization of the viscoelastic case.

plate decrease with time in a similar pattern under all mechanical support conditions. Figure 10 shows the influence of viscoelasticity on the in-plane stress $\bar{\sigma}_x$, transverse stress $\bar{\sigma}_{zx}$, electric field $\bar{D}_z$ and electric potential $\bar{\phi}$ of three-layered moderately thick ($S = 10$) viscoelastic smart plate (a) with non-graded and graded properties. The time-dependent variation of in-plane stress $\bar{\sigma}_x$, transverse stress $\bar{\sigma}_{zx}$, electric field $\bar{D}_z$ and electric potential $\bar{\phi}$ is plotted in non-dimensionalized form for first vibration mode under SSSS boundary condition. The non-dimensionalized initial values of in-plane stress $(\bar{\sigma}_x)_0$=-5.8047, transverse stress $(\bar{\sigma}_{zx})_0$=0.53780, electric field $(\bar{D}_z)_0$=3.1374 and electric potential $(\bar{\phi})_0$=-2.3274 $\times 10^{-3}$ for non-viscous non-graded case are used for further scaling of the viscoelastic case. It is observed that the stresses in the plate decrease fast with the increase in time and become constant after a certain value of time. Similar trend in time-dependent behavior of stresses are observed under the gradation of properties and for the non-graded case, albeit with a difference in numerical values. The time-dependent behavior of stresses is similar to time-dependent behaviors of viscoelastic properties like in Young's and shear moduli. However, electrical potential ($\bar{\phi}$) and electric field decrease ($\bar{D}_z$) gradually as time increases under both graded and non-graded case. It is also noted that the effect of gradation in elastic properties on electrical potential ($\bar{\phi}$) and electric field ($\bar{D}_z$) initially is very less but increases significantly as time grows. This shows that the gradation of material properties in the presence of viscoelasticity alters the electric response of piezoelectric layers to a significant extent. In general, the numerical study considering viscoelastic behaviour demonstrates a potential time-dependent structural behaviour, which could be crucial for analysing the mechanical behaviour of a wide range of polymer composites accurately and prospective time-dependent programming in smart structural systems.

6 Conclusions and perspective

The influence of in-plane gradation of stiffness and density on the free-vibration response of hybrid piezoelectric Levy-type plate is investigated by developing an accurate analytical solution. Further, the coupled effect of viscoelasticity and gradation on the natural frequency response of the IPFG smart viscoelastic plates is studied. The displacement, stresses, and electrical variables are solved as the primary variable by developing Hamilton's principle-based mixed formulation. A power series approach is used in conjunction with the extended Kantorovich method and Fourier series to obtain the closed-form analytical solution for Levy-type support condition. Biot model, which corresponds to a standard linear viscoelastic model, is coupled with the analytical framework to implement the viscoelasticity of composite layers in the analysis. Although the present analytical solution is developed for the elastic and viscoelastic analysis of smart in-plane functionally graded rectangular plates, it is also directly applicable for the natural frequency analysis of the symmetric and asymmetric laminated piezoelectric viscoelastic/elastic plates of constant properties.

An extensive numerical study is performed to assess the effect of in-plane gradation and viscoelasticity of material properties on natural frequencies and mode shapes of hybrid FGM plates. The benchmark numerical results are tabulated for various gradation cases and configurations under different electrical and mechanical support conditions. Numerical results for homogenous piezoelectric elastic/viscoelastic plates are also reported as a special case of the present study. The current results are validated with the results available in the open literature and 3D FE results by performing separate numerical simulations. It is found that the present EKM-power series analytical model is very efficient and accurate in depicting the flexural frequencies and mode shapes of the hybrid FGM viscoelastic and elastic plates. Some of the most significant outcomes of this study are listed below.

- The in-plane gradation of stiffness and density in the elastic layers significantly alters the flexural frequencies of the hybrid intelligent plate. As material properties variation indexes increase, the flexural frequencies of the smart plate decrease remarkably. When the gradation indexes become doubled (from 0.5 to 1), the percentage decrement in natural frequencies is almost raised by 1.5 times. The effect of gradation on free vibration response significantly depends upon the type of mechanical support conditions.
- The influence of gradation in lower mode natural frequencies specifically depends on mechanical support conditions of the hybrid plate. Further, percentage decrement in first and lower mode natural frequencies is different for different support conditions, while the effect of gradation in higher mode frequencies shows less sensitivity to support conditions. The decrement in higher mode natural frequencies almost remains the same for all boundary conditions. Another interesting finding is that the influence of in-plane gradation on flexural frequencies is not affected much by the electrical circuit conditions of piezoelectric layers.
- The mode shapes of the IPFG smart plate are affected significantly due to in-plane variation of stiffness and density. The symmetric mode shapes of the plate can be made asymmetrical by introducing appropriate gradation.
- The stresses in the smart FGM plates are influenced remarkably by in-plane variation of material properties. It is found that as the gradation index increases, the stresses in the IPFG smart plate decrease. But displacements, electric field, and electrical potential are not significantly affected by the gradation of stiffness and density.
- Though the in-plane gradation of stiffness and density significantly affects the flexural frequencies of the smart hybrid plate, their effect on the electric voltage of the piezoelectric layer is considerably less. This observation can play a significant role in the design of sensors or actuators for vibration control applications.
- The current investigation shows that the desired electromechanical responses of hybrid IPFG plate can be obtained by controlling the in-plane variation of material properties in the elastic layers. Based on the proposed efficient and accurate numerical framework, further studies can be undertaken to

simultaneously optimize multiple electrical and mechanical response parameters of interest in an expanded design space of layer-wise gradation parameters, material and geometric properties.

- For viscoelastic smart plates, the natural frequencies decrease gradually with time, whereas stresses in plate decrease fast and become constant after a critical time period. The decrement in electric response (in electric field and electric voltage) of the smart plate is also gradual. It is observed that the gradation of material properties in the presence of viscoelasticity significantly alters the electric response of piezoelectric layers. The presented numerical results demonstrate a great potential of the proposed viscoelastic analysis in the time domain for programming electromechanical responses of composite structures.
- Due to the consideration of viscoelastic effect, the natural frequencies decrease with time. The physical meaning of this variation is that the damping properties of viscoelastic layers diminish vibrational properties, while the damping behavior mainly depends upon the type of boundary conditions. It is worth noting that the natural frequencies decrease gradually with time, unlike viscoelastic properties, which decrease fast with the increase in time. The viscoelastic effect on lower vibration modes is more influenced by mechanical boundary conditions of the plates. The effect of viscoelasticity on higher mode natural frequencies is almost similar under all support conditions.

The numerical study demonstrates a potential time-dependent electromechanical behaviour based on the present viscoelastic modelling coupled with in-plane gradation, which could be crucial for analysing the structural behaviour of a wide range of 'intelligent' polymer composites accurately and prospective temporal programming in smart structural systems. The analytical results provided in this paper will serve as benchmarks to validate numerical algorithms in applications of natural frequency analysis for elastic/viscoelastic piezoelectric plates with or without gradation. Furthermore, the present analytical solution approach can also be extended to obtain analytical solutions for bending and free vibration analysis of multi-directional functionally graded smart plates.

Supplementary materials

1. Supplementary figures: Figure S1 to S26
2. Supplementary tables: Table S1 to S7
3. Supplementary texts: Appendix A to G

Acknowledgements

AS and TM would like to acknowledge the support received through the Science and Engineering Research Board (Grant no. SRG/2020/001398), India. SN acknowledges the initiation grant received from University of Southampton.

References

[1] F. Xu, X. Zhang, H. Zhang, A review on functionally graded structures and materials for energy absorption, Engineering Structures 171 (2018) 309–325.

[2] A. Garg, H. D. Chalak, R. Sahoo, T. Mukhopadhyay, Vibration and buckling analyses of sandwich plates containing functionally graded metal foam core, Acta Mechanica Solida Sinica, DOI: 10.1007/s10338-021-00295-z

[3] P. S. Ghatage, V. R. Kar, P. E. Sudhagar, On the numerical modelling and analysis of multi-directional functionally graded composite structures: A review, Composite Structures 236 (2020) 111837.

[4] V. Birman, L. W. Byrd, Modeling and analysis of functionally graded materials and structures, Applied mechanics reviews 60 (5) (2007) 195–216.

[5] C.-P. Wu, K.-H. Chiu, Y.-M. Wang, et al., A review on the three-dimensional analytical approaches of multilayered and functionally graded piezoelectric plates and shells, Comput Mater Continua 8 (2) (2008) 93–132.

[6] K. Swaminathan, D. Naveenkumar, A. Zenkour, E. Carrera, Stress, vibration and buckling analyses of fgm plates— a state-of-the-art review, Composite Structures 120 (2015) 10–31.

[7] P. Karsh, T. Mukhopadhyay, S. Dey, Stochastic dynamic analysis of twisted functionally graded plates, Composites Part B: Engineering 147 (2018) 259–278.

[8] Vaishali, T. Mukhopadhyay, P. Karsh, B. Basu, S. Dey, Machine learning based stochastic dynamic analysis of functionally graded shells, Composite Structures 237 (2020) 111870.
[9] K.B. Shingare , S. Naskar S., Probing the prediction of effective properties for composite materials, European Journal of Mechanics - A/Solids, 87 (2021) 104228.
[10] K.B. Shingare , S. Naskar S., Analytical solution for static and dynamic analysis of graphene-based hybrid flexoelectric nanostructures, Journal of Composites Science, DOI: 10.3390/jcs5030074
[11] S. Naskar, K. Shingare, S. Mondal, T. Mukhopadhyay, Flexoelectricity and Surface Effects on Coupled Electromechanical Responses of Graphene Reinforced Functionally Graded Nanocomposites: A unified size-dependent semi-analytical framework, Mechanical Systems and Signal Processing 169 (2022) 108757.
[12] P. Karsh, T. Mukhopadhyay, S. Dey, Stochastic low-velocity impact on functionally graded plates: Probabilistic and non-probabilistic uncertainty quantification, Composites Part B: Engineering 159 (2019) 461–480.
[13] M.-C. Trinh, T. Mukhopadhyay, S.-E. Kim, A semi-analytical stochastic buckling quantification of porous functionally graded plates, Aerospace Science and Technology 105 (2020) 105928.
[14] P. Karsh, T. Mukhopadhyay, S. Chakraborty, S. Naskar, S. Dey, A hybrid stochastic sensitivity analysis for low-frequency vibration and low-velocity impact of functionally graded plates, Composites Part B: Engineering 176 (2019) 107221.
[15] A. Leissa, A. Martin, Vibration and buckling of rectangular composite plates with variable fiber spacing, Composite Structures 14 (4) (1990) 339–357.
[16] J. Tomar, D. Gupta, N. Jain, Free vibrations of an isotropic non-homogeneous infinite plate of parabolically varying thickness, Indian J. pure appl. Math 15 (2) (1984) 211–220.
[17] M. Fares, A. Zenkour, Buckling and free vibration of non-homogeneous composite cross-ply laminated plates with various plate theories, Composite structures 44 (4) (1999) 279–287.
[18] D. Liu, C. Wang, W. Chen, Free vibration of FGM plates with in-plane material inhomogeneity, Composite Structures 92 (5) (2010) 1047–1051.
[19] T.-C. Yu, G.-J. Nie, Z. Zhong, F.-y. Chu, Analytical solution of rectangular plate with in-plane variable stiffness, Applied Mathematics and Mechanics 34 (2013) 395–404.
[20] M. Amirpour, R. Das, E. S. Flores, Analytical solutions for elastic deformation of functionally graded thick plates with in-plane stiffness variation using higher order shear deformation theory, Composites Part B: Engineering 94 (2016) 109–121.
[21] B. Uymaz, M. Aydogdu, S. Filiz, Vibration analyses of FGM plates with in-plane material inhomogeneity by Ritz method, Composite Structures 94 (4) (2012) 1398–1405.
[22] S. Yin, T. Yu, T. Q. Bui, X. Zheng, S. Tanaka, In-plane material inhomogeneity of functionally graded plates: A higher-order shear deformation plate isogeometric analysis, Composites Part B: Engineering 106 (2016) 273–284.
[23] O. S. Hussein, S. B. Mulani, Reliability analysis and optimization of in-plane functionally graded cnt-reinforced composite plates, Structural and Multidisciplinary Optimization 58 (3) (2018) 1221–1232.
[24] F. Chu, L. Wang, Z. Zhong, J. He, Hermite radial basis collocation method for vibration of functionally graded plates with in-plane material inhomogeneity, Computers & Structures 142 (2014) 79–89.
[25] P. Malekzadeh, A. Alibeygi Beni, Nonlinear free vibration of in-plane functionally graded rectangular plates, Mechanics of Advanced Materials and Structures 22 (8) (2015) 633–640.
[26] S. Yin, T. Yu, T. Q. Bui, X. Zheng, G. Yi, Rotation-free isogeometric analysis of functionally graded thin plates considering in-plane material inhomogeneity, Thin-Walled Structures 119 (2017) 385–395.
[27] S. Kumar, A. Mitra, H. Roy, Large amplitude free vibration study of non-uniform plates with in-plane material inhomogeneity, Proceedings of the Institution of Mechanical Engineers, Part L: Journal of Materials: Design and Applications 232 (5) (2018) 371–387.
[28] S.-Y. Kuo, L.-C. Shiau, Buckling and vibration of composite laminated plates with variable fiber spacing, Composite Structures 90 (2) (2009) 196–200.
[29] V. Haciyev, A. Sofiyev, N. Kuruoglu, Free bending vibration analysis of thin bidirectionally exponentially graded orthotropic rectangular plates resting on two-parameter elastic foundations, Composite Structures 184 (2018) 372–377.
[30] Y. Xue, G. Jin, H. Ding, M. Chen, Free vibration analysis of in-plane functionally graded plates using a refined plate theory and isogeometric approach, Composite Structures 192 (2018) 193–205.
[31] M. Loja, J. Barbosa, In-plane functionally graded plates: A study on the free vibration and dynamic instability behaviours, Composite Structures 237 (2020) 111905.
[32] C. Lü, W. Chen, J. Shao, Semi-analytical three-dimensional elasticity solutions for generally laminated composite plates, European Journal of Mechanics-A/Solids 27 (5) (2008) 899–917.
[33] C. Lü, C. W. Lim, W. Chen, Semi-analytical analysis for multi-directional functionally graded plates: 3-D elasticity solutions, International Journal for Numerical Methods in Engineering 79 (1) (2009) 25–44.

[34] A. Singh, P. Kumari, Two-dimensional elasticity solution for arbitrarily supported axially functionally graded beams, Journal of Solid Mechanics Vol 10 (4) (2018) 719–733.
[35] A. Singh, P. Kumari, Analytical solution of functionally graded beam having longitudinal stiffness variation, International Journal for Computational Methods in Engineering Science and Mechanics 19 (6) (2018) 390–395.
[36] A. Singh, P. Kumari, P. Bind, 2d free vibration solution of the hybrid piezoelectric laminated beams using extended kantorovich method, Journal of The Institution of Engineers (India): Series C 101 (1) (2020) 1–12.
[37] A. Singh, S. Kapuria, Analytical elasticity solution for accurate prediction of localized stresses in laminated composites under patch loading, European Journal of Mechanics-A/Solids 95 (2022) 104624.
[38] A. Singh, P. Kumari, R. Hazarika, Analytical solution for bending analysis of axially functionally graded angle-ply flat panels, Mathematical Problems in Engineering 2018.
[39] A. Singh, P. Kumari, Analytical free vibration solution for angle-ply piezolaminated plate under cylindrical bending: A piezo-elasticity approach, Advances in Computational Design 5 (1) (2020) 55–89.
[40] P. Kumari, A. Singh, R. Rajapakse, S. Kapuria, Three-dimensional static analysis of levy-type functionally graded plate with in-plane stiffness variation, Composite Structures 168 (2017) 780–791.
[41] A. Ravindran, K. Bhaskar, Three-dimensional analysis of composite fgm rectangular plates with in-plane heterogeneity, International Journal of Mechanical Sciences 160 (2019) 386–396.
[42] A. Ravindran, K. Bhaskar, Elasticity solution for a sandwich plate having composite facesheets with in-plane grading, Journal of Sandwich Structures & Materials (2020) 1099636220909810.
[43] P. Zhang, C. Qi, H. Fang, W. He, Three dimensional mechanical behaviors of in-plane functionally graded plates, Composite Structures 241 (2020) 112124.
[44] A. Singh, P. Kumari, Three-dimensional free vibration analysis of composite fgm rectangular plates with in-plane heterogeneity: An ekm solution, International Journal of Mechanical Sciences 180 (2020) 105711.
[45] K. Asemi, M. Salehi, M. Akhlaghi, Three dimensional static analysis of two dimensional functionally graded plates, IJMECH 2 (2) (2013) 21–32.
[46] T. Xiang, S. Natarajan, H. Man, C. Song, W. Gao, Free vibration and mechanical buckling of plates with in-plane material inhomogeneity– A three dimensional consistent approach, Composite Structures 118 (2014) 634–642.
[47] Y. Huang, Y. Zhao, D. Cao, Bending and free vibration analysis of orthotropic in-plane functionally graded plates using a chebyshev spectral approach, Composite Structures 255 (2021) 112938.
[48] A. Singh, T. Mukhopadhyay, S. Adhikari, B. Bhattacharya, Voltage-dependent modulation of elastic moduli in lattice metamaterials: Emergence of a programmable state-transition capability, International Journal of Solids and Structures 208-209 (2021) 31–48.
[49] H. Madinei, H. H. Khodaparast, S. Adhikari, M. Friswell, Design of mems piezoelectric harvesters with electrostatically adjustable resonance frequency, Mechanical Systems and Signal Processing 81 (2016) 360–374.
[50] G. Martínez-Ayuso, M. I. Friswell, H. H. Khodaparast, J. I. Roscow, C. R. Bowen, Electric field distribution in porous piezoelectric materials during polarization, Acta Materialia 173 (2019) 332–341.
[51] W. Chen, H. Ding, On free vibration of a functionally graded piezoelectric rectangular plate, Acta Mechanica 153 (3) (2002) 207–216.
[52] P. Lu, H. Lee, C. Lu, Exact solutions for simply supported functionally graded piezoelectric laminates by Stroh-like formalism, Composite Structures 72 (3) (2006) 352–363.
[53] S. Brischetto, E. Carrera, Refined 2d models for the analysis of functionally graded piezoelectric plates, Journal of Intelligent Material Systems and Structures 20 (15) (2009) 1783–1797.
[54] A. Zenkour, R. Alghanmi, Stress analysis of a functionally graded plate integrated with piezoelectric faces via a four-unknown shear deformation theory, Results in Physics 12 (2019) 268–277.
[55] S.-Q. Zhang, G.-Z. Zhao, M. N. Rao, R. Schmidt, Y.-J. Yu, A review on modeling techniques of piezoelectric integrated plates and shells, Journal of Intelligent Material Systems and Structures 30 (8) (2019) 1133–1147.
[56] P. Zhang, C. Qi, H. Fang, X. Sun, A semi-analytical approach for the flexural analysis of in-plane functionally graded magneto-electro-elastic plates, Composite Structures 250 (2020) 112590.
[57] P. Zhang, C. Qi, X. Sun, H. Fang, Y. Huang, Bending behaviors of the in-plane bidirectional functionally graded piezoelectric material plates, Mechanics of Advanced Materials and Structures (2020) 1–21.
[58] P. Zhang, C. Qi, H. Fang, X. Sun, Free vibration analysis of functionally graded magneto-electro-elastic plates with in-plane material heterogeneity, Journal of Intelligent Material Systems and Structures (2020) 1045389X20975487.

[59] J. Zhang, G. Zheng, The biot model and its application in viscoelastic composite structures, Journal of Vibration and Acoustics 129 (5) (2007) 533–540.
[60] M.-y. Hu, A.-w. Wang, Free vibration and transverse stresses of viscoelastic laminated plates, Applied Mathematics and Mechanics 30 (1) (2009) 101.
[61] Y. Mao, Y. Fu, H. Dai, Creep buckling and post-buckling analysis of the laminated piezoelectric viscoelastic functionally graded plates, European Journal of Mechanics-A/Solids 30 (4) (2011) 547–558.
[62] A. Zenkour, Bending responses of an exponentially graded simply-supported elastic/viscoelastic/elastic sandwich plate, Acta Mechanica Solida Sinica 24 (3) (2011) 250–261.
[63] Y. Wang, Z. Wang, L. Zu, Stability of viscoelastic rectangular plate with a piezoelectric layer subjected to follower force, Archive of Applied Mechanics 83 (4) (2013) 495–507.
[64] A. Alibeigloo, Effect of viscoelastic interface on three-dimensional static and vibration behavior of laminated composite plate, Composites Part B: Engineering 75 (2015) 17–28.
[65] P. Wu, D. Zhou, W. Liu, W. Lu, L. Wan, Three-dimensional elasticity solution of layered plates with viscoelastic interlayers, Mechanics of Time-Dependent Materials 21 (3) (2017) 307–329.
[66] M. Wang, Z. Yang, P. Wu, H. Fang, R. Huo, 3d analytical solution for multilayer functionally graded plates with viscoelastic interlayers, Mechanics Based Design of Structures and Machines (2021) 1–20.
[67] K. R. Karim, G. Chen, Surface damping effect of anchored constrained viscoelastic layers on the flexural response of simply supported structures, Mechanical Systems and Signal Processing 27 (2012) 419–432.
[68] S. C. Kattimani, M. Ray, Vibration control of multiferroic fibrous composite plates using active constrained layer damping, Mechanical Systems and Signal Processing 106 (2018) 334–354.
[69] J. S. Moita, A. L. Araújo, V. F. Correia, C. M. M. Soares, J. Herskovits, Active-passive damping in functionally graded sandwich plate/shell structures, Composite Structures 202 (2018) 324–332.
[70] F. Mastroddi, F. Martarelli, M. Eugeni, C. Riso, Time-and frequency-domain linear viscoelastic modeling of highly damped aerospace structures, Mechanical Systems and Signal Processing 122 (2019) 42–55.
[71] A. Batou, S. Adhikari, Optimal parameters of viscoelastic tuned-mass dampers, Journal of Sound and Vibration 445 (2019) 17–28.
[72] W. Sun, Z. Wang, X. Yan, M. Zhu, Inverse identification of the frequency-dependent mechanical parameters of viscoelastic materials based on the measured frfs, Mechanical Systems and Signal Processing 98 (2018) 816–833.
[73] P. Grosso, A. De Felice, S. Sorrentino, A method for the experimental identification of equivalent viscoelastic models from vibration of thin plates, Mechanical Systems and Signal Processing 153 (2021) 107527.
[74] A. Singh, P. Kumari, Two-dimensional free vibration analysis of axially functionally graded beams integrated with piezoelectric layers: An piezoelasticity approach, International Journal of Applied Mechanics 12 (04) (2020) 2050037.
[75] T. Mukhopadhyay, S. Adhikari, A. Batou, Frequency domain homogenization for the viscoelastic properties of spatially correlated quasi-periodic lattices, International Journal of Mechanical Sciences 150 (2019) 784–806.
[76] D. I. Jones, Handbook of viscoelastic vibration damping, John Wiley & Sons, 2001.
[77] R. Christensen, Theory of viscoelasticity: an introduction, Elsevier, 2012.
[78] P. A. M. Dirac, et al., The principles of quantum mechanics, no. 27, Oxford university press, 1981.
[79] L. Rouleau, J.-F. Deü, A. Legay, F. Le Lay, Application of kramers–kronig relations to time–temperature superposition for viscoelastic materials, Mechanics of Materials 65 (2013) 66–75.
[80] H. Booij, G. Thoone, Generalization of kramers-kronig transforms and some approximations of relations between viscoelastic quantities, Rheologica Acta 21 (1) (1982) 15–24.
[81] L. Xi, R. Luo, Use of kramers–kronig relations to construct the master curves of asphalt materials, Materials and Structures 54 (1) (2021) 1–16.
[82] M. Enelund, P. Olsson, Damping described by fading memory—analysis and application to fractional derivative models, International Journal of Solids and Structures 36 (7) (1999) 939–970.
[83] M. A. Biot, Variational principles in irreversible thermodynamics with application to viscoelasticity, Physical Review 97 (6) (1955) 1463.
[84] R. L. Bagley, P. J. Torvik, Fractional calculus-a different approach to the analysis of viscoelastically damped structures, AIAA journal 21 (5) (1983) 741–748.
[85] G. A. Lesieutre, D. L. Mingori, Finite element modeling of frequency-dependent material damping using augmenting thermodynamic fields, Journal of Guidance, Control, and Dynamics 13 (6) (1990) 1040–1050.
[86] D. J. McTavish, P. C. Hughes, Modeling of linear viscoelastic space structures, Journal of Vibration and Acoustics- ASME 115 (1) (1993) 103–110.

[87] S. Adhikari, Energy dissipation in vibrating structures, First Year Report, Cambridge University Engineering Department, Cambridge, UK.
[88] S. Adhikari, J. Woodhouse, Identification of damping: part 1, viscous damping, Journal of Sound and vibration 243 (1) (2001) 43–61.
[89] M. A. Ezzat, H. M. Youssef, Three-dimensional thermo-viscoelastic material, Mechanics of Advanced Materials and Structures 23 (1) (2016) 108–116.
[90] K. Barrett, A. Gotts, Fem for one-and two-dimensional viscoelastic materials with spherical and rotating domains using fft, Computers & structures 82 (2-3) (2004) 181–192.
[91] R. M. Gray, J. W. Goodman, Fourier transforms: An introduction for engineers, Vol. 322, Springer Science & Business Media, 2012.
[92] P. Kumari, A. Singh, Three-dimensional analytical solution for fgm plate with varying material properties in in-plane directions using extended kantorovich method, in: Recent Advances in Structural Engineering, Volume 1, Springer, 2019, pp. 611–621.
[93] S. Behera, P. Kumari, Analytical piezoelasticity solution for natural frequencies of levy-type piezolaminated plates, International Journal of Applied Mechanics 11 (03) (2019) 1950023.
[94] S. Kapuria, G. Achary, A coupled zigzag theory for the dynamics of piezoelectric hybrid cross-ply plates, Archive of Applied Mechanics 75 (1) (2005) 42–57.
[95] P. Heyliger, D. Saravanos, Exact free-vibration analysis of laminated plates with embedded piezoelectric layers, The Journal of the Acoustical Society of America 98 (3) (1995) 1547–1557.
[96] S. Malekmohammadi, B. Tressou, C. Nadot-Martin, F. Ellyin, R. Vaziri, Analytical micromechanics equations for elastic and viscoelastic properties of strand-based composites, Journal of Composite Materials 48 (15) (2014) 1857–1874.
[97] V. T. Endo, J. C. de Carvalho Pereira, Linear orthotropic viscoelasticity model for fiber reinforced thermoplastic material based on prony series, Mechanics of Time-Dependent Materials 21 (2) (2017) 199–221.
[98] D. Jalocha, A. Constantinescu, R. Neviere, Revisiting the identification of generalized maxwell models from experimental results, International Journal of Solids and Structures 67 (2015) 169–181.

Supplementary Material

Appendix A.

$$
\begin{array}{lll}
s_{11} = 1/Y_1, & s_{44} = 1/G_{23}, & s_{12} = -\nu_{21}/Y_2 = -\nu_{12}/Y_1 \\
s_{22} = 1/Y_2, & s_{55} = 1/G_{13}, & s_{13} = -\nu_{31}/Y_3 = -\nu_{13}/Y_1 \\
s_{33} = 1/Y_3, & s_{66} = 1/G_{12}, & s_{23} = -\nu_{32}/Y_3 = -\nu_{23}/Y_2 \\
\epsilon_{11} = \eta_{11} + e_{15}d_{15}, & \epsilon_{22} = \eta_{22} + e_{24}d_{24}, & \epsilon_{33} = \eta_{33} + e_{31}d_{31} + e_{32}d_{32} + e_{33}d_{33}
\end{array}
\tag{A.1}
$$

with

$$
\begin{aligned}
&[\, e_{31} \quad e_{32} \quad e_{33} \,] = [\, d_{31} \quad d_{32} \quad d_{33} \,] \begin{bmatrix} s_{11} & s_{12} & s_{13} \\ s_{12} & s_{22} & s_{23} \\ s_{13} & s_{23} & s_{33} \end{bmatrix}^{-1} \\
&e_{24} = d_{24}/s_{44}, \qquad e_{15} = d_{15}/s_{55}
\end{aligned}
\tag{A.2}
$$

Here Y_i, G_{ij} and ν_{ij} designate Young's moduli, shear moduli and Poisson's ratios, respectively.

Appendix B.

$$
\begin{array}{llll}
|E_i(\omega_s)| \to (E_s)_i \text{ for } \mu \to \infty & \text{and} & |E_i(\omega_s)| \to (E_s)_i(1+\bar{\varepsilon}_s) \text{ for } \mu \to 0 & \forall \omega_s > 0 \\
|G_{ij}(\omega_s)| \to (G_s)_{ij} \text{ for } \mu \to \infty & \text{and} & |G_{ij}(\omega_s)| \to (G_s)_{ij}(1+\bar{\varepsilon}_s) \text{ for } \mu \to 0 & \forall \omega_s > 0 \\
|E_i(\omega_s)| \to E_{si} \text{ for } \omega_s \to 0 & \text{and} & |E_i(\omega_s)| \to E_{si}(1+\bar{\varepsilon}_s) \text{ for } \omega_s \to \infty & \forall \mu > 0 \\
|G_i(\omega_s)| \to (G_s)_{ij} \text{ for } \omega_s \to 0 & \text{and} & |G_i(\omega_s)| \to (G_s)_{ij}(1+\bar{\varepsilon}_s) \text{ for } \omega_s \to \infty & \forall \mu > 0
\end{array}
\tag{B.1}
$$

$$
\phi_s\left(E_i(\omega_s)\right) = \phi_s\left(G_{ij}(\omega_s)\right) \to 0 \text{ for } \mu \to 0 \text{ and } \phi_s\left(E_i(\omega_s)\right) = \phi_s\left(G_{ij}(\omega_s)\right) \to 0 \text{ for } \mu \to \infty \qquad \forall \omega_s > 0
$$

$$
\phi_s\left(E_i(\omega_s)\right) = \phi_s\left(G_{ij}(\omega_s)\right) \to 0 \text{ for } \omega_s \to 0 \text{ and } \phi_s\left(E_i(\omega_s)\right) = \phi_s\left(G_{ij}(\omega_s)\right) \to 0 \text{ for } \omega_s \to \infty \qquad \forall \mu > 0
$$

Appendix C.

Using the notation $\langle \ldots \rangle_a = a \int_0^1 (\ldots) d\xi_1$ for integration over the span length (a), the non-zero elements of coefficient matrices $\mathbf{M}$, $\bar{\mathbf{A}}$, $\bar{\mathbf{A}}^{\mathbf{v}}$, $\hat{\mathbf{A}}$, $\hat{\mathbf{A}}^{\mathbf{v}}$, $\mathbf{K}^{\mathbf{m}}$, $\tilde{\mathbf{A}}$, $\tilde{\mathbf{A}}^{\mathbf{v}}$ are,

$$
\begin{aligned}
&M_{i_1 j_1} = M_{j_6 i_6} = \langle f_9^i f_1^j \rangle_a, \quad M_{i_2 j_2} = M_{j_5 i_5} = \langle f_8^i f_2^j \rangle_a, \quad M_{i_3 j_3} = M_{j_4 i_4} = \langle f_6^i f_3^j \rangle_a \\
&M_{i_7 j_7} = M_{j_8 i_8} = \langle f_{13}^i f_{10}^j \rangle_a, \; \bar{A}_{i_1 j_3} = \tfrac{-t}{a} \langle f_9^i f_{3,\xi_1}^j \rangle_a \qquad \bar{A}_{i_1 j_6} = t \bar{s}_{55} \langle f_9^i f_9^j \rangle_a, \\
&\bar{A}^v_{i_1 j_6} = \delta_2 t \langle \xi_1 \bar{s}_{55} f_9^i f_9^j \rangle_a \qquad \hat{A}_{i_1 j_4} = t \bar{d}_{15} \langle f_9^i f_{11}^j \rangle_a, \qquad \bar{A}_{i_2 j_3} = -\bar{m} t \langle f_8^i f_3^j \rangle_a \\
&\bar{A}_{i_2 j_5} = t \bar{s}_{44} \langle f_8^i f_8^j \rangle_a, \qquad \hat{A}_{i_2 j_5} = t \bar{d}_{24} \langle f_8^i f_{12}^j \rangle_a, \qquad \bar{A}_{i_3 j_4} = t \bar{s}_{33} \langle f_6^i f_6^j \rangle_a \\
&\hat{A}_{i_3 j_1} = t \bar{s}_{13} \langle f_6^i f_4^j \rangle_a, \qquad \hat{A}^v_{i_3 j_1} = \delta_1 t \langle \xi_1 \bar{s}_{13} f_6^i f_4^j \rangle_a, \qquad \hat{A}_{i_3 j_2} = t \bar{s}_{23} \langle f_6^i f_5^j \rangle_a \\
&\bar{A}_{i_3 j_8} = t \bar{d}_{33} \langle f_6^i f_{13}^j \rangle_a, \qquad \bar{A}_{i_4 j_5} = \bar{m} t \langle f_3^i f_8^j \rangle_a, \qquad \bar{A}_{i_4 j_6} = \tfrac{-t}{a} \langle f_3^i f_{9,\xi_1}^j \rangle_a, \\
&\hat{A}_{i_5 j_2} = -\bar{m} t \langle f_2^i f_5^j \rangle_a, \qquad \hat{A}_{i_5 j_3} = \tfrac{-t}{a} \langle f_2^i f_{7,\xi_1}^j \rangle_a, \qquad \hat{A}_{i_6 j_1} = \tfrac{-t}{a} \langle f_1^i f_{4,\xi_1}^j \rangle_a \\
&\hat{A}_{i_6 j_3} = \bar{m} t \langle f_1^i f_7^j \rangle_a, \qquad \bar{A}_{i_7 j_4} = t \bar{d}_{33} \langle f_{13}^i f_6^j \rangle_a, \qquad \bar{A}_{i_7 j_8} = -t \bar{\epsilon}_{33} \langle f_{13}^i f_{13}^j \rangle_a \\
&\hat{A}_{i_7 j_1} = t \bar{d}_{31} \langle f_{13}^i f_4^j \rangle_a, \qquad \hat{A}_{i_7 j_2} = t \bar{d}_{32} \langle f_{13}^i f_5^j \rangle_a, \qquad \hat{A}_{i_8 j_4} = \tfrac{-t}{a} \langle f_{10}^i f_{11,\xi_1}^j \rangle_a \\
&\hat{A}_{i_8 j_5} = t \bar{m} \langle f_{10}^i f_{12}^j \rangle_a, \qquad K_{i_1 j_1} = \bar{s}_{11} \langle f_4^i f_4^j \rangle_a, \qquad K_{i_1 j_2} = \bar{s}_{12} \langle f_4^i f_5^j \rangle_a \\
&K^v_{i_1 j_1} = \delta_1 \langle \xi_1 \bar{s}_{11} f_4^i f_4^j \rangle_a, \qquad K^v_{i_1 j_2} = \delta_1 \langle \xi_1 \bar{s}_{12} f_4^i f_5^j \rangle_a, \qquad K_{i_2 j_1} = K_{i_1 j_2} \\
&K^v_{i_2 j_1} = K^v_{i_1 j_2}, \qquad K_{i_2 j_2} = \bar{s}_{22} \langle f_5^i f_5^j \rangle_a, \qquad K_{i_3 j_3} = \bar{s}_{66} \langle f_7^i f_7^j \rangle_a \\
&K^v_{i_3 j_3} = \delta_2 \langle \xi_1 \bar{s}_{66} f_7^i f_7^j \rangle_a, \qquad K_{i_4 j_4} = \bar{\epsilon}_{11} \langle f_{11}^i f_{11}^j \rangle_a, \qquad K_{i_5 j_5} = \bar{\epsilon}_{22} \langle f_{12}^i f_{12}^j \rangle_a \\
&\tilde{A}_{i_1 j_1} = \tfrac{1}{a} \langle f_4^i f_{1,\xi_1}^j \rangle_a, \qquad \tilde{A}_{i_1 j_4} = -\bar{s}_{13} \langle f_4^i f_6^j \rangle_a, \qquad \tilde{A}^v_{i_1 j_4} = -\delta_1 \langle \xi_1 \bar{s}_{13} f_4^i f_6^j \rangle_a \\
&\tilde{A}_{i_1 j_8} = -\bar{d}_{31} \langle f_4^i f_{13}^j \rangle_a, \qquad \tilde{A}_{i_2 j_2} = -\bar{m} \langle f_5^i f_2^j \rangle_a, \qquad \tilde{A}_{i_2 j_4} = -\bar{s}_{23} \langle f_5^i f_6^j \rangle_a \\
&\tilde{A}_{i_2 j_8} = -\bar{d}_{32} \langle f_5^i f_{13}^j \rangle_a, \qquad \tilde{A}_{i_3 j_1} = \bar{m} \langle f_7^i f_1^j \rangle_a \qquad \tilde{A}_{i_3 j_2} = \tfrac{1}{a} \langle f_7^i f_{2,\xi_1}^j \rangle_a \\
&\tilde{A}_{i_4 j_6} = \bar{d}_{15} \langle f_{11}^i f_9^j \rangle_a, \qquad \tilde{A}_{i_4 j_7} = -\tfrac{1}{a} \langle f_{11}^i f_{10,\xi_1}^j \rangle_a, \qquad \tilde{A}_{i_5 j_5} = \bar{d}_{24} \langle f_{12}^i f_8^j \rangle_a \\
&\tilde{A}_{i_5 j_7} = -\bar{m} \langle f_{12}^i f_{10}^j \rangle_a, \qquad \bar{A}_{i_4 j_3} = -\rho \omega^2 t \langle f_3^i f_3^j \rangle_a, \qquad \bar{A}^v_{i_4 j_3} = -\delta_p \omega^2 t \langle \rho \, \xi_1 f_3^i f_3^j \rangle_a \\
&\bar{A}_{i_5 j_2} = -\rho \omega^2 t \langle f_2^i f_2^j \rangle_a, \qquad \bar{A}^v_{i_5 j_2} = -\delta_p \omega^2 t \langle \rho \, \xi_1 f_2^i f_2^j \rangle_a, \; \bar{A}_{i_6 j_1} = -\rho \omega^2 t \langle f_1^i f_1^j \rangle_a \\
&\bar{A}^v_{i_6 j_1} = -\delta_p \omega^2 t \langle \rho \, \xi_1 f_1^i f_1^j \rangle_a
\end{aligned}
\tag{C.1}
$$

Since the functions f_l^i are presumed for first starting iteration, the coefficient element, given in Eq. (C.1), could be solved in closed-form by performing integration along x-direction.

Appendix D.

The solution of

$$\bar{\mathbf{G}}_{,\zeta} = \mathbf{A}(\omega)\bar{\mathbf{G}} \tag{D.1}$$

is assumed in this form $\bar{\mathbf{G}}_{\mathbf{c}}(\zeta) = e^{\lambda\zeta}\mathbf{Y}$. This assumed solution is substituted in Eq. (D.1) and it leads to an eigenvalue problem $\mathbf{AY} = \lambda\mathbf{Y}$. In this equation, λ represents $8n$ eigenvalues which can be complex or real. $\mathbf{Y}$ represents corresponding $8n$ eigenvector pairs of matrix $\mathbf{A}$ which are functions of flexural frequency ω. Then, the final solution of Eq. (D.1) can be expressed as

$$\bar{\mathbf{G}}(\zeta) = \sum_{i=1}^{8n} \mathbf{G}_i(\zeta,\omega)C_i \tag{D.2}$$

Here $\mathbf{G}_i(\zeta,\omega)$ represents a column vector which is the function of corresponding eigenvalue (λ_i) and eigenvector (Y_i) pairs. C_i is unknown coefficients which depend upon shear traction free condition of top and bottom surface. After applying $8n(L-1)$ interface continuity conditions and $8n$ shear traction free constraints conditions of exterior (top and bottom) surface, equation (D.2) is transformed to the following form,

$$\sum_{i=1}^{8n} \mathbf{K}_{\mathbf{d}i}(\zeta,\omega)C_i = \mathbf{0} \tag{D.3}$$

Here, the matrix $\mathbf{K_d}$ is the function of flexural frequencies (ω_n). The determinant of coefficient matrix $\mathbf{K_d}$ is zero ($|det(\mathbf{K_d})|$=0) for a nontrivial solution and flexural frequencies (ω_n) can be obtained by solving the equation $|det(\mathbf{K_d})|$=0. In the present paper bisection method is employed to find roots of the equation $|det(\mathbf{K_d})|$=0. In this way, natural frequencies ω_{01} ($\omega_{01} = \omega_n$) have been obtained for first iteration.

Appendix E.

The nonzero elements of $\mathbf{N}_{8n\times 8n}$, $\bar{\mathbf{B}}_{8n\times 8n}$, $\bar{\mathbf{B}}^{\mathbf{v}}_{8n\times 8n}$, $\hat{\mathbf{B}}_{8n\times 5n}$, $\hat{\mathbf{B}}^{\mathbf{v}}_{8n\times 5n}$, $\mathbf{L}_{5n\times 5n}$, $\tilde{\mathbf{B}}_{5n\times 8n}$ and $\tilde{\mathbf{B}}^{\mathbf{v}}_{5n\times 8n}$ matrices are given below

$$
\begin{aligned}
&N_{i_1j_1} = N_{j_4i_4} = \langle g_4^i g_1^j\rangle_h, \quad N_{i_2j_2} = N_{j_5i_5} = \langle g_7^i g_2^j\rangle_h, \quad N_{i_3j_3} = N_{j_6i_6} = \langle g_9^i g_3^j\rangle_h \\
&N_{i_7j_7} = N_{j_8i_8} = \langle g_{10}^i g_{11}^j\rangle_h, \ \bar{B}_{i_1j_4} = a\langle \bar{s}_{11} g_4^i g_4^j\rangle_h, \quad \hat{B}_{i_1j_1} = a\langle \bar{s}_{12} g_4^i g_5^j\rangle_h \\
&\bar{B}^v_{i_1j_4} = a\delta_1\xi_1\langle \bar{s}_{11} g_4^i g_4^j\rangle_h, \quad \hat{B}_{i_1j_2} = a\langle \bar{s}_{13} g_4^i g_6^j\rangle_h, \quad \hat{B}^v_{i_1j_1} = \delta_1\xi_1 a\langle \bar{s}_{12} g_4^i g_5^j\rangle_h \\
&\hat{B}^v_{i_1j_2} = \delta_1\xi_1 a\langle \bar{s}_{13} g_4^i g_6^j\rangle_h, \quad \hat{B}_{i_1j_5} = \langle \bar{d}_{31} g_4^i g_{13}^j\rangle_h, \quad \bar{B}_{i_2j_1} = -\bar{m}\ a\langle g_7^i g_1^j\rangle_h \\
&\bar{B}_{i_2j_5} = a\langle \bar{s}_{66} g_7^i g_7^j\rangle_h, \quad \bar{B}^v_{i_2j_5} = \delta_2\xi_1\ a\langle \bar{s}_{66} g_7^i g_7^j, \quad \bar{B}_{i_3j_1} = -a\langle g_9^i \tfrac{g_{1,\zeta}^j}{t}\rangle_h\rangle_h \\
&\bar{B}_{i_3j_6} = a\langle \bar{s}_{55} g_9^i g_9^j\rangle_h, \quad \bar{B}^v_{i_3j_6} = \delta_2\xi_1 a\langle \bar{s}_{55} g_9^i g_9^j\rangle_h, \quad \bar{B}_{i_3j_8} = a\langle \bar{d}_{15} g_9^i g_{11}^j\rangle_h \\
&\bar{B}_{i_4j_5} = \bar{m}\ a\langle g_1^i g_7^j\rangle_h, \quad \bar{B}_{i_4j_6} = a\langle \tfrac{g_{1,\zeta}^i}{t} g_9^j\rangle_h, \quad \hat{B}_{i_5j_1} = -\bar{m}\ a\langle g_2^i g_5^j\rangle_h \\
&\hat{B}_{i_5j_3} = a\langle \tfrac{g_{2,\zeta}^i}{t} g_8^j\rangle_h, \quad \hat{B}_{i_6j_2} = -a\langle g_3^i \tfrac{g_{6,\zeta}^j}{t}\rangle_h, \quad \hat{B}_{i_6j_3} = a\ \bar{m}\langle g_3^i g_8^j\rangle_h \\
&\bar{B}_{i_7j_8} = -a\langle \bar{\epsilon}_{11} g_{11}^i g_{11}^j\rangle_h, \quad \bar{B}_{i_7j_6} = a\langle \bar{d}_{15} g_{11}^i g_9^j\rangle_h, \quad \hat{B}_{i_8j_4} = a\bar{m}\langle g_{10}^i g_{12}^j\rangle_h \\
&\hat{B}_{i_8j_5} = -a\langle g_{10}^i \tfrac{g_{13,\zeta}^j}{t}\rangle_h, \quad L_{i_1j_1} = \langle \bar{s}_{22} g_5^i g_5^j\rangle_h, \quad L_{i_1j_2} = \langle \bar{s}_{23} g_5^i g_6^j\rangle_h \\
&L_{i_1j_5} = \langle \bar{d}_{32} g_5^i g_{13}^j\rangle_h, \quad L_{i_2j_2} = \langle \bar{s}_{33} g_6^i g_6^j\rangle_h, \quad L_{i_2j_1} = L_{i_1j_2} \\
&L_{i_2j_5} = \langle \bar{d}_{33} g_6^i g_{13}^j\rangle_h, \quad L_{i_3j_3} = \langle \bar{s}_{44} g_8^i g_8^j\rangle_h, \quad L_{i_3j_4} = \langle \bar{d}_{24} g_8^i g_{12}^j\rangle_h \\
&L_{i_4j_3} = L_{i_3j_4}, \quad L_{i_4j_4} = -\langle \bar{\epsilon}_{22} g_{12}^i g_{12}^j\rangle_h, \quad L_{i_5j_1} = \langle \bar{d}_{32} g_{13}^i g_5^j\rangle_h \\
&L_{i_5j_2} = \langle \bar{d}_{33} g_{13}^i g_6^j\rangle_h, \quad L_{i_5j_5} = -\langle \bar{\epsilon}_{33} g_{13}^i g_{13}^j\rangle_h, \quad \tilde{B}_{i_1j_2} = -\bar{m}\langle g_5^i g_2^j\rangle_h \\
&\tilde{B}_{i_1j_4} = -\langle \bar{s}_{12} g_5^i g_4^j\rangle_h, \quad \tilde{B}^v_{i_1j_4} = \delta_1\xi_1\langle \bar{s}_{12} g_5^i g_4^j\rangle_h, \quad \tilde{B}_{i_2j_3} = \langle g_6^i \tfrac{g_{3,\zeta}^j}{t}\rangle_h \\
&\tilde{B}_{i_2j_4} = -\langle \bar{s}_{13} g_6^i g_4^j\rangle_h, \quad \tilde{B}^v_{i_2j_4} = -\delta_1\xi_1\langle \bar{s}_{13} g_6^i g_4^j\rangle_h, \quad \tilde{B}_{i_3j_3} = \bar{m}\langle g_8^i g_3^j\rangle_h \\
&\tilde{B}_{i_3j_2} = \langle g_8^i \tfrac{g_{2,\zeta}^j}{t}\rangle_h, \quad \tilde{B}_{i_4j_7} = \bar{m}\langle g_{12}^i g_{10}^j\rangle_h, \quad \tilde{B}_{i_5j_4} = -\langle \bar{d}_{31} g_{13}^i g_4^j\rangle_h \\
&\tilde{B}_{i_5j_7} = \langle g_{13}^i \tfrac{g_{10,\zeta}^j}{t}\rangle_h, \quad \bar{B}_{i_4j_1} = -a\rho\omega^2\langle g_1^i g_1^j\rangle_h, \quad \bar{B}^v_{i_4j_1} = -\delta_p\, a\rho\omega^2\xi_1\langle g_1^i g_1^j\rangle_h \\
&\bar{B}_{i_5j_2} = -a\rho\omega^2\langle g_2^i g_2^j\rangle_h, \quad \bar{B}^v_{i_5j_2} = -\delta_p\, a\rho\omega^2\xi_1\langle g_2^i g_2^j\rangle_h, \ \bar{B}_{i_6j_3} = -a\rho\omega^2\langle g_3^i g_3^j\rangle_h \\
&\bar{B}^v_{i_6j_3} = -\delta_p\, a\rho\omega^2\xi_1\langle g_3^i g_3^j\rangle_h
\end{aligned}
\tag{E.1}
$$

Here notation $\langle \ldots\rangle_h = \sum_{k=1}^{L} t^{(k)} \int_0^1 (\ldots)^{(k)}\, d\zeta$ indicates integration across the thickness. However, $g_l^i(\zeta)$ are already known in closed-form from previous iteration, hence all above elements (E.1) can also be solved exactly in closed form by executing integration over ζ direction on the known g_l^i functions.

Appendix F.

The final solution for the current system of variable coefficient ODEs

$$\bar{\mathbf{F}}_{,\xi_1} = \{\mathbf{B_0}(\omega) + \xi_1 \mathbf{B_1}(\omega) + \xi_1^2 \mathbf{B_2}\}\bar{\mathbf{F}} \tag{F.1}$$

can be expressed in the following power series form,

$$\bar{\mathbf{F}}^j(\xi_1) = \left(\sum_{i=0}^{n_p} \mathbf{H}_i^j \xi_1^i\right) \mathbf{C}_0 \tag{F.2}$$

By substituting assumed solution, Eq.(F.2), into Eq.(F.1) following recursive relations are obtained for $\mathbf{H}_i$,

$$\begin{aligned} &\hat{\mathbf{H}}_0 = \mathbf{I}; \quad \hat{\mathbf{H}}_1 = \mathbf{B_0}; \quad \hat{\mathbf{H}}_2 = \mathbf{B_0}\hat{\mathbf{H}}_1 + \mathbf{B_1} \\ &\hat{\mathbf{H}}_{i+1} = \mathbf{B_0}\hat{\mathbf{H}}_1 + i\mathbf{B_1}\hat{\mathbf{H}}_{i-1} + i(i-1)\mathbf{B_2}\hat{\mathbf{H}}_{i-2} \quad \text{for} \quad i \geq 2 \end{aligned} \tag{F.3}$$

Here, n_p is total number of terms in power series which has been taken large enough that makes sure that the contribution of next succeeding terms will be nominal and should be less than η $(= 10^{-10})$. $\mathbf{C}_0$ is unknown coefficient vector which can be obtained after applying mechanical and electrical boundary conditions in ξ_1-direction. When the boundary conditions of end $\xi_1 = 0$ and $\xi_1 = 1$ are applied, Eq. (F.2) leads to,

$$\sum_{i=1}^{8n} \mathbf{K_d}_i(\xi_1, \omega) C_i = \mathbf{0} \tag{F.4}$$

where the coefficient matrix $\mathbf{K_d}$ for this iteration is function of $\omega = \omega_m$. Similarly for nontrivial solution its determinant must be zero. So, ω_m has been obtained by solving equation $|det(\mathbf{K_d})|$=0 employing the root finding techniques called as bisection method.

Appendix G.

Remark 1. ***Advantages of the proposed mathematical model compared to others approaches.*** *In recent studies, it has been shown that the displacement-based 3D FE solutions fail to predict the sharp variation of transverse stresses in the composite/FGM structures as it fails to satisfy the traction-free conditions at the top and bottom surfaces, particularly where there are sharp stress gradients, such as near clamped edges [Ref. 4,30,32,66,81,82]. On the other hand, the proposed multi-term mixed-field extended Kantorovich method (MMEKM) is very robust and accurate in solving such 3D piezo-elasticity problems and able to satisfy all boundary and inter-facial continuity conditions exactly in a strong sense as the formulation is developed in mixed form. Here, mixed form means that the displacements, stresses, and electrical variables (electric field and electric potential) are solved as the primary variables. It is also worth mentioning that the accuracy of the current model is not affected by the span to thickness ratio (S) and configurations of laminates. It is equally efficient and accurate for thick to thin plates and also for symmetric to highly in-homogeneous asymmetric laminates, where the use of classical 2D laminate theories is limited to thin and symmetric laminates [Ref. 3-5].*

Remark 2. ***Poling in piezoelectric material.*** *Piezoelectric materials in the natural case are composed of microscopic electric dipoles with random orientation, rendering the overall polarization of the material zero. When stress is applied to this piezoelectric material through a mechanical force, it will result in a very small polarization. Hence, natural piezoelectric materials show a weak piezoelectric effect. In order to make the piezoelectric material much more piezoelectric sensitive and effective, initial directions of such dipoles need to be oriented in the direction of the applied forces. This process of forcing the dipoles to orient themselves in a prescribed direction is called poling. It is usually performed by applying a strong electric field in the prescribed direction for a sufficiently long time. After removing the electric field, most of the dipoles would remain in their initial orientation. The process of poling piezoelectric material is very similar to the magnetization of magnetic material, where one applies a sufficiently strong magnetic field to align the internal microscopic magnetic dipole moments of the material. After the removal of the magnetizing magnetic field, the dipoles hold their orientation gained by the magnetization.*

Remark 3. ***Fourier series approach for y-direction solution.*** *To obtain the solution for y-direction of plate, Fourier series approach is utilized and solution is assumed in form of Fourier series in such a*

manner that it satisfies simply-supported end conditions ($\sigma_y = w = u = 0$ at edges $\xi_2 = 0, 1$) of y direction.

$$[u,\, w,\, \sigma_x,\, \sigma_y,\, \sigma_z,\, \tau_{zx},\, \phi,\, D_x,\, D_z] = \sum_{m=1}^{\infty} [(u,\, w,\, \sigma_x,\, \sigma_y,\, \sigma_z,\, \tau_{zx},\, \phi,\, D_x,\, D_z)_m \cos\omega t] \sin m\pi\xi_2$$

$$[v,\, \tau_{yz},\, \tau_{xy},\, D_y] = \sum_{m=1}^{\infty} [(v,\, \tau_{yz},\, \tau_{xy},\, D_y)_m \cos\omega t] \cos m\pi\xi_2 \tag{F.5}$$

where $(\ )_m$ denotes the m^{th} term of Fourier series, and it is the function of ξ_1 and ζ. Here, ξ_2 is the y-direction coordinate parameter which is given by $\xi_2 = y/b$. Hence, ξ_2 always has a value from 0 to 1 for any value of b (length of the plate along y direction). Hence, $\xi_2 = 0$ at $y = 0$ and $\xi_2 = 1$ at $y = b$. Thus assumed Fourier series satisfies given simply supported condition at the end y=0 and y=b [$sin(0) = 0$ and $sin(pi) = 0$]. In the present study, no material and geometrical discontinuity is considered along the y-direction. Thus, the present domain will always be continuous, so the assumed form of the Fourier series is enough to satisfy the boundary conditions in $L^2(0, 1)$. Moreover, for simply-supported condition at y=0, b (which is roller type support and closed circuit) the variable 'v' and its corresponding variables (τ_{yz}, τ_{xy} and D_y) should not be zero to depict the exact closed-circuit simply-supported conditions. Hence, $cos(m\pi\xi_2)$ is used with the Fourier series for these variables.

Remark 4. ***Derivation Kramers–Kronig relations.*** *The bidirectional mathematical relations of Kramers–Kronig connects the real and imaginary parts of any complex function or signal that is analytic in the upper half-plane. These relations are usually employed during signal processing to calculate the real part of signal from the imaginary part of signal (or vice versa) in physical systems.*

Let $\chi(\omega_s) = \chi_1(\omega_s) + i\chi_2(\omega_s)$ be a complex function (signal) of the complex variable ω_s, where $\chi_1(\omega_s)$ and $\chi_2(\omega_s)$ are real. Similarly, if $\chi(\omega_s)$ is analytic function in the closed upper half-plane of ω_s, then function $\omega_s' \to \chi(\omega_s')/(\omega_s' - \omega_s)$ will also be analytic in the upper half of the plane. Further, contour is chosen as a hump over the pole at $\omega_s' = \omega_s$, and a large semicircle in the upper half plane to trace the real axis. Hence, according to the residue theorem for any closed contour within this region.

$$\oint \frac{\chi(\omega_s')}{\omega_s' - \omega_s}\, d\omega_s' = 0 \tag{F.6}$$

Then the integral is passed to limits after decomposing into its contributions along each of these three contour segments. The length of segment corresponds to semicircular increaseas respectively to $|\omega_s'|$. However, the integral over it become zero on the limits because $\chi(\omega_s')$ approaching zero faster than $1/|\omega_s'|$

$$0 = \oint \frac{\chi(\omega_s')}{\omega_s' - \omega_s}\, d\omega_s' = \mathcal{P}_s \int_{-\infty}^{\infty} \frac{\chi(\omega_s')}{\omega_s' - \omega_s}\, d\omega_s' - i\pi\chi(\omega_s). \tag{F.7}$$

Hence,

$$\chi(\omega_s) = \frac{1}{i\pi}\mathcal{P}_s \int_{-\infty}^{\infty} \frac{\chi(\omega_s')}{\omega_s' - \omega_s}\, d\omega_s' \tag{F.8}$$

The relation between the real and imaginary components of signal is proved by single i in the denominator. Finally, $\chi(\omega_s)$ can be obtained into their real and imaginary parts from the equation $\chi(\omega_s) = \chi_1(\omega_s) + i\chi_2(\omega_s)$. The imaginary part of a signal (response function) indicates the way of system in which it losses (dissipates) energy. The Kramers–Kronig relations suggest that the dissipated response of a signal or system is enough to determine its out of phase response, and vice versa. The integration from $-\infty$ to ∞ indicates the inclusion of negative and positive frequencies. Generally, the negative-frequency response of a signal or a system can be determined by its positive frequency-response because in most physical systems, $\chi(\omega_s)$ is the Fourier transform of response $\chi(t)$ corresponds to real-valued where it is assumed that the $\chi(-\omega_s) = \chi^*(\omega_s)$. It indicates that $\chi_1(\omega_s)$ represents the even function in frequency domain and $\chi_2(\omega_s)$ represents odd function in frequency domain. By employing these properties, the integration ranges can be reduced to $[0, \infty)$. The multiplication of the numerator and denominator of the integral part by $(\omega_s' + \omega_s)$ and separation gives the real part $\chi_1(\omega_s)$ as

$$\chi_1(\omega_s) = \frac{1}{\pi}\mathcal{P}_s \int_{-\infty}^{\infty} \frac{\omega_s' \chi_2(\omega_s')}{(\omega_s')^2 - (\omega_s)^2}\, d\omega_s' + \frac{\omega_s}{\pi}\mathcal{P}_s \int_{-\infty}^{\infty} \frac{\chi_2(\omega_s')}{(\omega_s')^2 - (\omega_s)^2}\, d\omega_s'. \tag{F.9}$$

Here, $\chi_2(\omega_s)$ is odd, Hence, the second integral becomes zero and it gives

$$\chi_1(\omega_s) = \frac{2}{\pi}\mathcal{P}_s\int_0^\infty \frac{\omega_s'\chi_2(\omega_s')}{(\omega_s')^2-(\omega_s)^2}\,d\omega_s'. \tag{F.10}$$

The same procedure for the imaginary part produces

$$\chi_2(\omega_s) = -\frac{2}{\pi}\mathcal{P}_s\int_0^\infty \frac{\omega_s\chi_1(\omega_s')}{(\omega_s')^2-(\omega_s)^2}\,d\omega_s' = -\frac{2\omega_s}{\pi}\mathcal{P}_s\int_0^\infty \frac{\chi_1(\omega_s')}{(\omega_s')^2-(\omega_s)^2}\,d\omega_s' \tag{F.11}$$

This form of Kramers–Kronig relations is beneficial for the physical interpretation of the response of the signals or functions.

Remark 5. ***Kramers–Kronig causality relations: Derivation of Equations 21, 22, 23 and 24.*** *The frequency dependence of the viscoelastic material's properties can be described by a complex modulus $G_s(\omega_s)$:*

$$G_s^*(\omega_s) = G_s'(\omega_s) + \iota G_s''(\omega_s) = |G_s(\omega_s)|e^{\iota\phi_s(\omega_s)} \tag{F.12}$$

where $G_s'(\omega_s)$ and $G_s''(\omega_s)$ are storage moduli and loss moduli, $|G_s(\omega_s)|$ is the amplitude and $\phi_s(\omega_s)$ is the phase angle. In the context of linear viscoelasticity, the constitutive law which links the stress $\sigma_t(t)$ to the strain $\varepsilon(t)$ can be written in its convolution form [69]

$$\sigma_t(t) = G_s(t) \circledast \varepsilon(t) \tag{F.13}$$

If the initial strain is $\varepsilon(t) = 0$ for $t \leq 0$, and the modulus is written as

$$G_s(t) = G_s(t \longrightarrow 0) - g_t(t) \tag{F.14}$$

the stress-strain relationship becomes,

$$\sigma_t(t) = G_s(t \longrightarrow 0)\varepsilon(t) - g_t(t) \circledast \varepsilon(t) \tag{F.15}$$

The causality conditions requires the memory function $g_t(t)$ to be causal, i.e., $g_t(t) = 0, \forall t < 0$. The Fourier transform of a real linear causal function $g_t(t)$ that does not possess any singularity at $t = 0$ respects certain relations between its real and imaginary parts [75-77],

$$\Re(g_t^*(\omega_s)) = \tfrac{2}{\pi}\textstyle\int_0^\infty \frac{u\Im(g_t^*(u_s))}{\omega_s^2-u_s^2}\,du_s \tag{F.16}$$

$$\Im(g_t^*(\omega_s)) = \tfrac{2\omega_s}{\pi}\textstyle\int_0^\infty \frac{\Re(g_t^*(u_s))}{u_s^2-\omega_s^2}\,du_s \tag{F.17}$$

Using Eq. (F.12) and the Fourier transform of Eq. (F.14) ($G^*(\omega_s) = G_{s\infty} - g_t^*(\omega_s)$) in Eqs. (F.16) and (F.17) lead to the so-called Kramers-Kronig relations (Remark 4) linking the real and the imaginary parts of the complex modulus [73,75-79],

$$G_s'(\omega_s) = G_{s\infty} + \frac{2}{\pi}\int_0^\infty \frac{uG_s''(u_s)}{\omega_s^2-u_s^2}\,du_s \tag{F.18}$$

$$G_s''(\omega_s) = \frac{2\omega_s}{\pi}\int_0^\infty \frac{G_s'(u_s)}{u_s^2-\omega_s^2}\,du_s \tag{F.19}$$

where $G_{s\infty} = G_s^*(\omega_s \to \infty) = G_t(t \to 0)$ is the unrelaxed modulus. Similar equations link the logarithm of the modulus amplitude to the phase angle, the complex elastic modulus $G_s^*(\omega_s)$ can be expressed, as Eq. (F.12), $G_s^*(\omega_s) = G_s'(\omega_s) + \iota G_s''(\omega_s) = |G_s(\omega_s)|e^{\iota\phi_s(\omega_s)}$. By converting it to logarithmic form [77], $\ln G_s^*(\omega_s) = \ln G_s'(\omega_s) + \iota \ln G_s''(\omega_s) = \ln|G_s(\omega_s)| + \iota\phi_s(\omega_s)$, and using the same method as above, $|G_s'(\omega_s)|$ and ϕ_s can thus be formulated as,

$$\ln|G_s'(\omega_s)| = \ln|G_{s\infty}| + \frac{2}{\pi}\int_0^\infty \frac{u_s\phi_s(u_s)}{\omega_s^2-u_s^2}\,du_s \tag{F.20}$$

$$\phi_s(\omega_s) = \frac{2\omega_s}{\pi}\int_0^\infty \frac{\ln|G_s(u_s)|}{u_s^2-\omega_s^2}\,du_s \tag{F.21}$$

Additional numerical results

Table S1: Comparison of first ten lowest natural frequencies ($\omega^* = \omega a S\sqrt{\rho_0/Y_0}$) for composite piezoelectric smart plates (d) subjected to closed circuit (CC) condition at top ($\phi(x, y, h/2)$=0) and open circuit condition at bottom ($D_z(x, y, -h/2)$=0).

			1	2	3	4	5	6	7	8	9	10
	SSSS	Present	7.181	13.595	13.830	18.371	20.932	21.690	24.525	24.896	28.818	29.442
		3D [82]	7.181	13.594	13.821	18.367	20.931	21.632	24.523	24.884	28.817	29.448
	CSSS	Present	7.449	13.802	13.898	18.494	21.133	21.707	24.687	24.972	29.131	29.457
		3D [82]	7.476	13.838	13.901	18.514	21.160	21.656	24.708	25.057	28.890	29.513
S=5	CCSS	Present	7.751	13.967	13.977	18.612	21.338	21.726	24.847	25.048	29.203	29.472
		3D [82]	7.887	14.018	14.150	18.713	21.460	21.680	24.981	25.162	29.488	29.925
	CFSS	Present	4.691	9.407	12.239	15.356	16.121	20.487	20.548	22.757	23.501	26.644
		3D [82]	4.715	9.449	12.284	15.409	16.202	20.570	20.582	22.746	23.434	26.774
		Present	3.907	5.521	10.891	11.840	12.958	16.655	17.637	20.297	21.022	21.982
	FFSS	3D [82]	4.028	5.514	11.314	11.851	13.081	17.234	17.745	20.330	21.135	22.581
	SSSS	Present	9.369	19.622	21.236	28.727	34.090	35.019	40.808	40.878	49.492	50.098
		3D [82]	9.369	19.614	21.236	28.724	34.047	35.019	40.796	40.876	49.491	50.098
	CSSS	Present	10.568	20.004	22.214	29.270	34.214	35.671	41.072	41.345	50.004	50.279
		3D [82]	10.551	20.000	22.251	29.292	34.187	35.716	41.375	41.375	50.047	50.156
S=10	CCSS	Present	11.844	20.424	23.084	29.797	34.346	36.300	41.337	41.801	50.326	50.491
		3D [82]	11.589	20.427	23.266	29.903	34.352	36.461	41.076	41.375	50.047	50.156
	CFSS	Present	5.623	13.905	16.671	22.852	26.487	31.725	33.318	36.311	40.219	44.492
		3D [82]	5.651	13.601	16.956	22.849	26.523	31.843	33.382	36.450	40.121	44.519
	FFSS	Present	4.391	6.720	15.925	16.418	17.961	25.628	29.354	31.402	32.684	36.571
		3D [82]	4.532	6.706	16.120	16.659	17.666	25.695	30.240	31.422	32.679	37.183

Table S2: Convergence study on the natural frequencies ($\omega^* = \omega a S\sqrt{\rho_0/E_0}$) of moderately thick ($S$ = 10) IPFG smart piezoelectric plate (a) subjected to SSSS and CCSS boundary conditions.

	SSSS					CCSS				
	Iter.1		Iter.2			Iter.1		Iter.2		
m	Step 1 (0-1)	Step 2 (1-1)	Step 1 (2-1)	Step 2 (2-2)	3D FE	Step 1 (0-1)	Step 2 (1-1)	Step 1 (2-1)	Step 2 (2-2)	3D FE
ω^*_{11}	9.240	8.682	8.682	8.682	8.691	9.240	12.978	12.979	12.978	13.099
ω^*_{21}	24.926	23.791	23.791	23.791	23.836	24.926	27.151	27.261	27.264	27.542
ω^*_{31}	42.782	41.515	41.515	41.515	41.580	42.782	43.648	43.759	43.763	44.260
ω^*_{41}	60.864	59.642	59.642	59.642	59.734	60.864	60.946	61.039	61.041	61.726
ω^*_{51}	78.830	77.696	77.696	77.696	77.823	78.830	78.555	78.700	78.703	79.483
ω^*_{12}	15.384	14.958	14.958	14.958	14.986	15.384	17.390	17.665	17.665	17.506
ω^*_{22}	28.813	27.779	27.778	27.779	27.832	28.813	30.393	30.488	30.489	30.724
ω^*_{32}	45.628	44.380	44.380	44.380	44.450	45.628	46.188	46.294	46.296	46.747
ω^*_{42}	63.158	61.897	61.897	61.897	61.987	63.158	63.061	63.147	63.149	63.795
ω^*_{52}	80.774	79.563	79.563	79.563	79.687	80.774	80.344	80.408	80.406	81.241
ω^*_{13}	25.291	24.938	24.938	24.938	24.972	25.291	26.131	26.132	26.133	26.275
ω^*_{23}	35.978	35.142	35.143	35.142	35.195	35.978	36.927	37.011	37.002	37.192
ω^*_{33}	50.920	49.791	49.792	49.791	49.865	50.920	51.219	51.321	51.322	51.697
ω^*_{43}	67.350	66.132	66.132	66.132	66.229	67.350	67.133	67.224	67.225	67.796
ω^*_{53}	84.261	83.038	83.038	83.038	83.164	84.261	83.739	83.812	83.813	84.573

Table S3: Influence of in-plane gradation of density and stiffness on natural flexural frequencies ($\omega^* = \omega a S\sqrt{\rho_0/E_0}$) of moderately thick ($S = 10$) IPFG smart piezoelectric plate (a) subjected to SSSS boundary conditions.

	Constant		Case (1)		Case (2)		Case (3)	
ω^*_{nm}	Present	3D FE	Present	3D FE	Present	3D FE	Present	3D FE
ω^*_{11}	10.152	10.152	8.682	8.691	7.602	7.668	6.708	6.847
ω^*_{21}	28.262	28.262	23.791	23.836	20.568	20.688	18.297	18.594
ω^*_{31}	49.430	49.430	41.515	41.580	35.799	35.965	32.474	32.876
ω^*_{41}	70.945	70.946	59.642	59.734	51.420	51.651	47.249	47.745
ω^*_{51}	92.163	92.165	77.696	77.823	67.055	67.363	62.121	62.708
ω^*_{12}	16.779	16.779	14.958	14.986	13.558	13.633	12.528	12.658
ω^*_{22}	32.417	32.416	27.779	27.832	24.405	24.544	22.225	22.510
ω^*_{32}	52.408	52.408	44.380	44.450	38.559	38.737	35.319	35.704
ω^*_{42}	73.276	73.278	61.897	61.987	53.601	53.827	49.484	49.954
ω^*_{52}	94.071	94.074	79.563	79.687	68.873	69.166	63.972	64.525
ω^*_{13}	27.461	27.461	24.938	24.972	22.919	22.980	21.397	21.499
ω^*_{23}	40.044	40.045	35.142	35.195	31.516	31.651	29.244	29.487
ω^*_{33}	57.934	57.934	49.791	49.865	43.840	44.029	40.597	40.950
ω^*_{43}	77.559	77.560	66.132	66.229	57.757	57.998	53.640	54.085
ω^*_{53}	97.543	97.544	83.038	83.164	72.305	72.609	67.393	67.926

Table S4: Influence of in-plane gradation of density and stiffness on natural flexural frequencies ($\omega^* = \omega a S\sqrt{\rho_0/E_0}$) of moderately thick ($S = 10$) IPFG smart piezoelectric plate (a) subjected to CSSS boundary conditions.

	Constant		Case (1)		Case (2)		Case (3)	
ω^*_{nm}	Present	3D FE	Present	3D FE	Present	3D FE	Present	3D FE
ω^*_{11}	12.764	12.741	10.922	10.911	9.558	9.584	8.645	8.608
ω^*_{21}	30.456	30.614	25.903	26.000	22.586	22.672	20.458	20.575
ω^*_{31}	50.739	51.038	42.977	43.154	37.340	37.480	34.275	34.438
ω^*_{41}	71.694	72.117	60.635	60.900	52.585	52.804	48.359	48.938
ω^*_{51}	93.626	93.115	78.395	78.752	67.979	68.283	63.337	63.650
ω^*_{12}	18.240	18.295	16.115	16.174	14.522	14.588	13.408	13.488
ω^*_{22}	34.137	34.273	29.408	29.495	25.945	26.027	23.846	23.953
ω^*_{32}	53.534	53.807	45.634	45.793	39.881	40.008	36.847	36.998
ω^*_{42}	73.947	74.335	63.278	63.032	54.647	54.848	50.784	50.999
ω^*_{52}	94.447	94.969	80.208	80.553	69.715	70.017	65.085	65.388
ω^*_{13}	28.206	28.280	25.466	25.538	23.311	23.379	21.748	21.818
ω^*_{23}	41.251	41.361	36.251	36.327	32.539	32.613	30.295	30.387
ω^*_{33}	58.847	59.075	50.804	50.932	44.908	45.013	41.810	41.934
ω^*_{43}	78.145	78.497	66.918	67.127	58.687	58.859	54.776	54.958
ω^*_{53}	97.895	98.365	83.635	83.941	73.091	73.357	68.414	68.679

Table S5: Influence of in-plane gradation of density and stiffness on natural flexural frequencies ($\omega^* = \omega a S\sqrt{\rho_0/E_0}$) of moderately thick ($S = 10$) IPFG smart piezoelectric plate (a) subjected to SFSS boundary conditions.

	Constant		Case (1)		Case (2)		Case (3)	
ω^*_{nm}	Present	3D FE	Present	3D FE	Present	3D FE	Present	3D FE
ω^*_{11}	4.023	4.055	3.527	3.562	3.166	3.205	2.938	2.970
ω^*_{21}	14.828	14.836	12.621	12.677	11.007	11.116	9.688	9.870
ω^*_{31}	34.555	34.487	29.260	29.308	25.388	25.542	22.600	22.936
ω^*_{41}	56.174	56.486	47.502	47.814	41.124	41.526	37.298	37.945
ω^*_{51}	77.544	78.157	65.674	66.202	56.860	57.457	52.232	53.087
ω^*_{12}	12.485	12.584	11.105	11.208	10.069	10.175	9.323	9.417
ω^*_{22}	21.216	21.221	18.530	18.614	16.550	16.719	15.198	15.415
ω^*_{32}	38.705	38.766	33.135	33.287	29.052	29.315	26.382	26.780
ω^*_{42}	59.148	59.397	50.316	50.596	43.808	44.194	40.070	40.662
ω^*_{52}	79.810	80.582	67.882	68.539	58.997	59.616	54.421	55.467
ω^*_{13}	24.172	24.321	21.551	21.718	19.545	19.722	18.058	18.216
ω^*_{23}	31.244	31.265	27.921	28.017	25.416	25.599	23.718	23.938
ω^*_{33}	45.971	46.026	40.050	40.220	35.679	35.977	32.985	33.373
ω^*_{43}	64.518	64.722	55.494	55.809	48.814	49.260	45.104	45.699
ω^*_{53}	83.982	84.669	71.977	72.550	62.994	63.627	58.431	59.257

Table S6: Influence of in-plane gradation of density and stiffness on natural flexural frequencies ($\omega^* = \omega a S\sqrt{\rho_0/E_0}$) of moderately thick ($S = 10$) IPFG smart piezoelectric plate (a) subjected to FFSS boundary conditions.

	Constant		Case (1)		Case (2)		Case (3)	
ω^*_{nm}	Present	3D FE	Present	3D FE	Present	3D FE	Present	3D FE
ω^*_{11}	3.148	3.206	2.919	2.965	2.726	2.764	2.566	2.595
ω^*_{21}	5.664	5.758	4.952	5.135	4.528	4.696	4.323	4.481
ω^*_{31}	20.412	20.353	17.239	17.317	14.985	15.173	13.182	13.478
ω^*_{41}	41.068	40.943	34.508	34.748	29.794	30.232	26.655	27.269
ω^*_{51}	62.866	63.669	52.881	53.739	45.614	46.602	41.496	42.317
ω^*_{12}	11.624	11.760	10.701	10.822	9.867	9.980	9.186	9.284
ω^*_{22}	14.528	14.579	13.230	13.328	12.347	12.486	11.850	11.984
ω^*_{32}	26.484	26.462	22.922	23.073	20.376	20.662	18.700	19.032
ω^*_{42}	45.164	45.549	38.375	38.862	33.492	34.069	30.492	31.152
ω^*_{52}	65.720	65.479	55.651	56.409	48.302	49.209	44.283	45.318
ω^*_{13}	23.402	23.595	21.372	21.550	19.455	19.673	18.063	18.191
ω^*_{23}	26.083	26.172	24.187	24.305	22.944	23.055	21.934	22.121
ω^*_{33}	35.986	35.931	31.905	32.042	29.004	29.261	27.224	27.527
ω^*_{43}	52.144	52.356	45.068	45.505	39.945	40.537	36.994	37.637
ω^*_{53}	70.875	71.773	60.682	61.635	53.210	54.248	49.245	50.372

Table S7: Influence of in-plane gradation of density and stiffness on lowest six natural flexural frequencies ($\omega^* = \omega a S\sqrt{\rho_0/E_0}$) of thick ($S = 5$, $t_p = 0.1h$) IPFG smart plate (b) subjected to different circuit conditions at top and bottom surface.

			Close-Close Circuit				Open-Close Circuit			
Mode no.			Constant	Case 1	Case 2	Case 3	Constant	Case 1	Case 2	Case 3
SSSS	1	ω^*_{11}	7.511	6.731	6.122	5.717	7.623	6.839	6.226	5.820
	2	ω^*_{12}	12.476	11.545	10.772	10.235	12.526	11.688	10.907	10.366
	3	ω^*_{21}	16.130	14.093	12.553	11.843	16.249	14.208	12.662	11.959
	4	ω^*_{13}	18.501	17.312	16.271	15.484	18.637	17.442	16.395	15.603
	5	ω^*_{22}	19.266	17.248	15.697	14.939	19.401	17.379	15.821	15.065
	6	ω^*_{23}	23.752	21.704	20.009	19.201	23.877	21.826	20.206	19.317
CSSS	1	ω^*_{11}	8.194	7.336	6.655	6.242	8.288	7.427	6.742	6.328
	2	ω^*_{12}	12.776	11.777	10.950	10.396	12.914	11.910	11.077	10.519
	3	ω^*_{21}	16.466	14.487	12.971	12.270	16.578	14.595	13.072	12.377
	4	ω^*_{13}	18.644	17.405	16.330	15.532	18.775	17.532	16.452	15.649
	5	ω^*_{22}	19.519	17.527	15.971	15.207	19.648	17.651	16.090	15.326
	6	ω^*_{23}	23.937	21.890	20.256	19.354	24.058	22.009	20.370	19.467
CCSS	1	ω^*_{11}	8.925	7.826	7.003	6.612	9.001	7.898	7.072	6.685
	2	ω^*_{12}	13.099	11.968	11.067	10.524	13.224	12.088	11.183	10.635
	3	ω^*_{21}	16.742	14.614	13.039	12.367	16.850	14.716	13.135	12.469
	4	ω^*_{13}	18.796	17.492	16.381	15.588	18.923	17.615	16.498	15.700
	5	ω^*_{22}	19.754	17.634	16.026	15.276	19.877	17.752	16.140	15.388
	6	ω^*_{23}	24.118	21.970	20.294	19.397	24.235	22.084	20.405	19.506
CFSS	1	ω^*_{11}	4.425	4.027	3.709	3.483	4.437	4.039	3.721	3.495
	2	ω^*_{12}	10.311	9.495	8.831	8.308	10.379	9.556	8.888	8.360
	3	ω^*_{21}	10.614	9.607	8.783	8.269	10.700	9.688	8.863	8.351
	4	ω^*_{22}	14.973	13.772	12.776	12.156	15.060	13.862	12.866	12.246
	5	ω^*_{13}	16.905	15.608	14.530	13.657	16.990	15.682	14.599	13.720
	6	ω^*_{31}	19.235	17.198	15.558	14.770	19.322	17.310	15.667	14.890
SFSS	1	ω^*_{11}	3.978	3.663	3.409	3.212	4.008	3.690	3.433	3.235
	2	ω^*_{21}	10.156	9.141	8.331	7.811	10.243	9.227	8.417	7.901
	3	ω^*_{12}	10.212	9.429	8.787	8.271	10.289	9.497	8.849	8.327
	4	ω^*_{22}	14.705	13.518	12.551	11.944	14.798	136.614	12.647	12.040
	5	ω^*_{13}	16.869	15.591	14.522	13.651	16.958	15.667	14.591	13.714
	6	ω^*_{31}	18.859	16.740	15.063	14.283	18.973	16.862	15.180	14.411
FFSS	1	ω^*_{11}	3.308	3.132	2.976	2.838	3.341	3.163	3.006	2.866
	2	ω^*_{21}	5.456	5.090	4.816	4.641	5.462	5.101	4.816	4.642
	3	ω^*_{12}	9.688	9.145	8.623	8.158	9.768	9.220	8.691	8.219
	4	ω^*_{22}	11.550	10.885	10.383	10.061	11.582	10.921	10.426	10.109
	5	ω^*_{31}	12.996	11.549	10.459	9.892	13.059	11.614	10.521	9.964
	6	ω^*_{13}	16.456	15.466	14.478	13.627	16.548	15.548	14.549	13.692

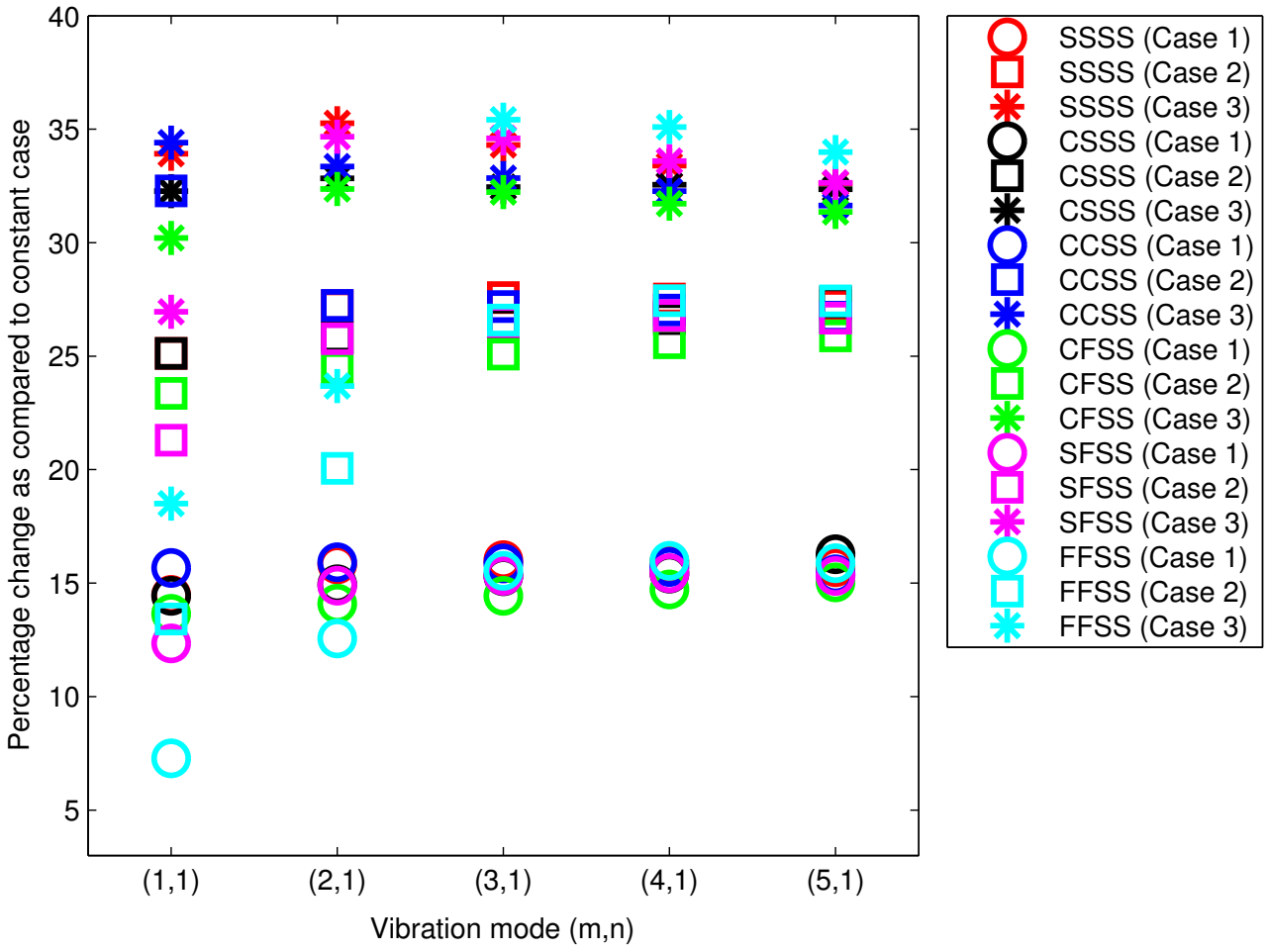

Fig. S1: Percentage decrement in first five lowest natural flexural frequencies of IPFG smart plate (a) due to in-plane gradation of density and stiffness under SSSS, CSSS, CCSS, CFSS, SFSS and FFSS boundary conditions ($S = 10$, $m = 1$).

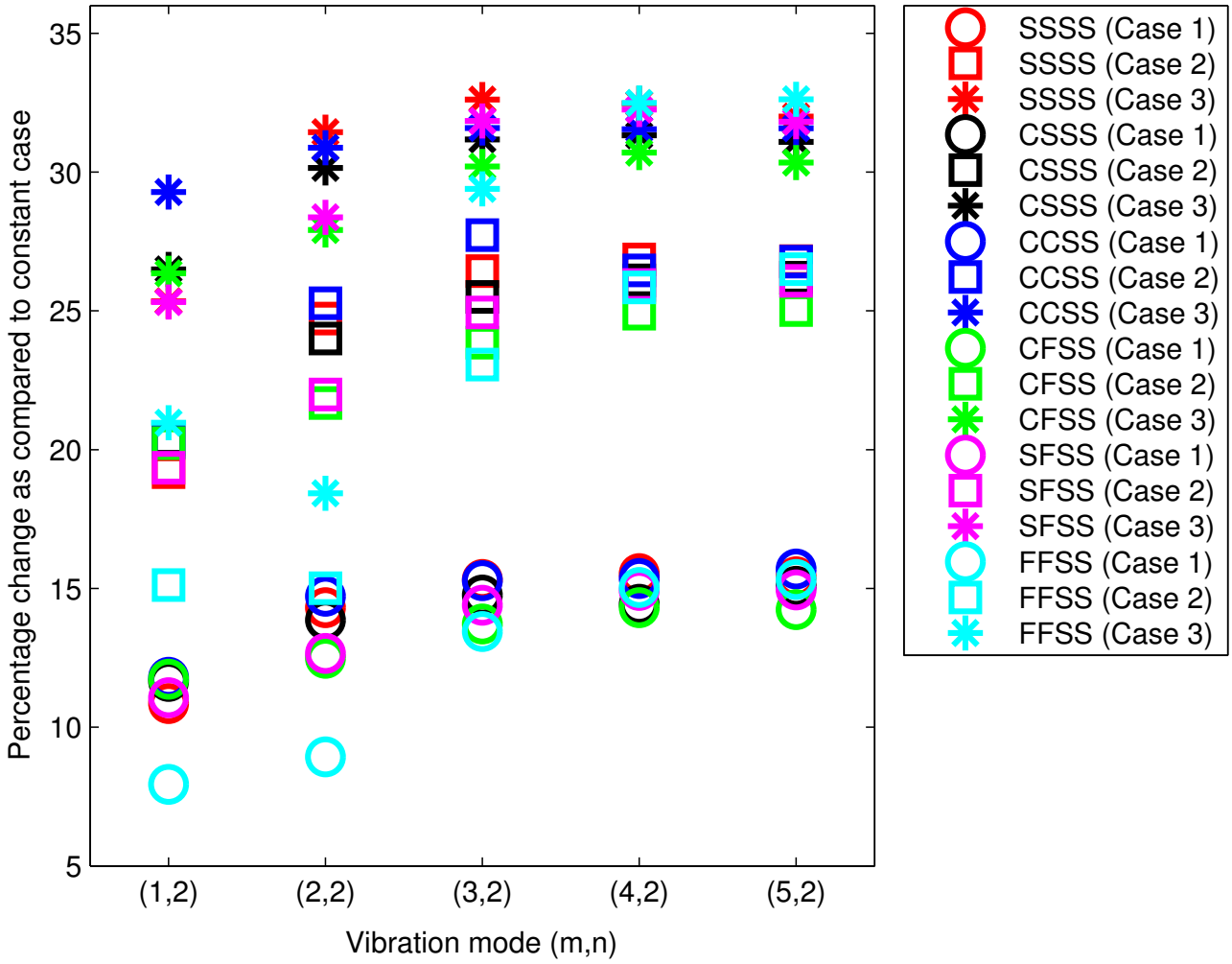

Fig. S2: Percentage decrement in first five lowest natural flexural frequencies of IPFG smart plate (a) due to in-plane gradation of density and stiffness under SSSS, CSSS, CCSS, CFSS, SFSS and FFSS boundary conditions ($S = 10$, $m = 2$).

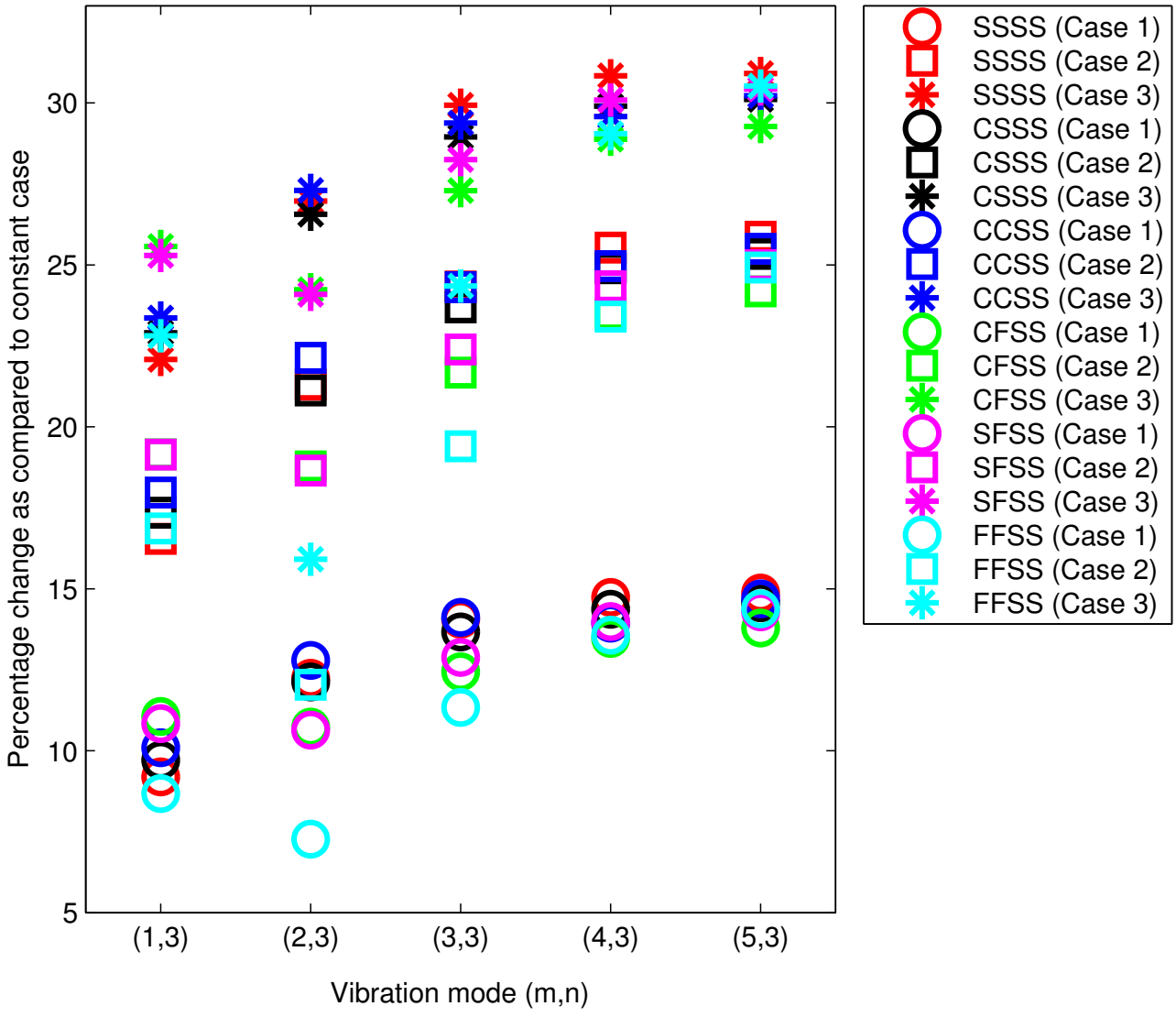

Fig. S3: Percentage decrement in first five lowest natural flexural frequencies of IPFG smart plate (a) due to in-plane gradation of density and stiffness under SSSS, CSSS, CCSS, CFSS, SFSS and FFSS boundary conditions ($S = 10$, $m = 3$).

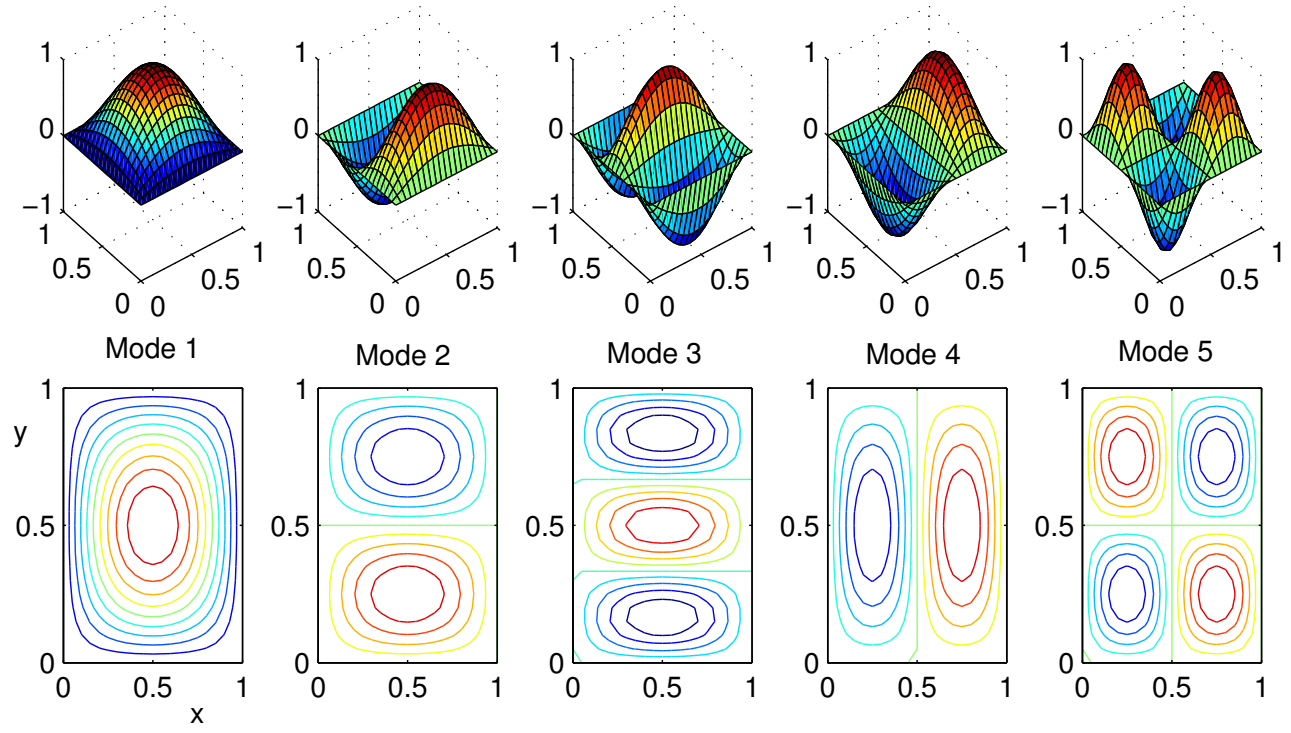

Fig. S4: First five flexural mode shapes for moderately thick ($S = 10$) IPFG smart plate (a) under constant properties case, and subjected to all around supported–simply supported (SSSS) boundary conditions.

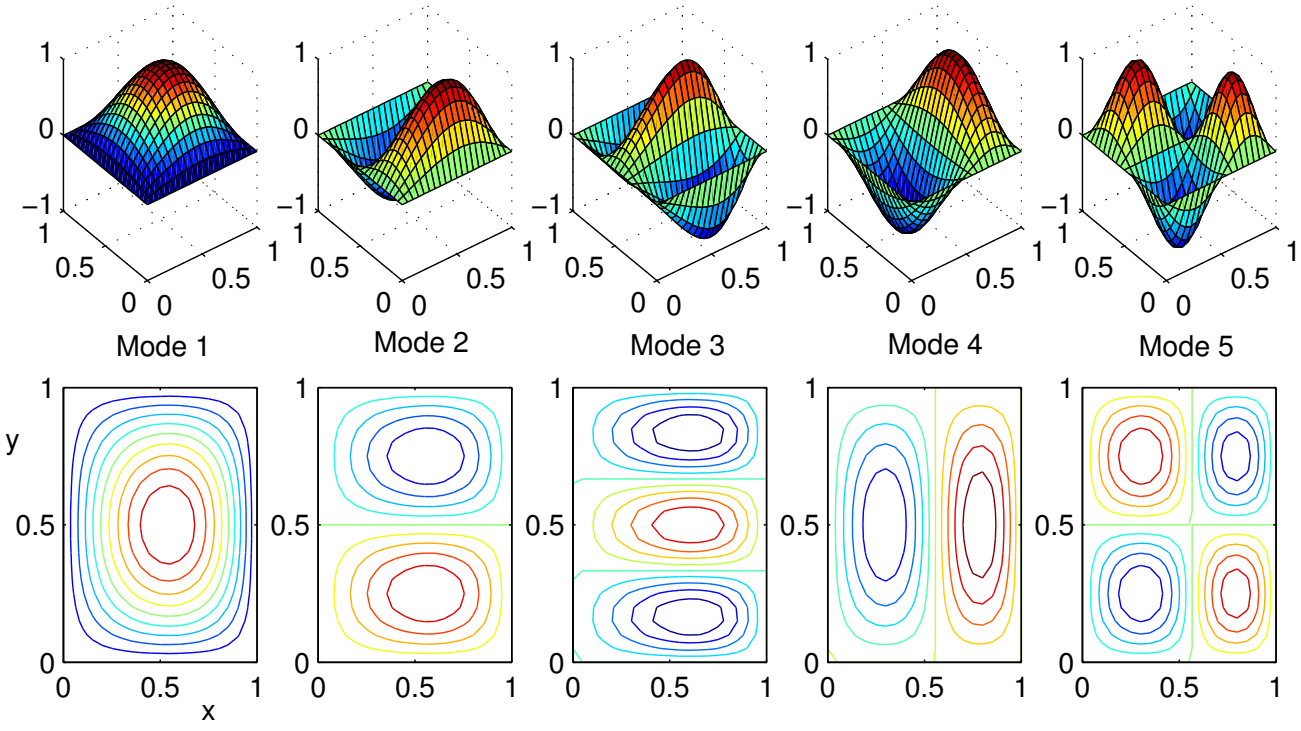

Fig. S5: First five flexural mode shapes for moderately thick ($S = 10$) IPFG smart plate (a) under gradation case 1, and subjected to all around supported–simply supported (SSSS) boundary conditions.

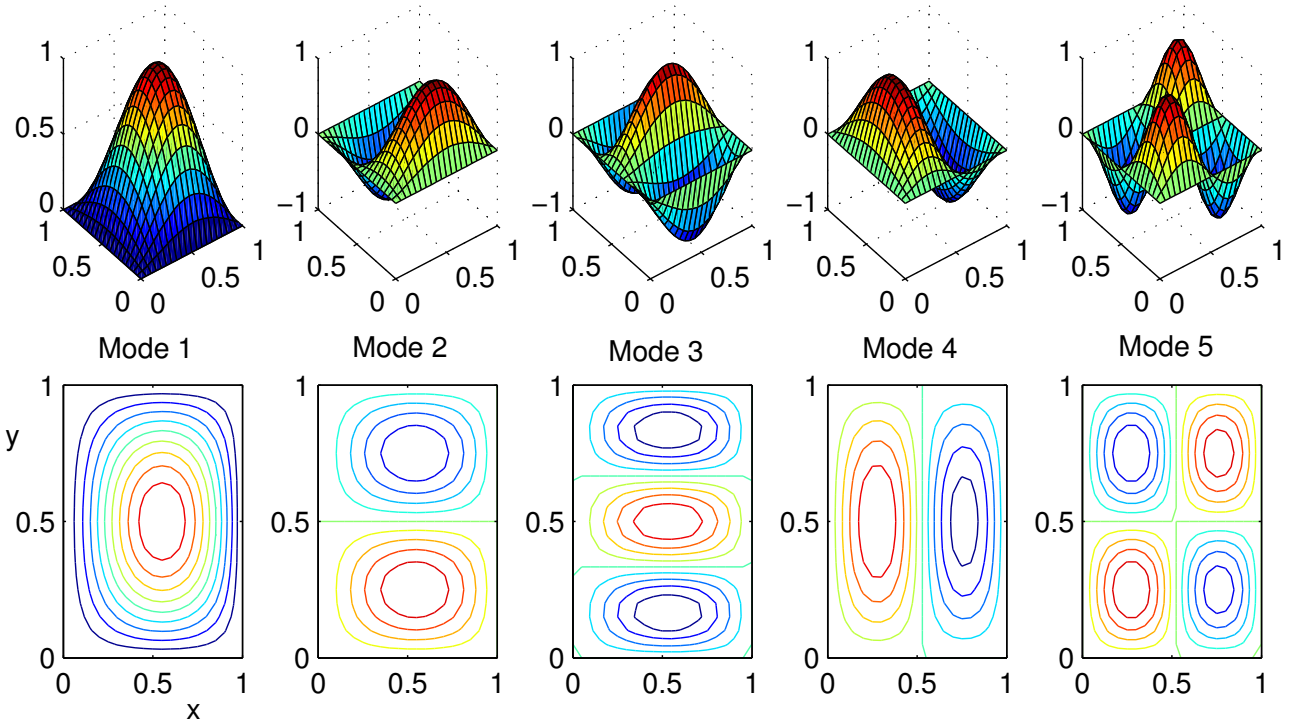

Fig. S6: First five flexural mode shapes for moderately thick ($S = 10$) IPFG smart plate (a) under constant properties case, and subjected to clamped–simply supported (CSSS) boundary conditions.

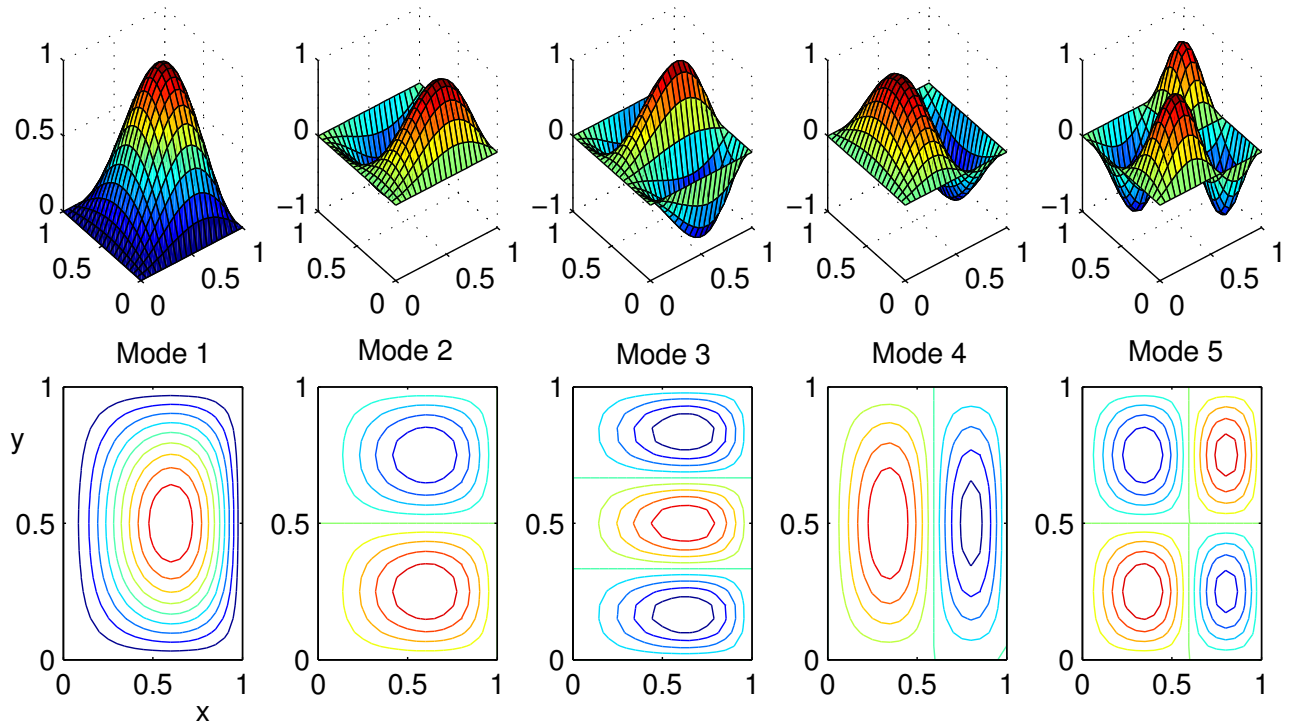

Fig. S7: First five flexural mode shapes for moderately thick ($S = 10$) IPFG smart plate (a) under gradation case 1, and subjected to clamped–simply supported (CSSS) boundary conditions.

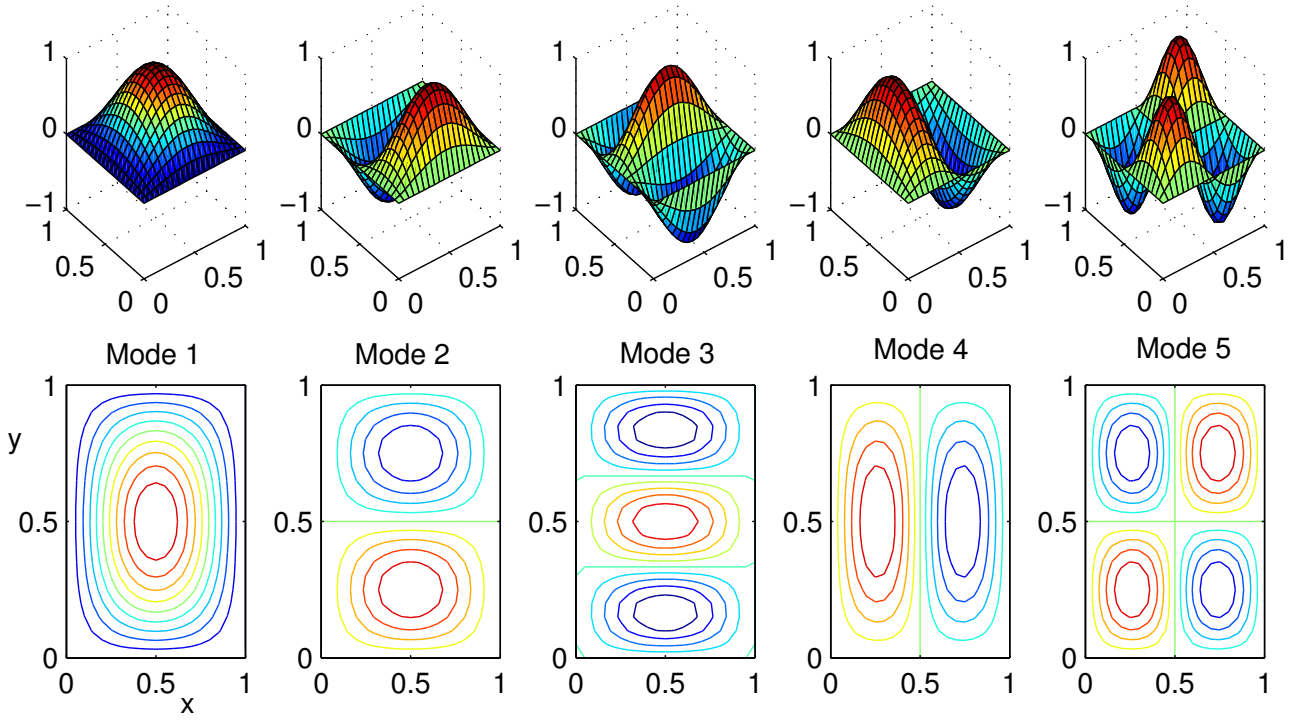

Fig. S8: First five flexural mode shapes for moderately thick ($S = 10$) IPFG smart plate (a) under constant properties case, and subjected to clamped–clamped supported (CCSS) boundary conditions

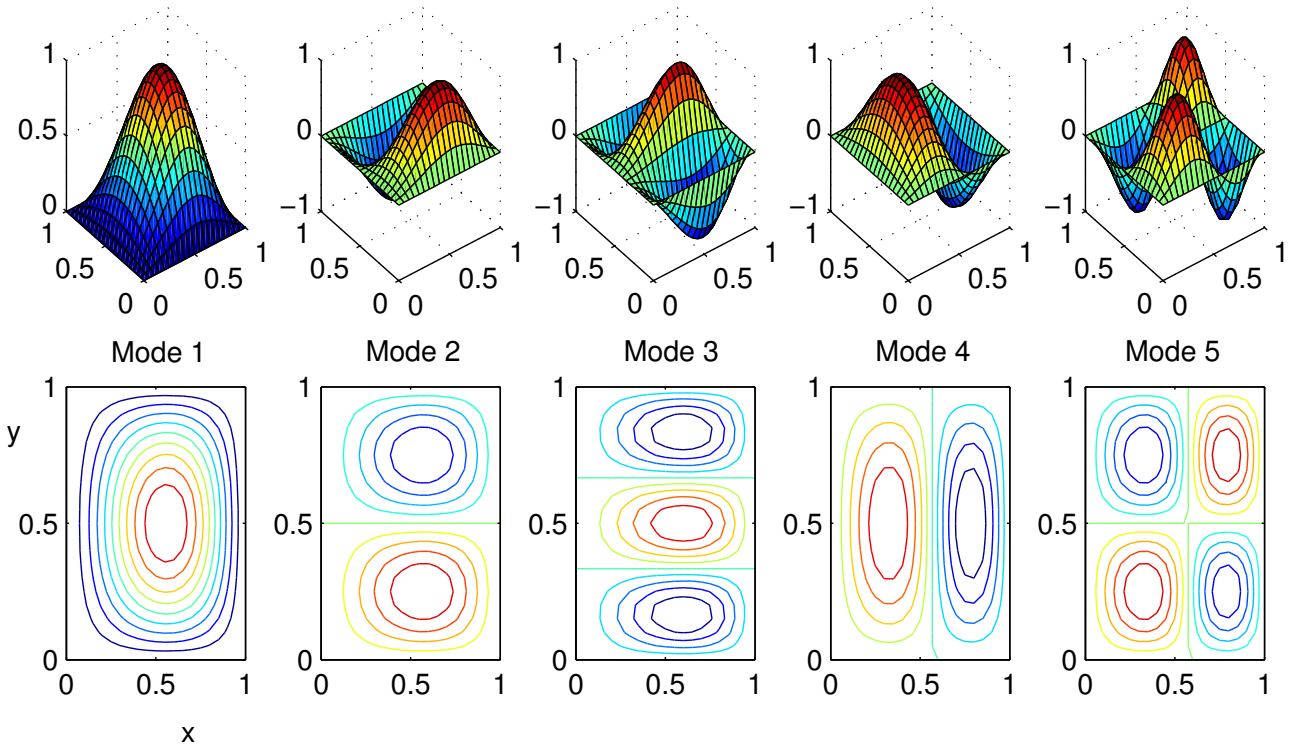

Fig. S9: First five flexural mode shapes for moderately thick ($S = 10$) IPFG smart plate (a) under gradation case 1, and subjected to clamped–clamped supported (CCSS) boundary conditions.

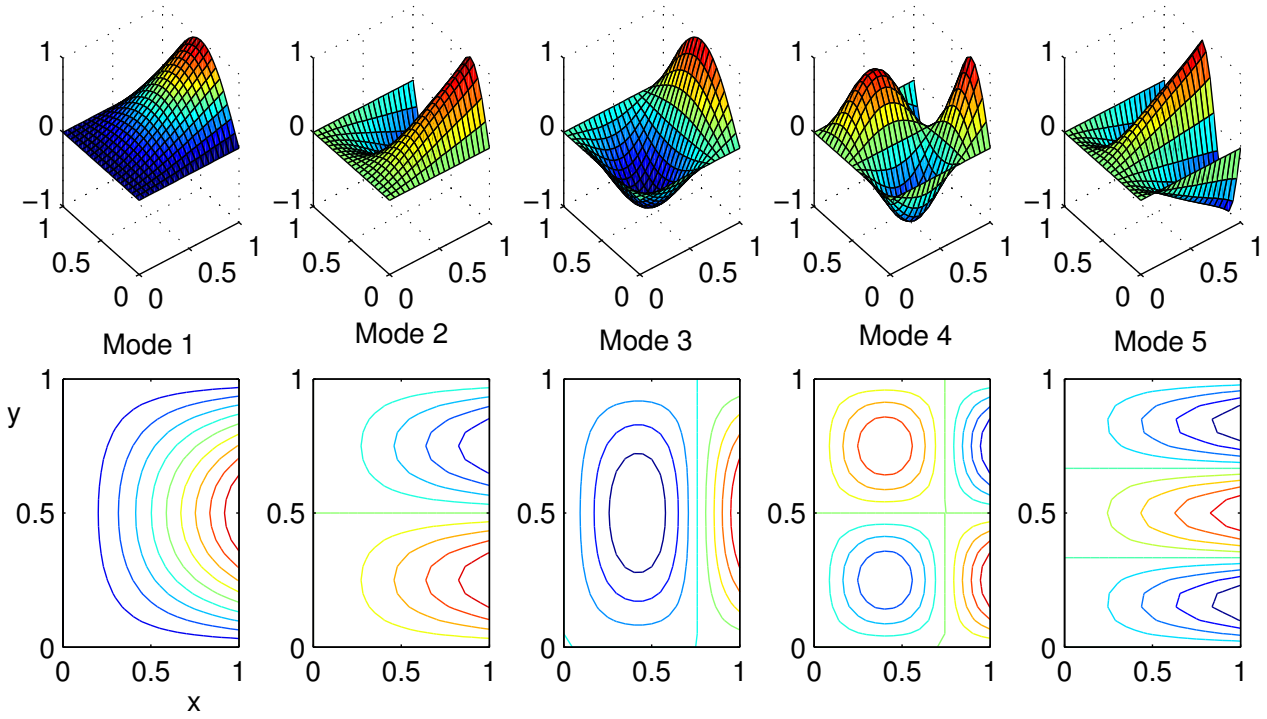

Fig. S10: First five flexural mode shapes for moderately thick ($S = 10$) IPFG smart plate (a) under constant properties case, and subjected to clamped–free supported (CFSS) boundary conditions.

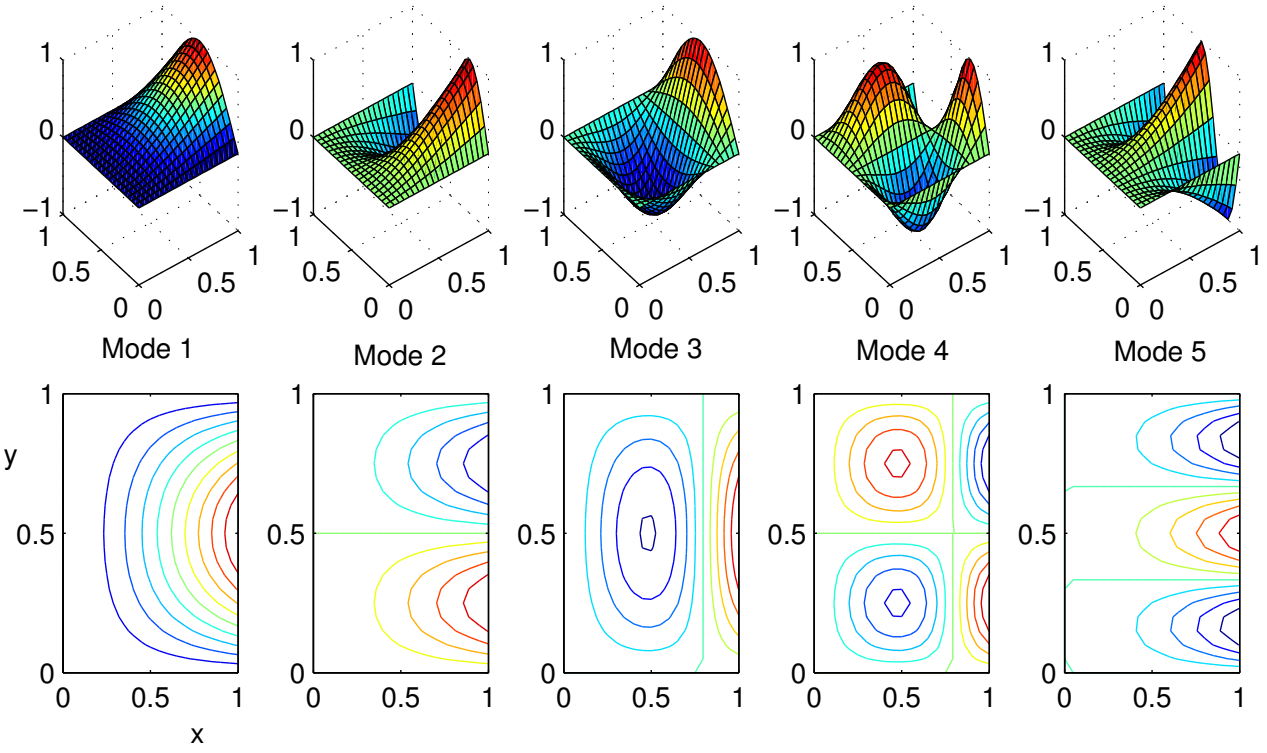

Fig. S11: First five flexural mode shapes for moderately thick ($S = 10$) IPFG smart plate (a) under gradation case 1, and subjected to clamped–free supported (CFSS) boundary conditions.

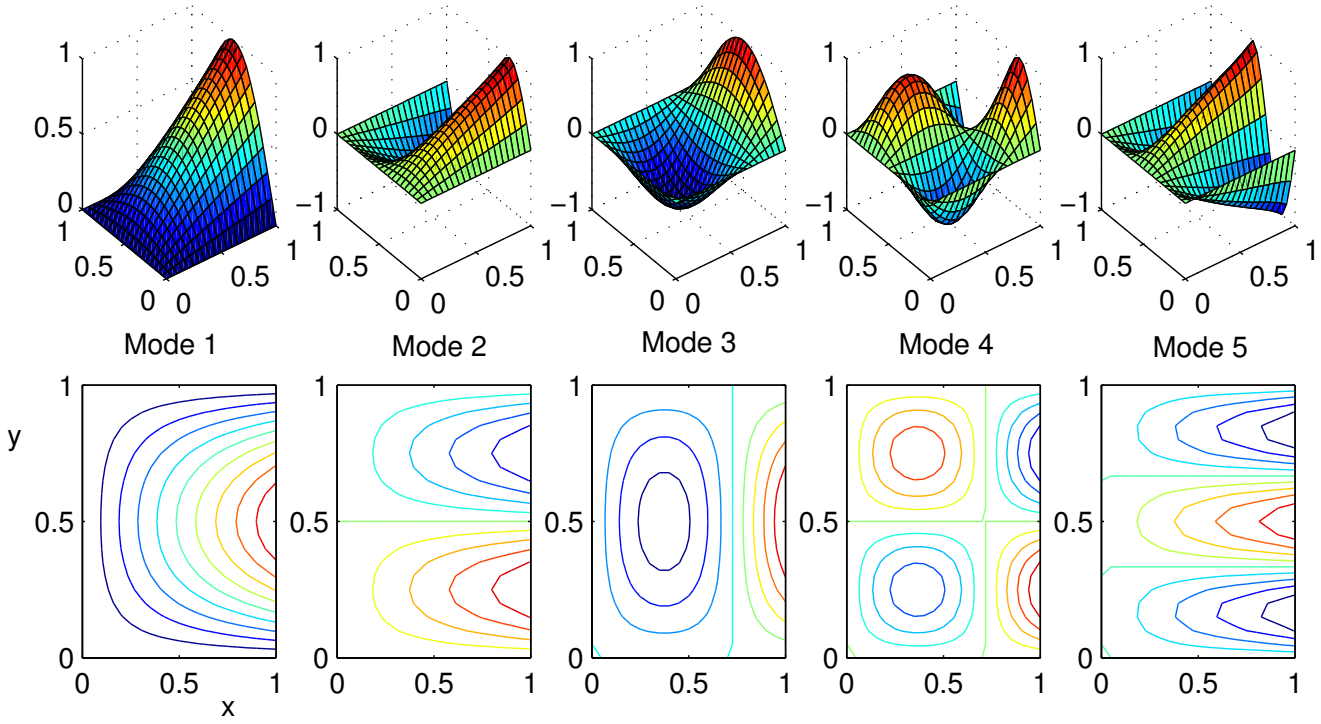

Fig. S12: First five flexural mode shapes for moderately thick ($S = 10$) IPFG smart plate (a) under constant properties case, and subjected to simply supported–free supported (SFSS) boundary conditions.

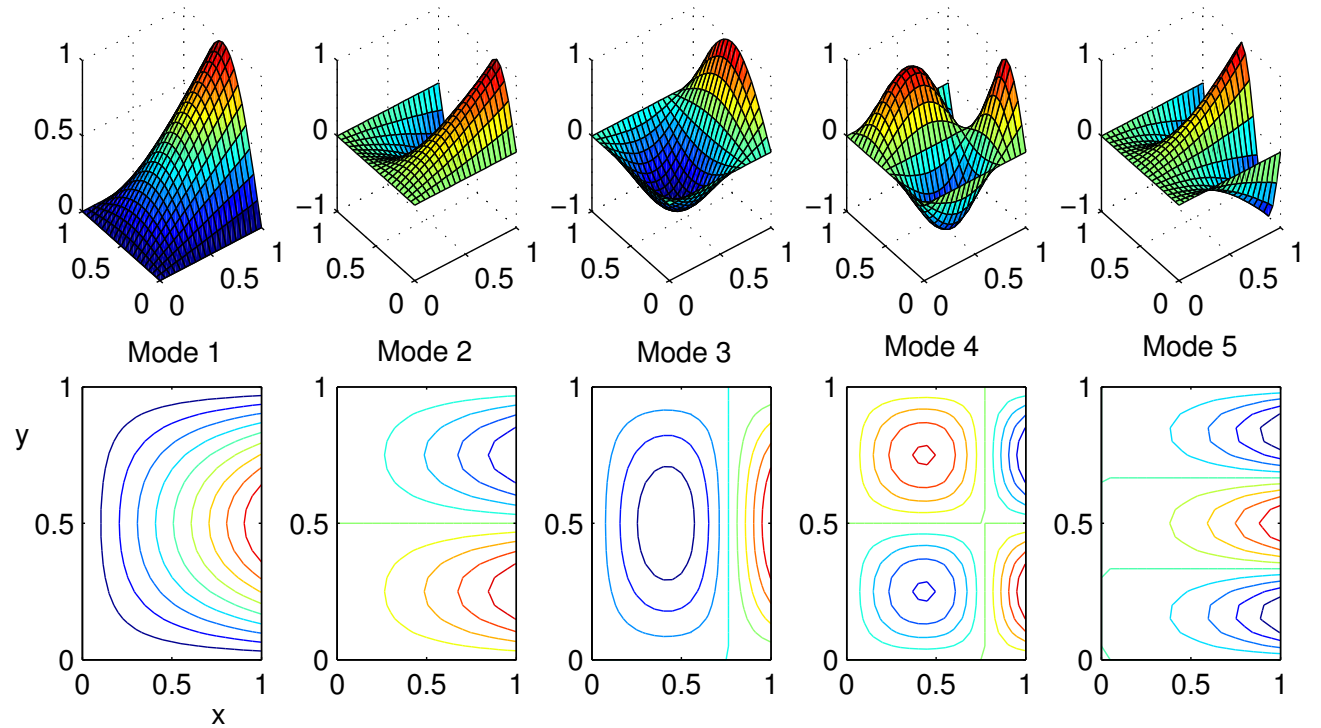

Fig. S13: First five flexural mode shapes for moderately thick ($S = 10$) IPFG smart plate (a) under gradation case 1, and subjected to simply supported–free supported (SFSS) boundary conditions.

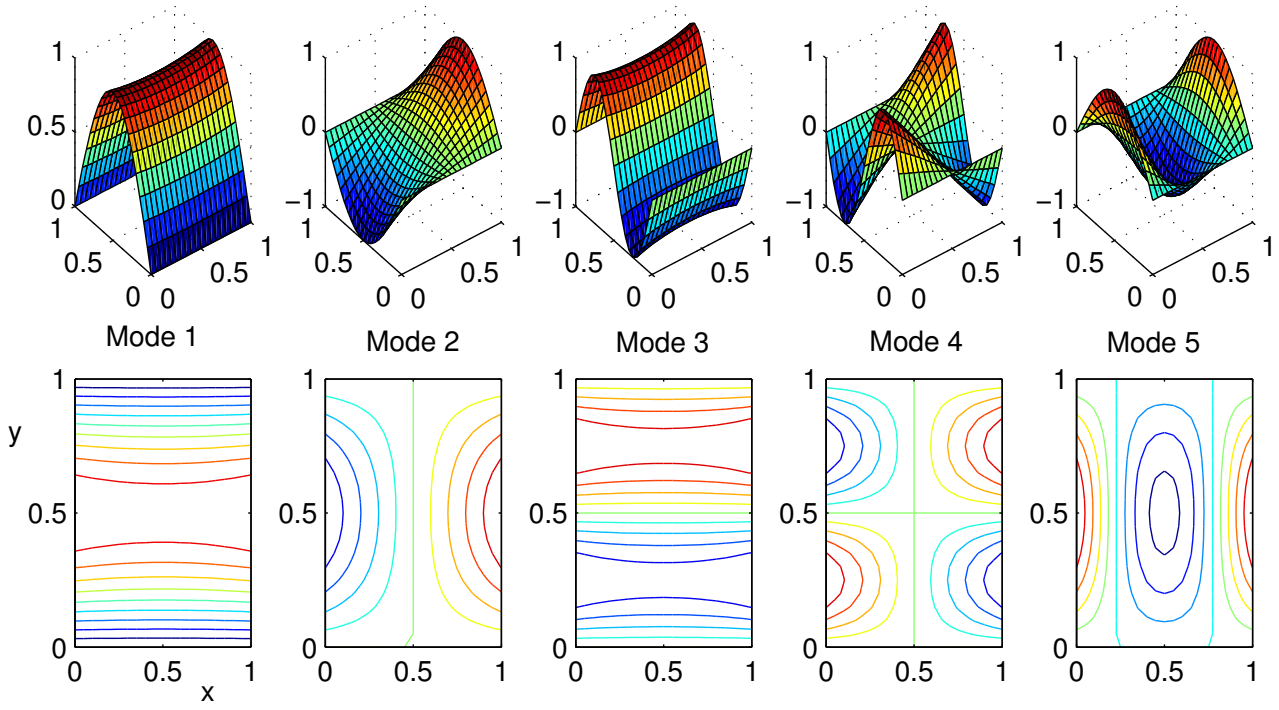

Fig. S14: First five flexural mode shapes for moderately thick ($S = 10$) IPFG smart plate (a) under constant properties case, and subjected to free–free supported (FFSS) boundary conditions.

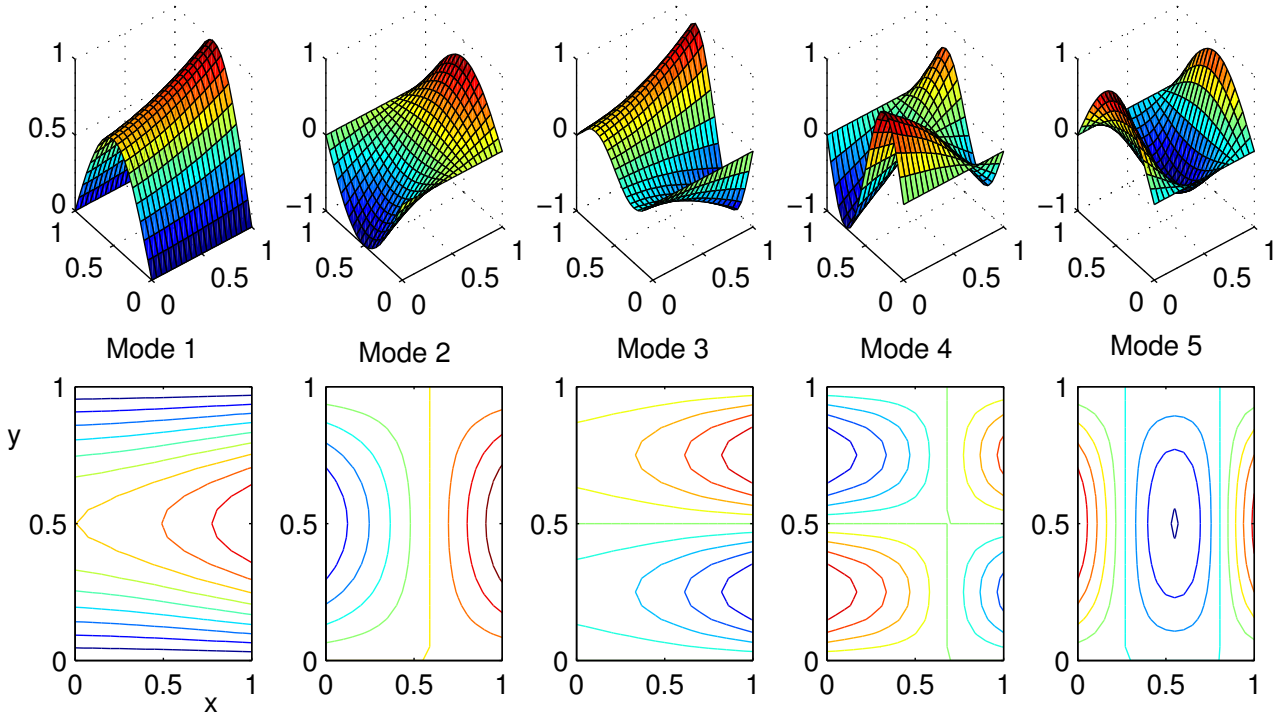

Fig. S15: First five flexural mode shapes for moderately thick ($S = 10$) IPFG smart plate (a) under gradation case 1, and subjected to free–free supported (FFSS) boundary conditions.

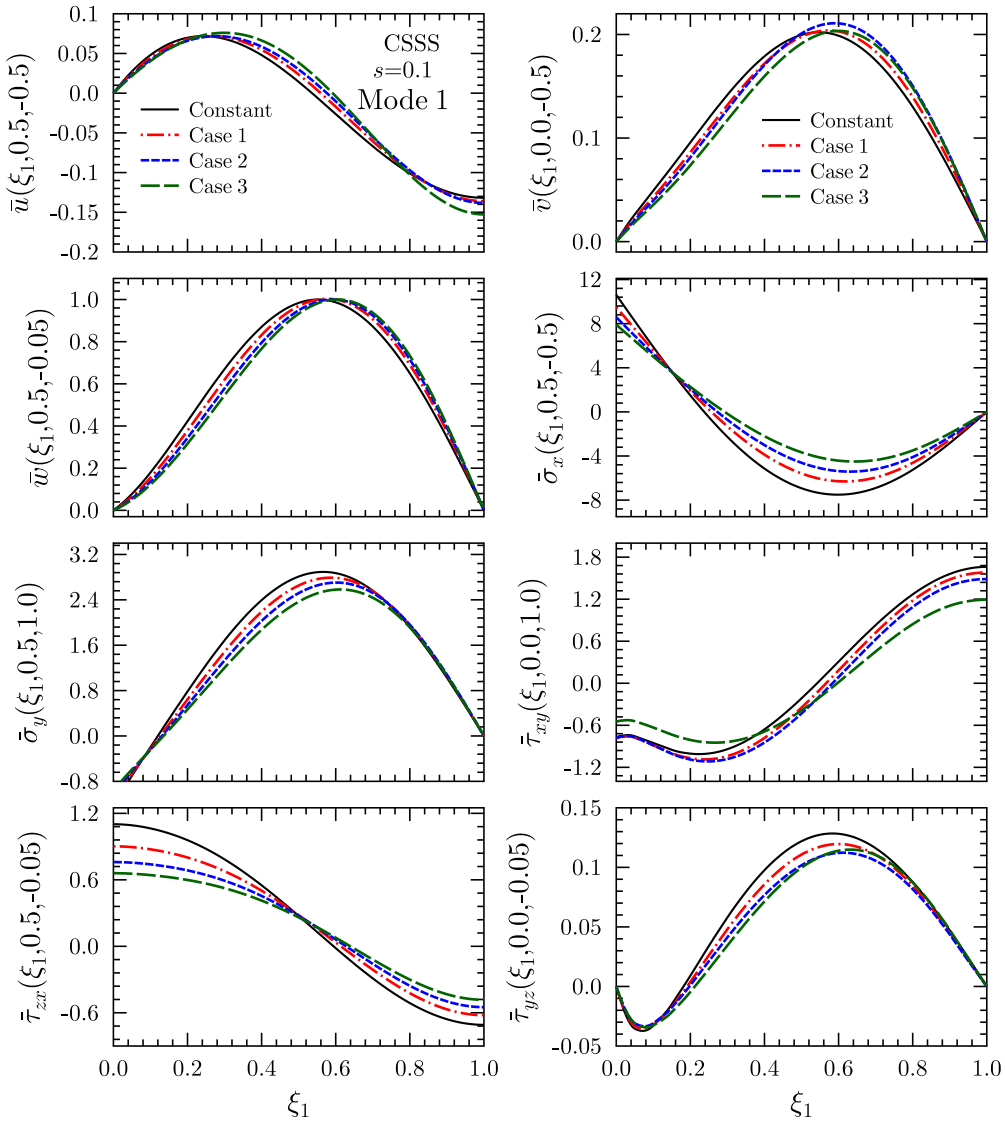

Fig. S16: Influence of in-plane variation of density and stiffness on axial variations of displacements and stresses for first flexural vibration mode (Mode-1) of the moderately thick ($S = 10$) IPFG smart plate (a) subjected to CSSS boundary condition.

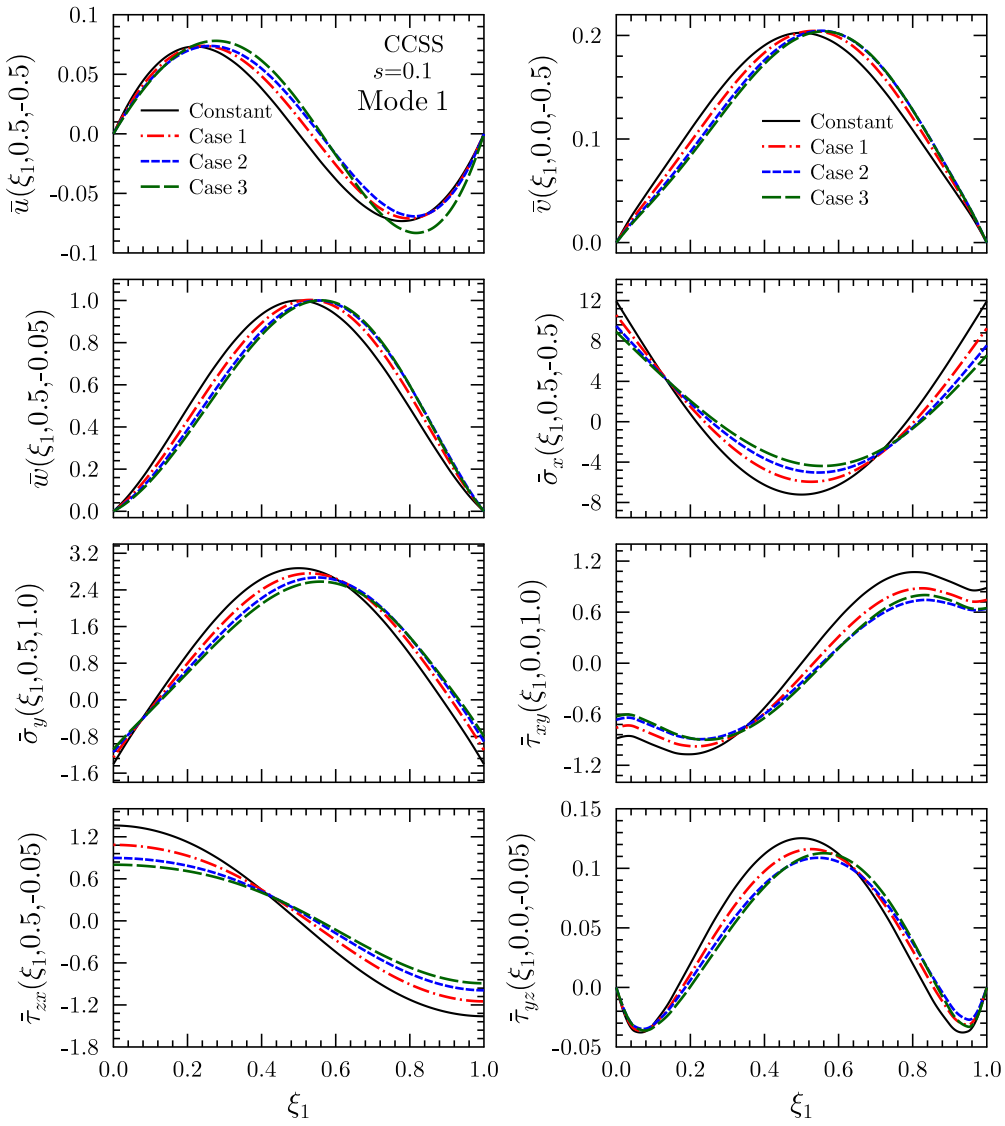

Fig. S17: Influence of in-plane variation of density and stiffness on axial variations of displacements and stresses for first flexural vibration mode (Mode-1) of the moderately thick ($S = 10$) IPFG smart plate (a) subjected to CCSS boundary condition.

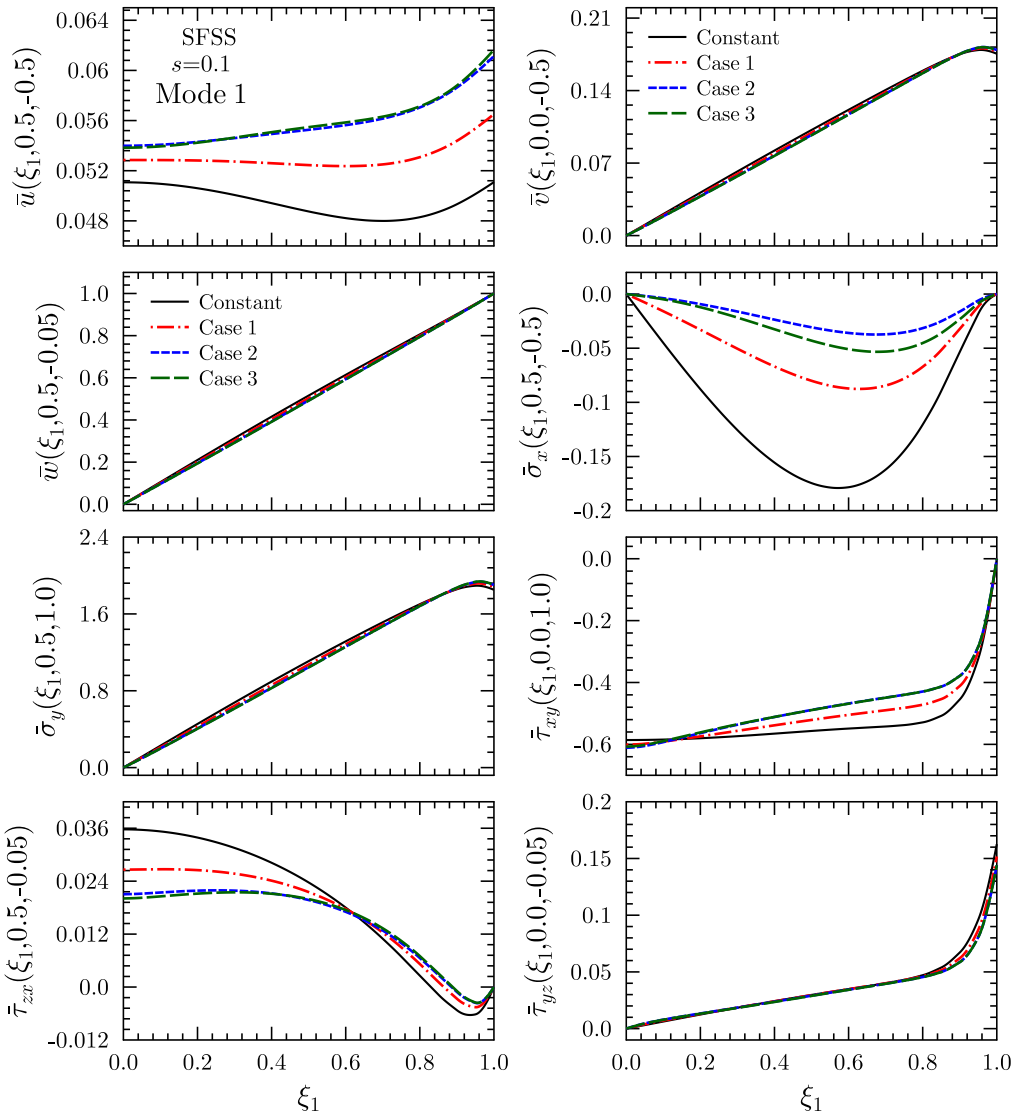

Fig. S18: Influence of in-plane variation of density and stiffness on axial variations of displacements and stresses for first flexural vibration mode (Mode-1) of the moderately thick ($S = 10$) IPFG smart plate (a) subjected to SFSS boundary condition.

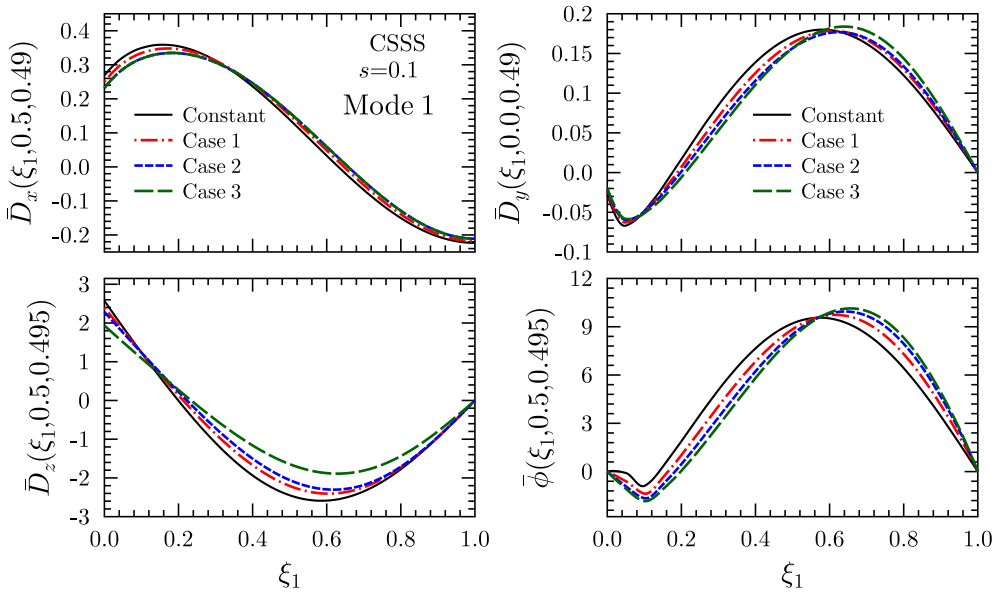

Fig. S19: Influence of in-plane variation of density and stiffness on axial variations of electric variables for first flexural vibration mode (Mode-1) of the moderately thick ($S = 10$) IPFG smart plate (a) subjected to CSSS boundary condition.

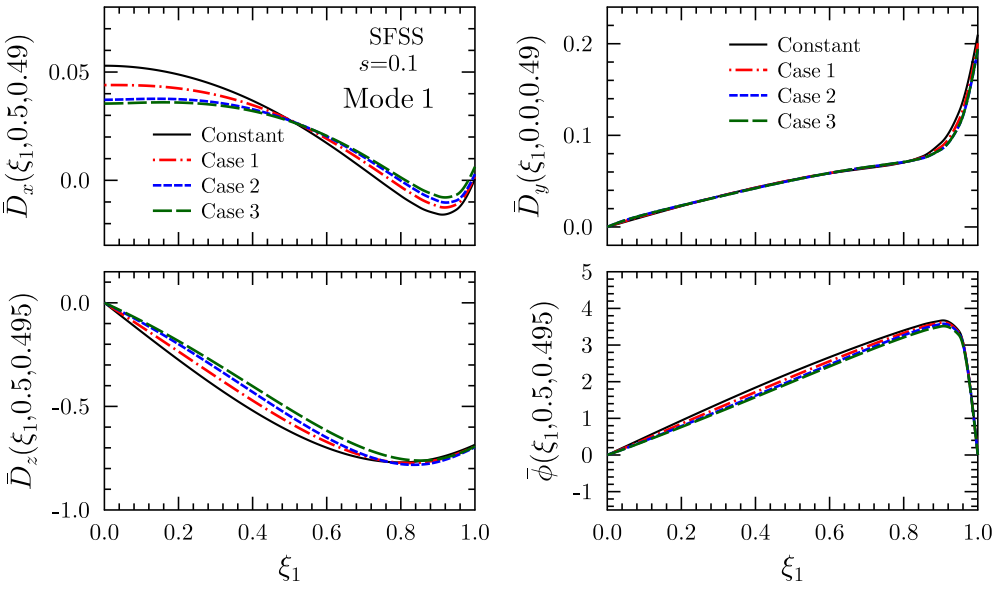

Fig. S20: Influence of in-plane variation of density and stiffness on axial variations of electric variables for first flexural vibration mode (Mode-1) of the moderately thick ($S = 10$) IPFG smart plate (a) with SFSS boundary condition.

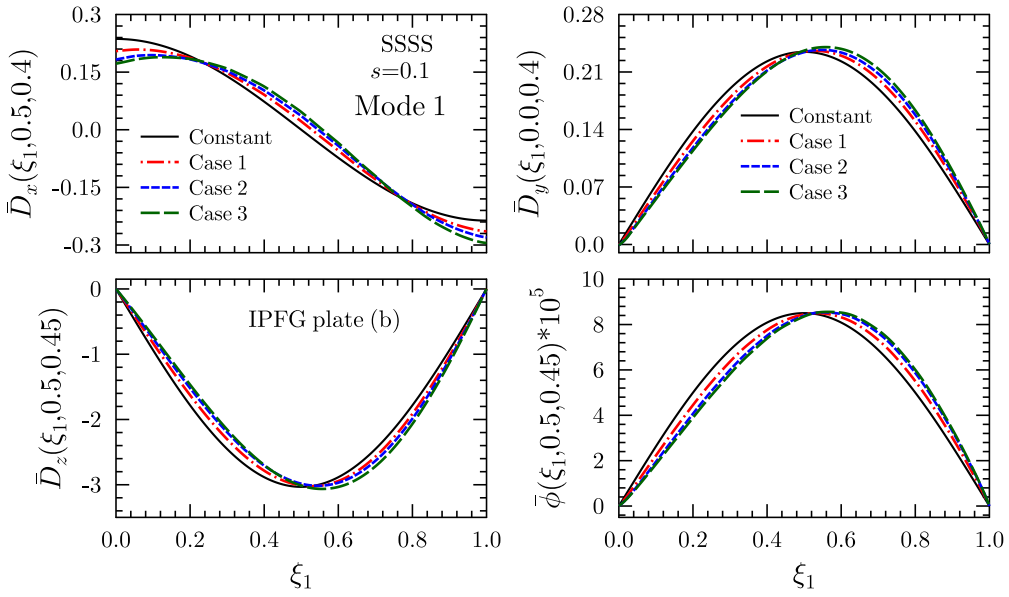

Fig. S21: Influence of in-plane variation of density and stiffness on axial variations of electric variables for first flexural vibration mode (Mode-1) of the moderately thick ($S = 10$) IPFG smart plate (b) with SSSS boundary condition.

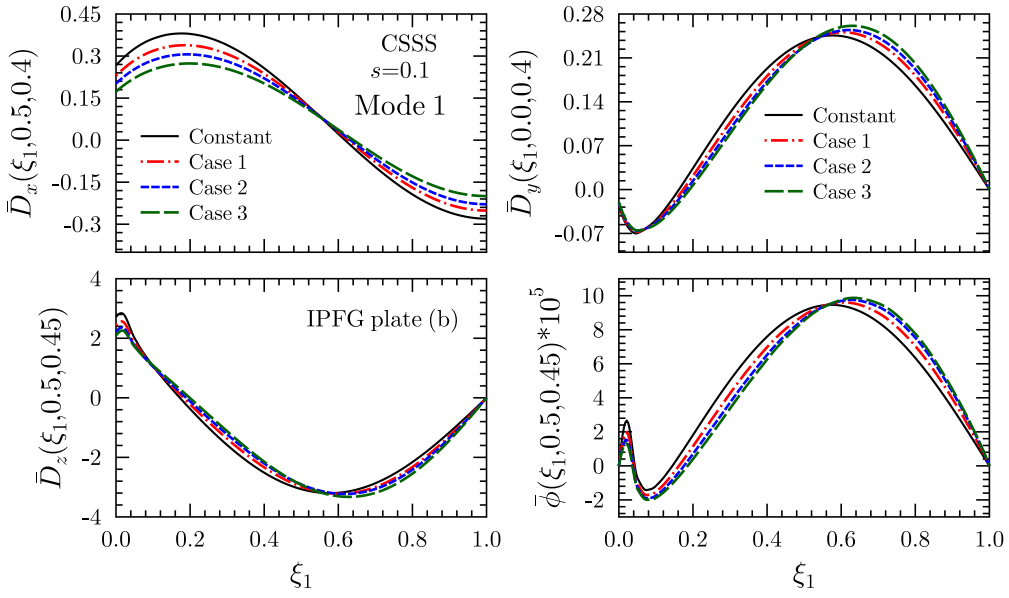

Fig. S22: Influence of in-plane variation of density and stiffness on axial variations of electric variables for first flexural vibration mode (Mode-1) of the moderately thick ($S = 10$) IPFG smart plate (b) with CSSS boundary condition.

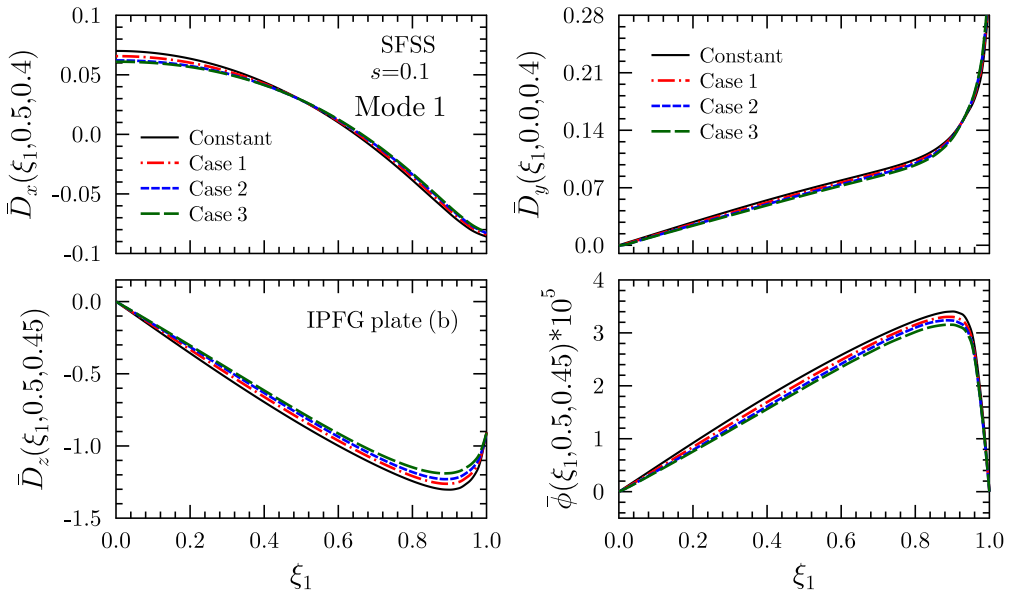

Fig. S23: Influence of in-plane variation of density and stiffness on axial variations of electric variables for first flexural vibration mode (Mode-1) of the moderately thick ($S = 10$) IPFG smart plate (b) with SFSS boundary condition.

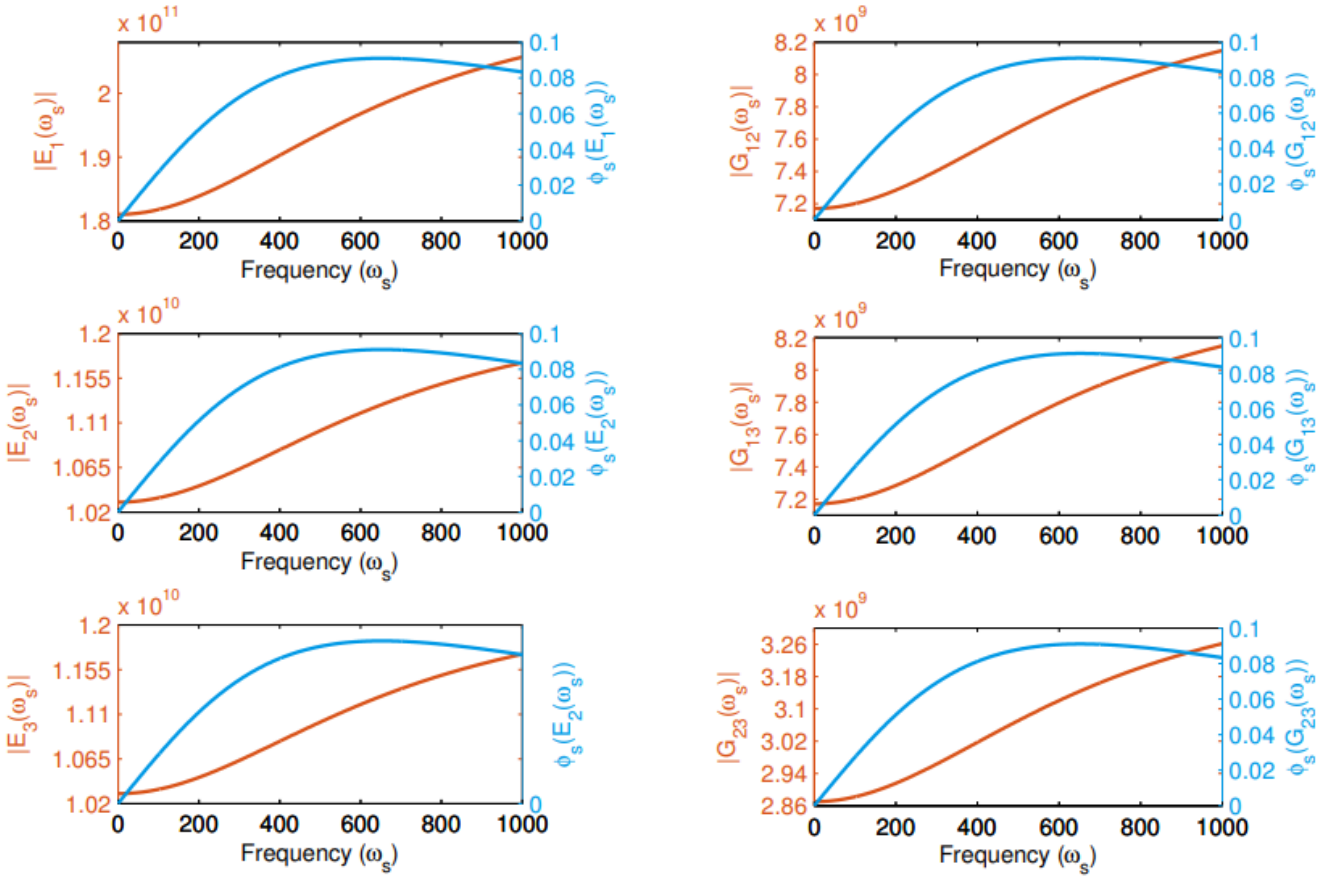

Fig. S24: Effect of viscoelasticity on Young's moduli (E_1 , E_2 and E_3) and shear moduli (G_{12} , G_{12} and G_{23}) in frequency domain. Frequency-dependent amplitudes and phase angles are presented for orthotropic viscoelastic layer of Mat. 4 (Gr/Ep) having elastic properties E_1=181.0 GPa, E_2=10.3, E_3=10.3 GPa, G_{12}=7.17 GPa, G_{13}=7.17 GPa and G_{23}=2.87 GPa.

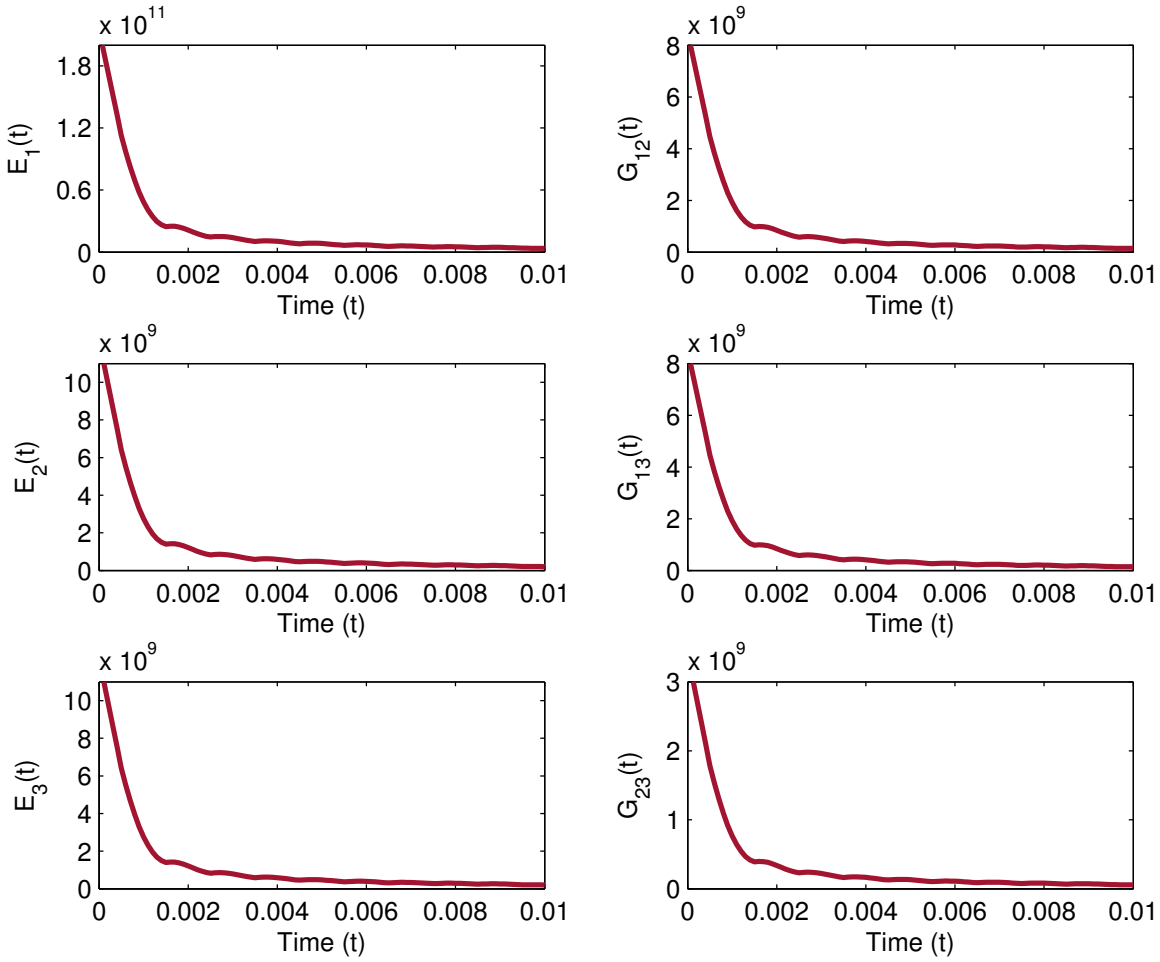

Fig. S25: Effect of viscoelasticity on Young's moduli (E_1 , E_2 and E_3) and shear moduli (G_{12} , G_{12} and G_{23}) in time domain. Variation of Young's moduli and shear moduli of Mat. 4 (Gr/Ep) with time is obtained using inverse Fourier transformation (IFFT) technique.

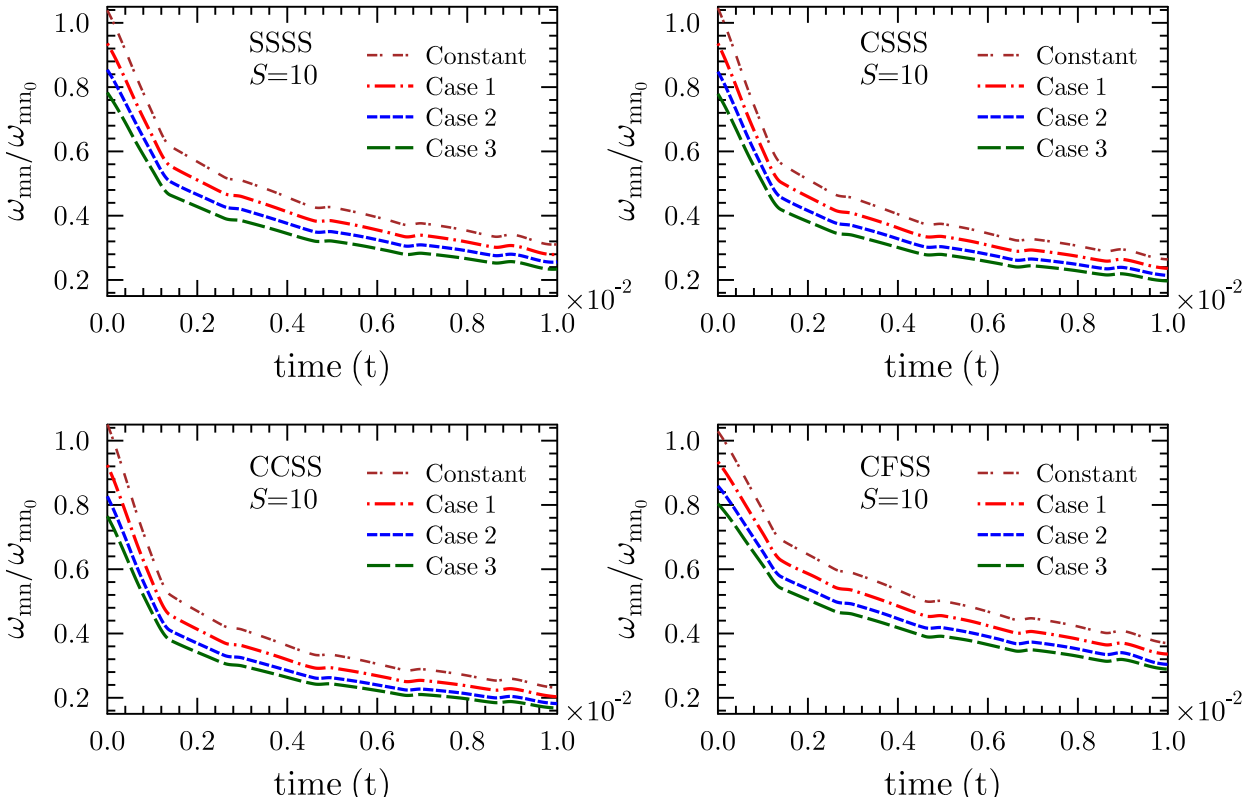

Fig. S26: Effect of viscoelasticity on the first natural frequencies of three-layered moderately thick (S=10) viscoelastic smart plate (b) with graded properties. The time-dependent variation of first natural frequencies is plotted in non-dimensionalized form for different gradation cases under different boundary conditions such as SSSS, CSSS, CCSS, CFSS. The non-dimensionalization is done by dividing the natural frequencies of viscoelastic plate by the natural frequencies of elastic plate without any gradation given in Table 6.